Graphene Oxide Coated Optical Fiber Mach-Zehnder Interferometers

By

Bowen Gao

A Thesis Submitted in Partial Fulfillment of

the Requirements for the Degree of

Master of Science

Department of Physics and Physical Oceanography

Memorial University of Newfoundland

September 2023

St. John's Newfoundland

Abstract

Optical fibers are extensively utilized in the telecommunication industry for their exceptional light-guiding capabilities. Furthermore, their remarkable attributes, including high flexibility, low loss, compact size, immunity to electromagnetic interference, and operation in harsh environments, have sparked extensive research into their applications across diverse sensor fields.

The emergence of nanomaterials with unique physical and chemical properties offers many new applications. As one of the graphene derivatives with various oxygen-containing functional groups, graphene oxide (GO) based materials enable a wide range of sensing applications owing to their interaction with external water molecules and various organic solvents. This study investigates the spectral properties of two GO-coated symmetric fiber Mach-Zehnder interferometers (FMZIs), i.e., tapered and bulge-fused structures, under varying environmental conditions, in comparison with uncoated FMZIs. The light energy density distribution along those microstructures is simulated by COMSOL Multiphysics software. The study begins by examining the sensitivity of FMZIs to refractive index, temperature, and humidity by observing the shift of dip wavelength at different environmental conditions. Then, the interferometers are coated with GO using the in-situ layer self-assembly method, which are silanization-treated fibers to create a positively charged surface, enabling the attraction and accumulation of negatively charged materials. Next, coating effects on different fiber structures and sensitivities to environmental conditions are compared. Additionally, two different GO-based coatings (graphene oxide-sodium alginate composite, and graphene oxide-fullerenol nano-

composite encapsulated by the hydrogel) are applied to the tapered structure to assess their effects on the optical properties of the sensor under different environmental conditions. Finally, the spectra of the tapered FMZIs with and without different coatings are measured at various curvatures. The sensitivity of the interferometer in curvature measurement is analyzed using the conformal mapping technique to explore the properties of the coatings under different curvatures. This study demonstrates the effectiveness and great potentials of the graphene oxide-based nanomaterials in fiber-optic sensing.

Acknowledgments

I am grateful to my supervisors, Dr. Qiying Chen and Dr. Liqiu Men, for allowing me to work and study in their research group and for the valuable guidance they gave me during my graduate studies, which has benefited me greatly during these two years. I would also like to thank Dr. Chen for giving me a lot of comments to help me complete my thesis.

I would like to thank Dr. Anand Yethiraj, Dr. Todd Andrews, and Dr. Shams Anwar for their courses and instructions. I am grateful to thank the School of Graduate Studies at the Memorial University of Newfoundland, the physics department, and my supervisor for financial support.

Finally, I would like to thank my parents and friends for their support and encouragement over the years.

Table of Contents

List of Tables

List of Figures

List of Abbreviations

FMZI	Fiber Mach-Zehnder interferometer
OPD	Optical phase difference
LPG	Long-period fiber grating
GO	Graphene oxide
i-LBL	In-situ layer-by-layer assembly
APTES	(3-Aminopropyl) triethoxysilane
SMF	Single-mode optical fiber
BBD	Box-Behnken design
R^2	Coefficient of determination
FSR	Free spectral range
DFT	Discrete Fourier transform
RI	Refractive index
RH	Relative humidity
OSA	Optical spectrum analyzer
Algin	Alginic acid sodium
$C_{60}(OH)_n$	Fullerenol

Chapter 1 Introduction

Sensor technology plays an important role in entertainment, health, transportation, and many industries. Over the past few decades, optical fibers have been widely deployed in telecommunications due to their exceptional properties as the light guides [1, 2]. In addition, due to the unique characteristics of optical fibers, including high flexibility, low propagation loss, high sensitivity, compact size, high accuracy, immunity to electromagnetic interference, durability in harsh environments, and flexibility to be integrated directly into systems [3], fiber-optic-based sensing technology has provided novel solutions in various sensor fields with the development of optoelectronic technology.

The first sensing experiments using low-loss optical fibers were conducted in the early 1970s [4]. Since then, various studies have utilized optical fibers as sensing indicators for temperature [5], strain [6], pressure [7], rotation, displacement, refractive index [8], polarization, ultrasound [9], and humidity [10]. Furthermore, their sensing capabilities have been considerably enhanced by utilizing innovative fiber optic technologies of fiber gratings [11], fiber interferometers [12], Brillouin/Raman scattering [13], surface plasmon resonance [14], micro-structured fibers [15], nanowires [16], and specialty fiber couplers [17]. Indeed, some fiber optic sensors are used for real-time deformation monitoring of aircraft, ships, bridges, and constructions [18]. With the development of human-friendly smart materials, even health monitoring systems using fiber devices have attracted great interest as future technologies [19].

1.1 Optical Fibers

An optical waveguide is a dielectric structure that can transmit energy at wavelengths in the infrared or visible portions of the electromagnetic spectrum. Waveguides used for optical communication are highly flexible fibers composed of almost transparent dielectric materials. Optical fibers are long cylinders of transparent glass or plastic characterized by a refractive index variation along its radial direction [20]. These fibers have a small cross-section, comparable to human hair, and are usually divided into three layers, as shown in Figure 1-1 (a). The central region is the core, surrounded by the cladding, surrounded by a protective coat. The core and cladding are typically made of the same material with a different doping concentration, for example, the standard single-mode silica fiber SMF-28 has a doped core (with as low as ~3.0 mol.% GeO_2 content) [21, 22, 23]. In the single-mode fiber the refractive index profile n is graded within the core, while the cladding index is usually uniform, as shown in Figure 1-1 (b) [24]. The core index must be greater than the cladding index because light hitting an interface from a higher to lower index can undergo total internal reflection, which is necessary for the propagation of light [25].

The refractive index of an optical medium is one of the key material properties. It is a dimensionless number that indicates the behaviour of light propagation in that medium. Snell's law of refraction describes as follows:

$$n_1 \cos\theta_{\mathrm{i}} = n_2 \cos\theta_{\mathrm{t}} \tag{1-1}$$

where θ_{i} is the angle of incidence, θ_{t} is the angle of refraction, and n_1 and n_2 are the refractive indices of medium 1 and 2, respectively, as shown in Figure 1-2 (a).

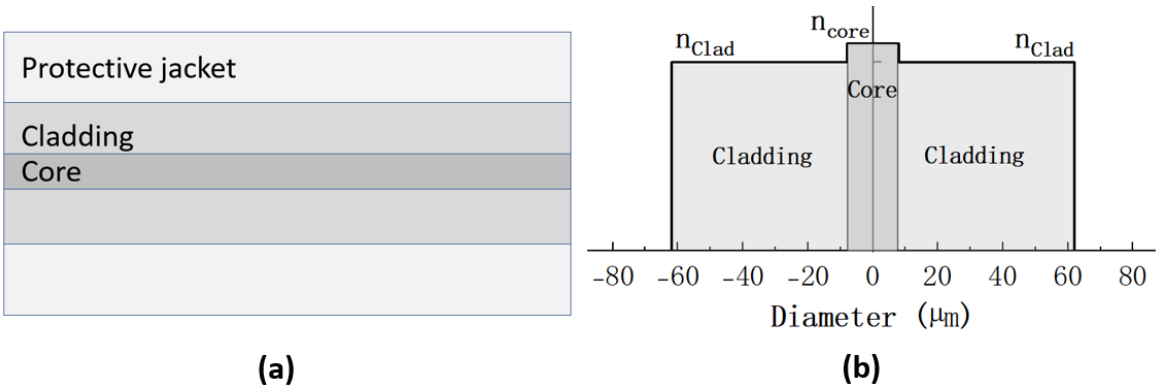

Figure 1-1: Schematic illustration of an optic fiber and step-index fiber. (a) Structure of an optic fiber. (b) Refractive index profile of step-index fiber, which has different constant refractive index values for the core and cladding.

Figure 1-2 (b) shows that light propagation in an optical fiber follows total internal reflection when light propagates from a higher refractive index medium (medium 1) towards a lower refractive index medium (medium 2) if $0 \leq \theta_i < \theta_c$. It is partly reflected and partly refracted if $\theta_c < \theta_i \leq \pi/2$, shown in Figure 1-2 (a), where θ_c is the critical angle, defined by: [24]

$$\theta_c = \cos^{-1}\left\{\frac{n_2}{n_1}\right\} = \sin^{-1}\left\{1 - \frac{n_2^2}{n_1^2}\right\}^{\frac{1}{2}} \tag{1-2}$$

When the condition of total internal reflection is satisfied, all the power of light returns back to the fiber core. If the fiber is not significantly bent, a light beam can propagate over a very long distance along the fiber with an intensity loss of less than 1 dB/km [26].

Mode is a terminology to describe the nature of propagation of electromagnetic waves in a waveguide. Based on the number of modes propagating through the optic fiber, the fiber can be grouped into two categories: single-mode and multimode fibers. Modes represent electromagnetic field patterns along the light path inside the fiber. The first type is transverse electric (TE) modes for which $E_z = 0$, $H_z \neq 0$, and the second is transverse magnetic (TM) modes for which $H_z = 0$, $E_z \neq 0$. E_z is the electric field in the z-direction, and H_z is the magnetic field in the z-direction [24].

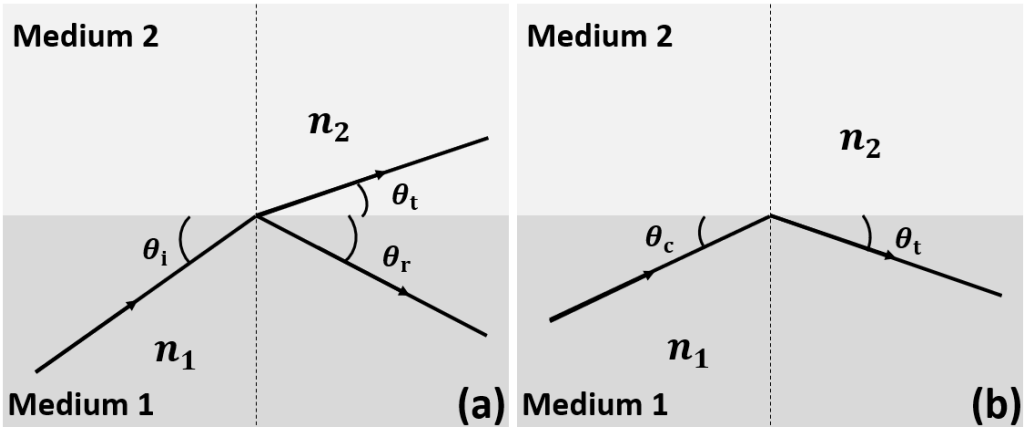

Figure 1-2: Reflection at a planar interface between unbounded regions of refractive indices n_1 and n_2. (a) Partial reflection and refraction where $\theta_i = \theta_r$ (reflection angle), and (b) total internal reflection.

In optical fibers, along with TE and TM modes, another hybrid mode with axial electric and magnetic fields is classified into EH and HE modes. In EH modes, the axial magnetic field H_z is relatively strong; in HE modes, the axial electric field E_z is relatively strong. These modes are now designated linearly polarized (LP) modes based on the linearly polarized light.

In a single-mode fiber, only one mode (LP_{01} mode) can propagate through the fiber. The number of modes propagating through the fiber is proportional to its V-number: [27]

$$V = \frac{2\pi a}{\lambda}\sqrt{n_{\text{core}}^2 - n_{\text{clad}}^2} = \frac{2\pi a}{\lambda}\,NA \tag{1-3}$$

where α is the radius of the core, λ is the wavelength of light propagating through the fiber, and NA is the numerical aperture.

The single-mode fiber has a core radius between 2.0 to 5.0 μm, and the multimode fiber has a core radius between 12.5 to 100.0 μm. When $V < 2.405$, the fiber only has one mode. Beyond $V \geq 2.405$, a higher-order mode emerges, indicating that $V = 2.405$ is the cut-off of the higher-order mode, below which that mode cannot propagate. Every high-order mode has a cut-off, but the first cut-off determines whether the fiber is single-mode or multimode.

Two parameters characterize the LP modes: LP (l, m). The parameter l is the azimuthal dependence of the mode: when $l = 0$, the light propagation does not depend on the azimuth angle, and when $l \neq 0$, it means the number of isolations in the electric field, and the parameter m is the number of zeros when going along the radial direction. Every LP mode has more than one propagating mode. A low-index-contrast approximation allows degenerate polarization; each mode has two polarizations. When $l > 0$, the mode also has two helical polarities: $+l$ and $-l$, which means that modes with $l = 0$ have a degeneracy of 2. In contrast, modes with $l > 0$ have 4 degeneracies, but the degeneracies are rarely represented due to the same shape [28].

A schematic illustration of the LP modes in a multimode fiber core with a 40.0 μm core diameter and 0.12 numerical aperture at 1550.0 nm wavelength is shown in Figure 1-3. The colour distribution in Figure 1-3 shows the distribution of the electric field in the x direction, and the colour legend is on the right side of the graph.

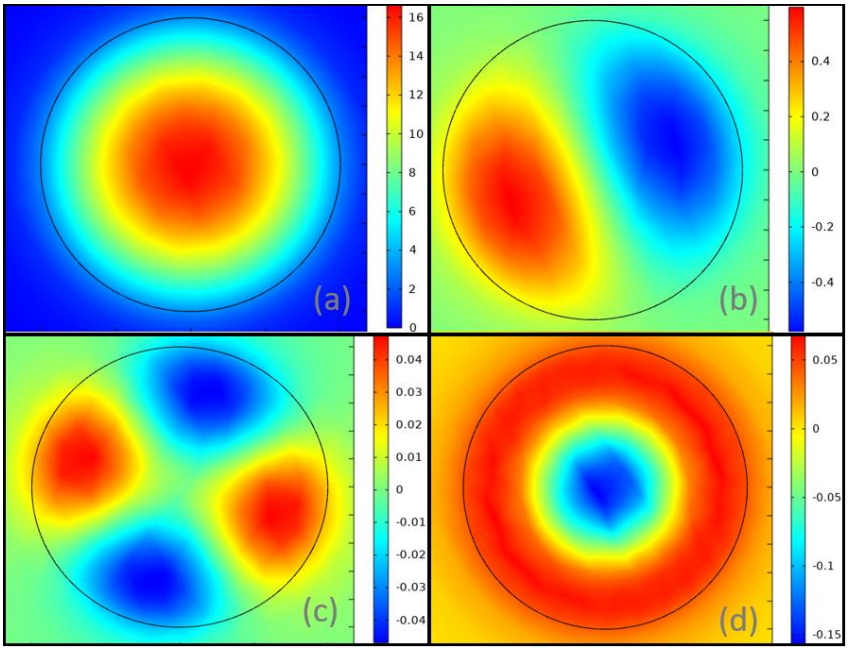

Figure 1-3: Schematic illustration of LP modes in a multimode optical fiber core. (a) LP (0,1), (b) LP (1,1), (c) LP (2,1), and (d) LP (0,2).

Figure 1-3 (a) and (d) show the distribution of E_x in a pattern of concentric circles, which means the parameter $l = 0$. In Figure 1-3 (b) and (c), the electric field is divided into two and four parts, which means the parameter is 1 and 2, respectively.

1.2 Interferometric Fiber Optic Sensors

A fiber optic interferometer operates with the interference between two beams propagating through different optical paths of a single fiber or two different fibers. The configuration consists of beam-splitting and beam-combining components and arranges one of the optical paths to be easily affected by external perturbations. Since the output signal of an interferometer contains a large amount of temporal and spectral information, measurements can be achieved by quantitatively detecting changes in wavelength, phase, intensity, frequency and bandwidth. These sensing indicators can perform remarkably in large dynamic ranges with high accuracy and sensitivity [29].

Currently, fiber optic interferometers have been miniaturized to the micro-scale. Small-sized fiber devices replace bulk optic components such as beam splitters, combiners, and objective lenses for sensors to operate on fiber scales. Due to its advantages of easy alignment, high coupling efficiency and high stability, the inline structure with two optical paths on one physical line has been widely investigated as the best candidate for realizing a miniaturized fiber optic interferometer. The fiber optic interferometer can be classified into four types: Fabry-Perot, Mach-Zehnder, Michelson, and Sagnac [30]. This study will focus on the characteristics of the Mach-Zehnder interferometer.

1.2.1 Mach-Zehnder Interferometers

Mach-Zehnder interferometers separate light from a single light source to determine the relative phase shift change between two collimated beams. The apparatus is named after the physicists Ludwig Mach and Ludwig Zehnder; Mach refined Zehnder's proposal in an 1892 article [31].

Mach-Zehnder interferometers are beam division interferometers comprising two mirrors and two beam splitters. Light is split into two paths within the system and recombined downstream of the second beam splitter to produce an interference pattern based on the phase difference between those two paths. A small asymmetry in either of the beam splitters or one of the mirrors can introduce a phase difference. Since the two paths are separate, this interferometer is more difficult to align. This technique can be applied to various applications, such as inserting an object along one of two paths, for example, a glass slide. This results in a difference in the optical path, therefore, a movement of the interference fringes. Counting the fringes can find the difference in the optical path. Figure 1-4 shows the interferometer scheme.

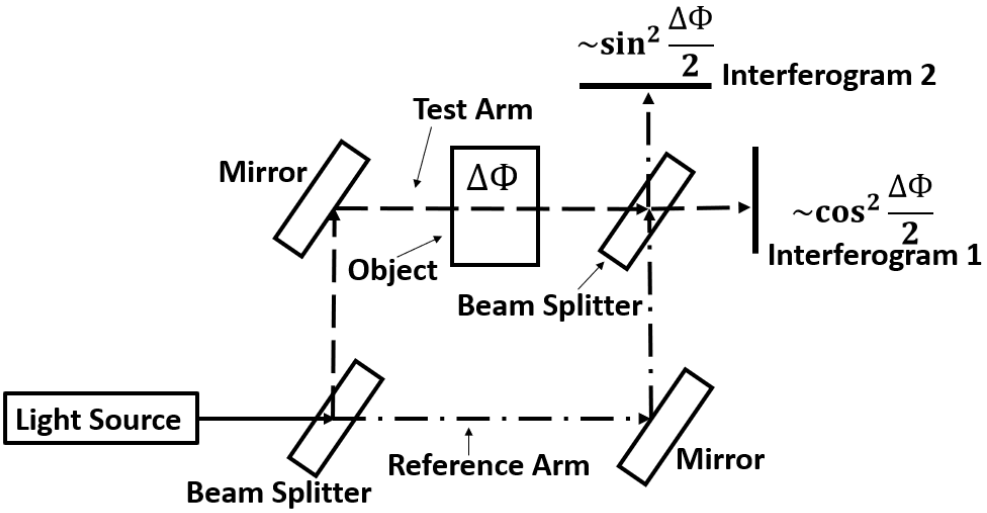

Figure 1-4: Schematic diagram of a Mach-Zehnder Interferometer.

In Figure 1-4, each beam in the Mach-Zehnder interferometer follows a different path before recombining downstream of the second beam splitter. There is interference between the two waves because of their coherent superposition.

There are two outputs of the Mach-Zehnder apparatus. The first output is parallel to the incoming beam, and the other is orthogonal. According to the parallel output, both beams arrive after two reflections, therefor both beams accumulated a 2π phase shift of wavelength. For the orthogonal output, one beam arrives after three reflections, while the other after a single reflection. Therefore, the two beams are out of phase with π and give rise to destructive interference.

After inserting an object into the interferometer, the beam in the test arm undergoes a phase shift of $\Delta\Phi$. This reflects on the intensity of the resulting beam. The output intensity of the parallel beam will have $\cos^2(\Delta\Phi/2)$, while the orthogonal beam $\sin^2(\Delta\Phi/2)$, as shown in Figure 1-4 [32].

1.2.2 Mach-Zehnder Interferometric Fiber Optic Sensors

Optical fiber Mach-Zehnder interferometer (FMZI) are widely used in various sensing applications because of their flexible configurations. According to Figure 1-5, early FMZIs had two independent arms, a reference arm and a test arm. The first fiber coupler splits incident light into two arms, then recombined by a second fiber coupler. According to the optical phase difference (OPD) between the two arms, the recombined light contains an interference component [33].

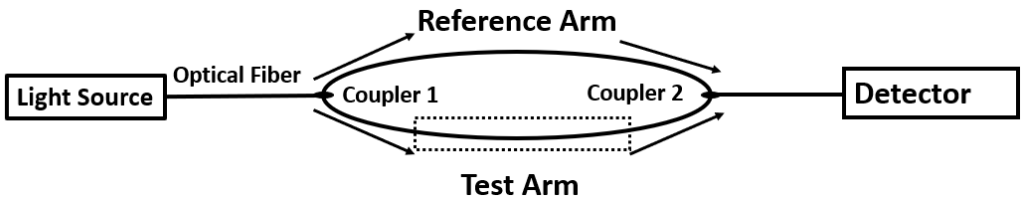

Figure 1-5: Schematic illustration of an FMZI.

In sensing applications, the reference arm is isolated from external variations, and only the test arm is subject to these variations. Therefore, the variation in the sensing arm caused by factors such as temperature, strain, and refractive index affects the OPD of FMZI. The sensitivity of the test arm to varying conditions can be measured by analyzing the interference signal.

The linear waveguide interferometer has rapidly replaced the scheme of using two separate arms in FMZIs since long-period fiber gratings (LPGs) were introduced [30]. In a single-mode fiber, a part of the beam is guided in a core mode coupled to cladding modes by one LPG and then recoupled to the core mode by another, as shown in Figure 1-6 (a) [34]. However, the LPG pair FMZI has a problem with the operating wavelength. Due to the phase-matching phenomenon of fiber gratings, LPGs operate within a limited range of wavelengths. For maximum performance, both LPGs should be identical [35].

Another method of splitting the beam is to splice two fibers with a tiny lateral offset [36], as shown in Figure 1-6 (b). The offset allows a portion of the core mode beam to couple to several cladding modes without being greatly affected by wavelength. In addition, the number of involved cladding modes and the insertion loss can be controlled by the offset amount. The beam also can be split by the core diameter mismatch method, shown in Figure 1-6 (c) [37] and (d) [38]. Fibers with different core sizes can be inserted to create the optical splitting effect.

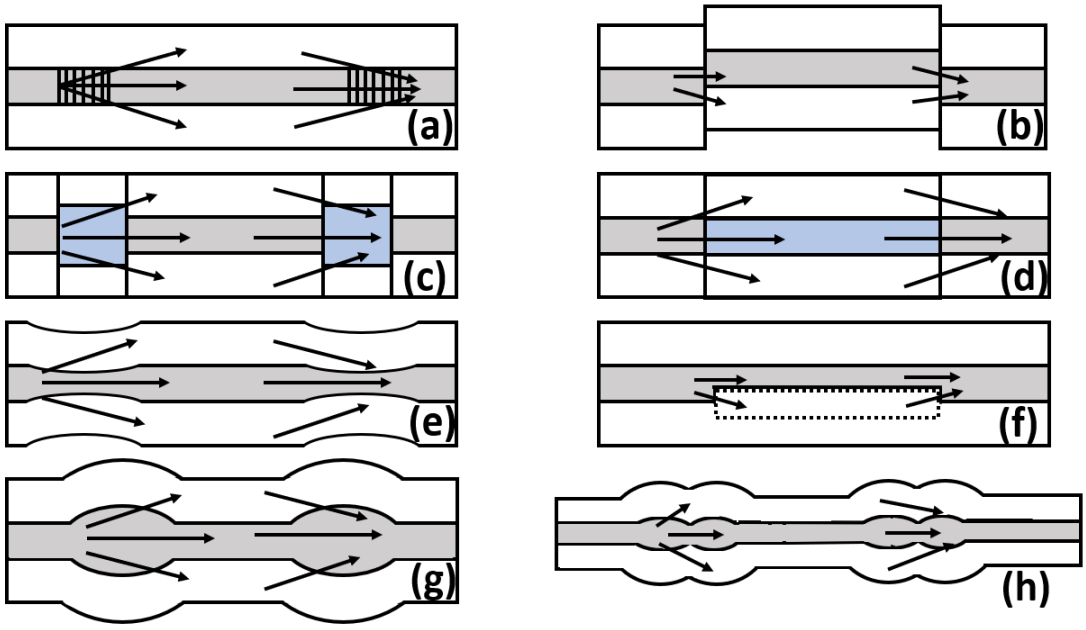

Figure 1-6: Configuration of various types of FMZIs: (a) LPGs, (b) core-offset, (c) core diameter mismatch with different core diameter fiber, (d) inserting different kinds of optical fiber, (e) tapers, (f) cavity formed by a femtosecond laser, (g) ball-shaped or waist-enlarged tapers, and (h) peanut-shaped structures.

Tapering a fiber at two points along the fiber, can form an effective FMZI, as shown in Figure 1-6 (e) [39]. Due to the tapered structure, the diameter of the fiber core portion decreases. As the diameter of the core mode remains the same, the beam in the core mode can be coupled to the cladding. Although cost-effective and relatively simple, it is mechanically weak, particularly in the taper regions. Femtosecond lasers can also be used to create the splitter and combiner pairs by creating cavities within the fiber [40], as shown in Figure 1-6 (f). Besides the tapered structure, there is also a method of coupling the core mode beam to the cladding mode by increasing the diameter of the fiber core, such as the ball shape structure [41] or the peanut shape structure [42], as shown in Figure 1-6 (g) and (h).

A broadband light source connected to the FMZI separates the light into two beams at the first fiber coupler. Light beams propagate in the core (I_1, reference arm) and cladding (I_2, test arm), then coupled at the second fiber coupler, resulting in an interference output. (Figure 1-7)

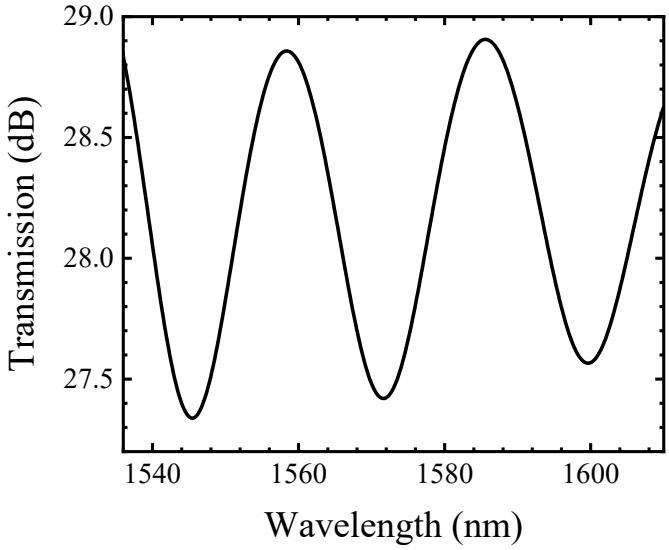

Figure 1-7: Simulated FMZI transmission spectrum with an interferometer length of 2.03 cm.

Theoretically, the transmitted light intensity of the FMZI can be expressed by the classic two-beam interference equation: [43]

$$I = I_1 + I_2 + 2\sqrt{I_1 I_2}\cos\Phi \tag{1-4}$$

where I is the intensity of the interference signal and the phase difference (Φ) between the cladding and core modes after propagating through the taper separation, which is:

$$\Phi = \frac{2\pi(n_{\text{core}} - n_{\text{clad}})L}{\lambda} = \frac{2\pi\Delta n_{\text{eff}}L}{\lambda} \tag{1-5}$$

where n_{core} and n_{clad} are the refractive indexes of fiber core and cladding, respectively. Effective refractive index Δn_{eff} is the refractive index difference between the fiber core and cladding, interferometer length L is the taper separation, and λ is the dip wavelength of the interference spectrum.

The phase difference satisfies the following conditions:

$$\Phi = (2m + 1)\pi \tag{1-6}$$

where m is the order of the Mach-Zehnder interference.

According to Eqn. (1-5) and (1-6) the wavelength of the attenuation dip λ_m can be expressed in:

$$\lambda_m = \frac{2\Delta n_{\text{eff}} L}{2m+1} \tag{1-7}$$

The free spectral range (FSR) between the adjacent attenuation dip wavelengths, $\Delta \lambda_m$, is:

$$\Delta\lambda_m = \lambda_{m-1} - \lambda_m = \frac{4\Delta n_{\text{eff}} L}{(2m-1)(2m+1)} \tag{1-8}$$

Equation (1-8) shows that the FSR between two interference dips depends on the interferometer length and the effective refractive index. Since the effective refractive index of the fiber is constant, the number of interference points observed in a limited measurement range can be controlled by the length *L*.

1.3 Graphene Oxide Coated Fiber Mach-Zehnder Interferometers

Graphene discovered by Nobel physics prize winners Andre Geim and Konstantin Novoselov in 2004 [44], opened a new era of two-dimensional material research, as shown in Figure 1-8 (a). Graphene is the basic building block of all graphitic forms (including carbon nanotubes, graphite and fullerene). Graphene has attracted researchers' attention because of its unique properties, such as its high surface area to weight, remarkable thermal and chemical stability, ultra-high mechanical strength, excellent electron transport properties, charge mobility, fascinating electronic and optical properties, and low production cost [45]. Since graphene atoms are surface atoms, graphene is sensitive to environmental factors. Different types of sensors can be developed using graphene-based nanostructures [46, 47, 48].

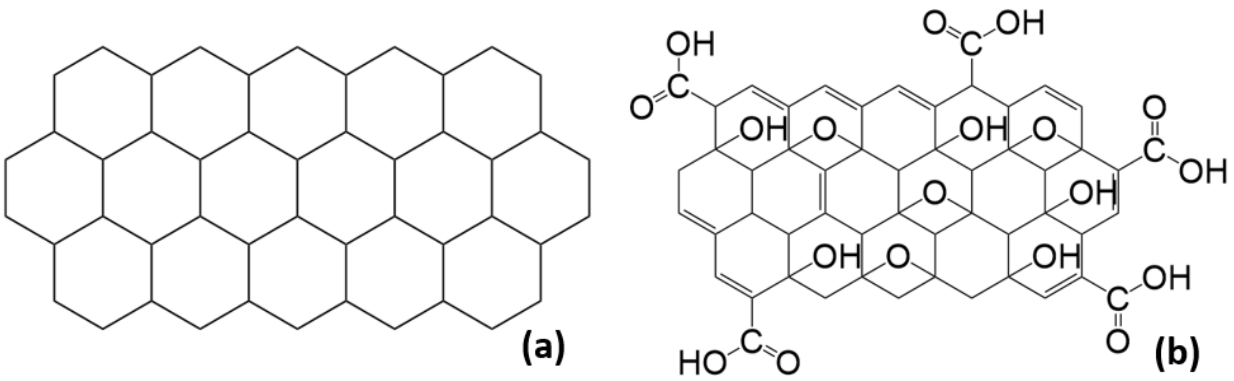

Figure 1-8: Chemical structures of: (a) Graphene, (b) graphene oxide.

Graphene oxide (GO) is a functionalized graphene derivative generally obtained by oxidizing graphite in strong acids and oxidizing agents, as shown in Figure 1-8 (b). When GO consists of fewer than ten layers, its refractive index is ~1.2 RIU, and it is anticipated that as the number of GO layers increases, the refractive index will increase [49]. The sensitivity of the sensor can be increased by coating multiple layers of GO to reduce the refractive index contrast (difference in refractive indices of the fiber core and GO cladding layer).

GO is also hydrophilic, has a large specific surface area (theoretical limitation: 2630 m^2/g), and its extensive oxygen-containing functional groups such as hydroxyl, carboxyl, and epoxide (mostly on the top and bottom surfaces) and carbonyl (mostly on the sheet edges) [50] facilitates its interaction with a wide variety of organic solvents [51]. As a result of the presence of carboxylic and hydroxyl groups, it disperses well in water and displays a strong negative charge at the surface. As a result of its negative charge and enriched functional groups, GO can interact with a variety of organic solvents and can also be easily deposited on a variety of substrates [52].

Recent studies have shown that graphene and GO-based coatings improve RI sensitivity, and nitrogen dioxide, ethanol, humidity, and heavy metals have been detected using this

technique. Moreover, the rich functional groups of GO make it suitable for immobilizing biomolecules for biosensing applications [52]. Because GO is hydrophilic, it is important to investigate the structure and dynamics of water molecules associated with GO intercalations below the threshold of water crystallization. These unique characteristics make it suitable for humidity sensors used as a humidity-sensitive film [53].

However, it is difficult to increase the coating thickness due to the electrostatic repulsion between graphene and oxygen-containing functional groups. It is less efficient if the coating thickness is increased by reducing the previous GO layer before each coating. Furthermore, the adhesive layer affects the properties of the coating if it is coated alternately with graphene oxide and the adhesive layer [54, 55]. Recently, there have been several methods for coating GO on optical fibers: the immersed method, dip-coated method, layer-by-layer method, optical deposition method, and in-situ layer self-assembly method.

Fan *et al.* presented a GO-coated FMZI humidity sensor to enhance the response to ambient water molecules [56]. The cladding of the few-mode fiber was partially etched and coated with a film layer by the immersed method and natural evaporation. After cleaning the fiber several times with alcohol, the sensing area was immersed in a sufficiently sized droplet of GO dispersion and let it naturally evaporate for 24 hours at 25℃. GO sheets were deposited on the fiber surface, and the concentration and volume of the GO solution could be used to adjust the thickness of the coating. At higher graphene concentrations, thicker GO films could be produced.

Mandeep *et al.* first investigated GO-coated LPG sensors using single-mode optical fiber to detect harmful gases such as carbon monoxide and methane in underground coal mines. Using

a customized holder and dipping and lifting speeds of 100 mm/min, a 40 nm thick layer of GO was applied to the sensing head [57].

Song *et al.* prepared graphene-coated conductive fibers by layer-by-layer negative and positive charged graphene oxide [54]. The carboxyl functional group of GO dispersion was ionized in the solution, resulting in a negative charge. $AlCl_3$ was used to reverse the change to a positive state. In this experiment, polyacrylonitrile fiber was coated with bovine serum albumin to facilitate adhesion to the first layer of GO. Positive and negative charge cycle coating produced conductive fibers with better electrical conductivity and enhanced coating efficiency than non-positive and negatively charged cycle coatings.

Tian *et al.* used an optically driven deposition method to coat a micro-nano fiber Bragg grating with GO film to make a humidity sensor [58]. The diameter of the fiber Bragg grating was etched to approximately 12 μm and applied a uniform film to the surface. A laser with a central wavelength of 1060 nm and a power of 75 mW was used to coat GO on the fiber Bragg grating for 20 minutes. The smaller the grating area diameter, the higher the sensitivity of the humidity sensor. Additionally, the larger sizes of GO flakes could enhance the absorption of water molecules. The GO solutions of different concentrations affected the thickness of the film coated on the fiber Bragg grating. It would reduce the capacity to absorb water molecules if the GO film was too thin (such as five layers, about 6 nm) or too thick (such as 20 μm). When the GO film was too thin, it absorbed very few water molecules, which narrowed the detection range of the humidity sensor. In contrast, if the coating thickness was too large, the inner layer of GO film would hardly change due to the limited permeability of absorbing water molecules.

Yang *et al.* proposed a compact S-tapered fiber humidity sensor using by in-situ layer-by-layer assembly (i-LbL) technique [59]. Chemical modification of the fiber surface and self-

assembly of the layers were the key components of the i-LBL technology. First, the prepared S-tapered fiber was immersed in acetone for 30 minutes to remove organic pollutants and then washed and dried using deionized water and ethanol. Almost all types of glass fibre were composed primarily of SiO_2. In alkaline solutions, hydroxyl ions attacked the SiO_2 framework according to the following equation: [60]

$$[-\mathrm{Si}-\mathrm{O}-\mathrm{Si}-]+\mathrm{OH}^{-} \overset{\Delta}{\rightarrow} [-\mathrm{SiO}]^{-}+[\mathrm{Si}-\mathrm{OH}] \tag{1-9}$$

According to Eqn. (1-9) OH groups were added to fiber surfaces by immersing them in 1.0 M NaOH solution for two hours. Next, it was rinsed thoroughly with deionized water and absolute ethanol to remove the extra NaOH solution. In the third step, the dried S-tapered fiber was immersed in 5 wt% (3-Aminopropyl) triethoxysilane (APTES) for 4 hours, and the hydroxyl groups on the silica surface reacted with the APTES to form a Si-O-Si bond. Then the S-tapered fiber was removed, washed thoroughly with ethanol, and heated at 95°C for 10 min. Electrostatic forces were used to adhere negatively charged GO nanosheets to APTES-silanized fiber surfaces due to positively charged amino groups (NH_2) on the fiber surface. The S-tapered fiber was placed in a groove and immersed in the GO solution. As the GO solvent in the groove volatilized, the GO nanosheets were adsorbed to the surface of the S-tapered fiber. A clear brownish coating formed by repeating this process twelve times. The number of cycles could control the thickness of the coating.

Chapter 2 Fabrication and Properties of Graphene Oxide Coated Fiber Mach-Zehnder Interferometers

The microstructured fiber can be fabricated by stretching or fusing a standard telecommunication single-mode optical fiber (SMF-28, Corning Inc.) using a FITEL S182A optical fiber fusion splicer. An optical fiber fusion splicer is a device that uses an electric arc to melt the ends of two fibers together to form a single long fiber. By adjusting the arc power, arc time and stretching or pushing distance through manual operation, fibers of various waist diameters can be fabricated. This study discusses two types of microstructured fibers: tapered fiber and bulge-fused fiber.

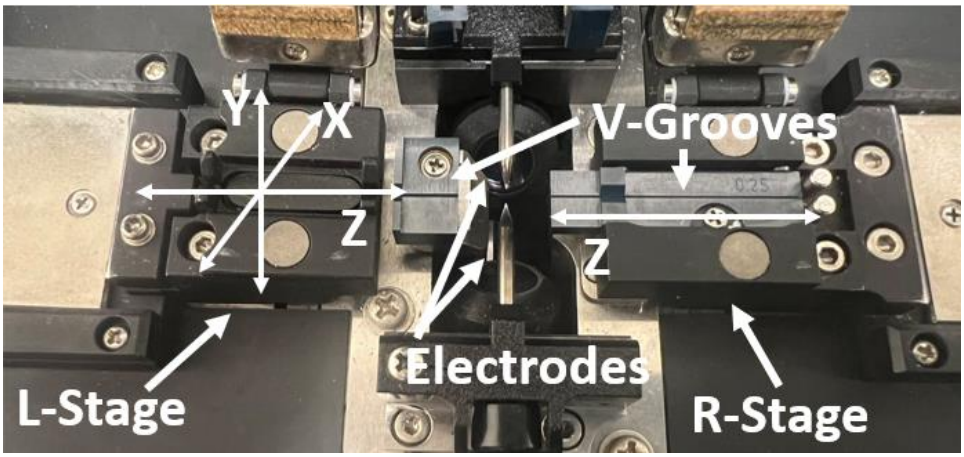

Figure 2-1: Schematic illustration of the components of the fusion splicer.

Figure 2-1 shows that the fusion splicer components consist of moving stages (L-stage and R-stage), V-grooves, and electrodes. Electrodes generate arcs, while the strength of the arc can be determined by arc power. The R-stage is a "fixed stage" that only moves in the Z direction, whereas the L-stage is a "calibration stage" that moves in three directions (X, Y, Z).

A step prior to fusion is called "impurity burn-off." It is a precautionary cleaning step where the electrodes generate an arc to burn off any remaining dust or moisture from the fiber surface. The discharge time of the arc can be set by “per-fuse” time setting. In the fusion step, the electrodes emit a second arc that fuses the fiber ends together to form a permanent splice. The arc time for this process can be set by “arc duration” setting, and both moving stages move inward while discharging to ensure the fiber ends are fused.

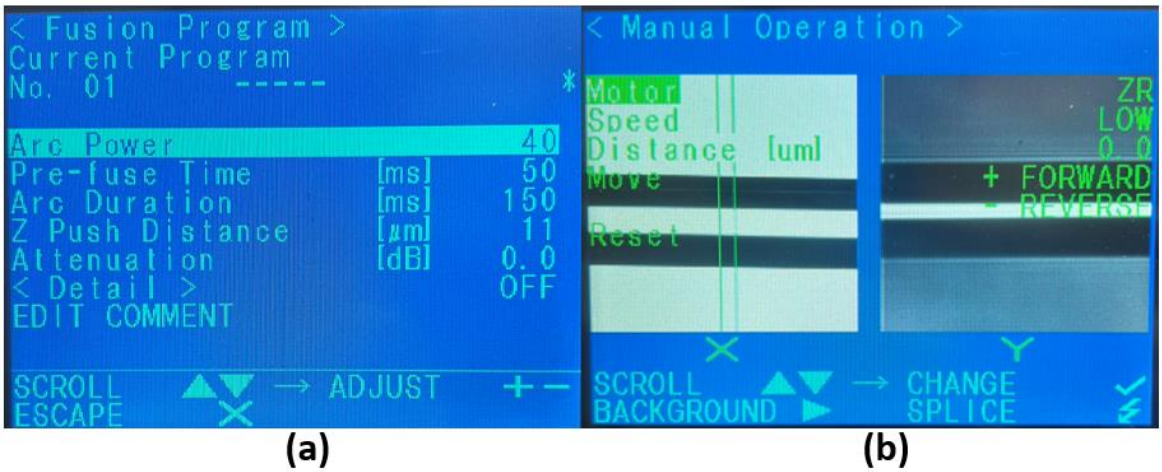

Figure 2-2: Control panel of the fusion splicer. (a) Setting window, (b) manual operation window.

According to Figure 2-2 (a), arc power is the value set through the control panel. Pre-fuse time and arc duration having units in microseconds (ms). The moving distance of both stages during the fusion process is determined by the Z push distance measured in micrometres (µm). In Figure 2-2 (b), on the left is the top view of the optical fiber (X), and on the right is the side view of the optical fiber (Y). The vertical lines above the X can identify the arc discharge area.

2.1 Fabrication of Optical Fiber Tapers

In order to prepare tapered fibers, the fiber is heated and stretched to reduce the waist diameter. To achieve the fabrication of tapered optical fiber with a fusion splicer, the effect of different factors on the waist diameter is analyzed in this experiment by a statistical software package Design-Expert 12 (Stat-Ease Inc.) using Box-Behnken design (BBD). In statistics, BBD is a design of experiments for response surface methodology introduced by George E. P. Box and Donald Behnken in 1960 [61]. It is an independent, rotatable quadratic design that requires three levels of each factor with no embedded points. In this design, the variable combinations are at the midpoints of the edges of the variable space and the center, as shown in Figure 2-3 [62]. BBD can analyze the relationship of each factor with the response with fewer design points.

In this analysis, the fiber waist diameter is defined as the response, and three main factors that change the waist diameter during fabricating are arc power (*A*), discharge time (ms) (*B*), and separation distance (μm) (*C*). Each factor contains three levels, usually coded as −1, 0, and +1, where −1 and +1 are the minimum and maximum values of the factor, respectively, and 0 is the center value. Table 1 shows the parameters of the experiment, and Table 2 shows the random data input. The experiment repeats three times to ensure stability, and the response (waist diameter) shown in Table 2 is the average of the three measurements.

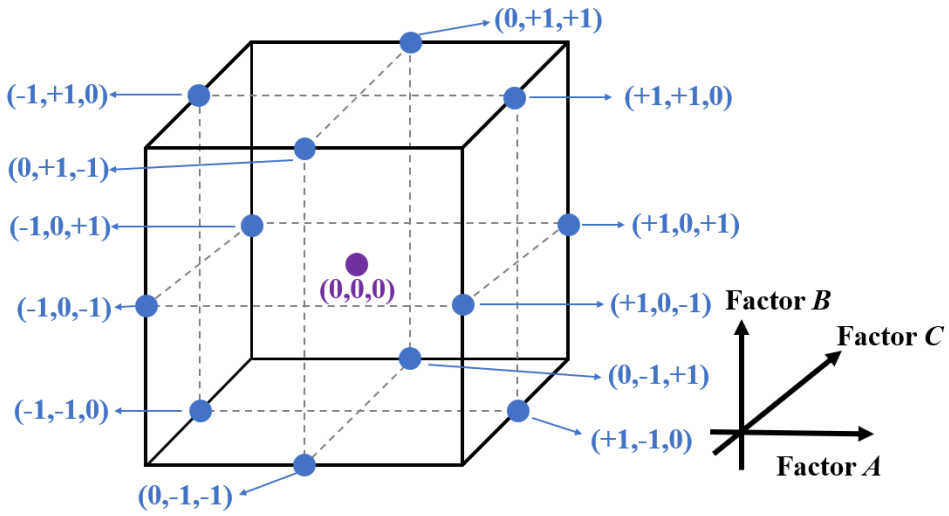

Figure 2-3: Box-Behnken design cube with the center point (0,0,0) and twelve combinations of three factors (*A*, *B*, *C*) with three levels each.

Table 1: Parameters for the Box–Behnken design test.

Parameters	No.	Items			
Factor	3	Arc power (*A*) Time (ms) (*B*) Separation distance (μm) (*C*)			
Level	2	Factor level	−1	0	+1
		Arc power	20	30	40
		Time (ms)	50	100	150
		Separation distance (μm)	300	400	500
Response	1	Diameter of tapered fiber			
Replications	3	All factors			

The arc power in this experiment ranges from 20 to 40, with a midpoint of 30. Time intervals range from 50 to 150 ms, and separation distances range from 300 to 500 μm. Additionally, approximately 3.0 cm of the protective jacket is removed before the experiment using a fiber-optic stripper (CFS-2) and wiped with ethanol. To straighten the fiber, a 7.85×10^{-3} Newtons (0.8 g) weight is suspended on the fiber end to apply a pre-stress. After manufacturing the tapered fibers, a microscope (Leica Microsystems Wetzlar GmbH) is used to observe the surface morphology. The waist diameter and taper length are measured by image processing software (Quartz PCI), as shown in Figures 2-4.

Table 2: Randomized data input in Design Expert 12 software.

Factor *A*	Factor *B*	Factor *C*	Response
Arc Power	Time (ms)	Separation distance (μm)	Waist diameter (μm)
40	50	400	62.2
20	50	400	66.4
30	50	500	49.1
30	50	300	90.2
30	100	400	67.6
20	100	300	89.8
40	100	500	43.3
40	100	300	83.5
20	100	500	51.6
30	100	400	68.6
30	100	400	65.4
40	150	400	66.1
30	150	300	89.7
30	150	500	49.4
20	150	400	72.7

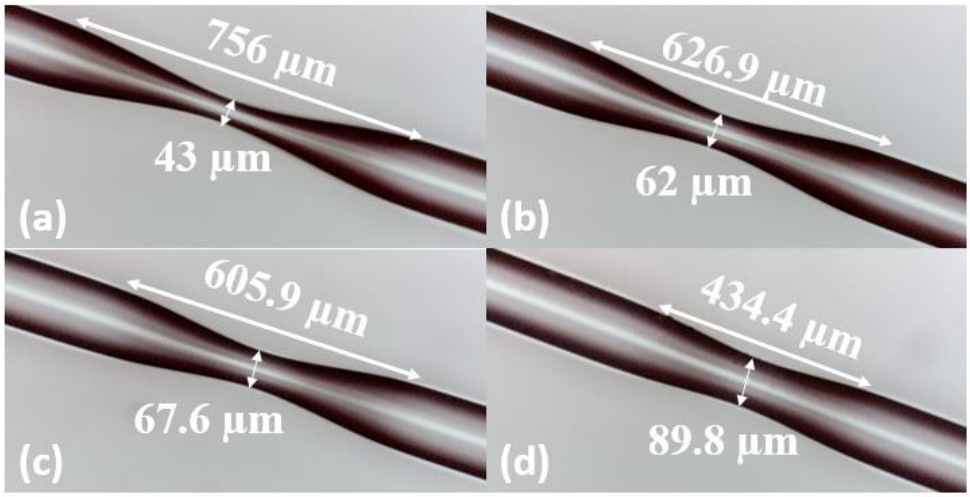

Figure 2-4: Tapered fiber at the run number: (a) 4; (b) 10; (c) 14; and (d) 2.

Figure 2-5 shows that the taper length increases as the diameter decreases. After analyzing the data with a linear fit, the relationship between those two factors can be calculated by:

$$\text{Taper Length} = -4.91 \times \text{Waist Diameter} + 944.67\ \mu\text{m}$$

The coefficient of determination (R^2) is 0.955.

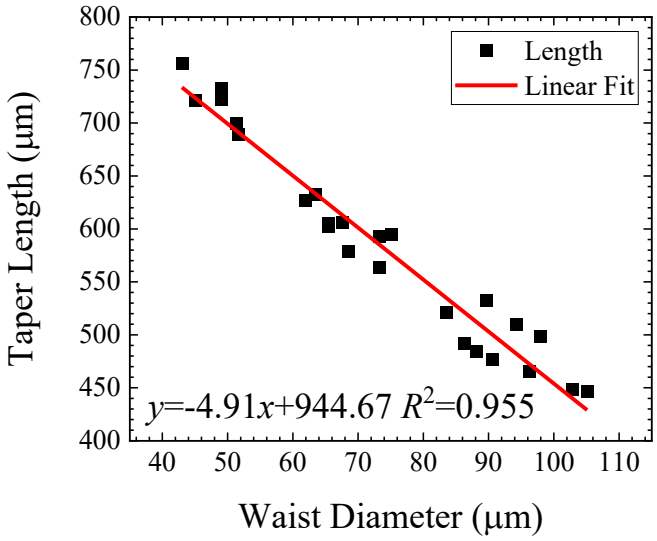

Figure 2-5: Relationship between waist diameter and taper length.

Table 3: ANOVA for linear model.

Source	Sum of Squares	df	Mean Square	*F*-value	*p*-value	
Model	3306.98	3	1102.33	280.69	< 0.0001	significant
A -Arc Power	83.21	1	83.21	21.19	0.0008	significant
B -Time	11.76	1	11.76	2.99	0.111	not significant
C -Separation Distance	3212.01	1	3212.01	817.90	< 0.0001	significant
Residual	43.20	11	3.93	–	–	–
Lack of Fit	37.84	9	4.20	1.57	0.449	not significant
Pure Error	5.36	2	2.68	–	–	–

Analyzing the data collected by BBD with analysis of variance (ANOVA) gives the effect of each factor on the waist diameter. ANOVA is the process of analyzing differences in means using statistical models and their associated estimation procedures. The degrees of

freedom (df) is the number of independent pieces of information. The *F*-value is variation between sample means. The *p*-value is a number calculated from a statistical test that describes the probability that the experimental results will remain unchanged when the experimental parameters are changed. A larger *p*-value for a factor indicates that the factor influences the experimental results less. This analysis defines a *p*-value less than 0.05 as significant for the experimental results. Residual means the sum of squared errors, lack of fit is the variation between the actual measurements and the values predicted by the model, and pure error is the variation among replicates [63].

According to Table 3, the *p*-value of the model is less than 0.05, which means that the factors selected in this model are valid. In this case, the effects of arc power and separation distance on the waist diameter are significant. Since the *p*-value of time is greater than 0.1, this indicates that time is associated with high uncertainty and has a relatively small effect on the results. The *p*-value of lack of fit is 0.449 implies that the lack of fit is insignificant, which means the model fits with the linear model.

Figure 2-6 shows a 3D surface of the diameter change of the waist diameter influenced by the arc power and the separation distance at a time of 50 ms. The final equation in terms of factors can be calculated as follows:

$$\text{Waist diameter} = 153.77\ \mu\text{m} - 0.348 \times A + 0.0268 \times B - 0.197 \times C \quad (2\text{-}1)$$

From the Eqn. (2-1), both factors *A* (arc power) and *C* (separation distance) are inversely proportional to the waist diameter, but factor *B* (time) has a positive effect on the waist diameter. The waist diameter of the tapered fiber can be calculated to be 72.4 μm by using Eqn. (2-1) when the arc power, time, and separation distance are 40, 50 ms, and 350 μm, respectively. Then apply the above parameters to the fusion splicer and repeat the preparation 15 times to measure the stability of the fabrication, shown in Figure 2-7.

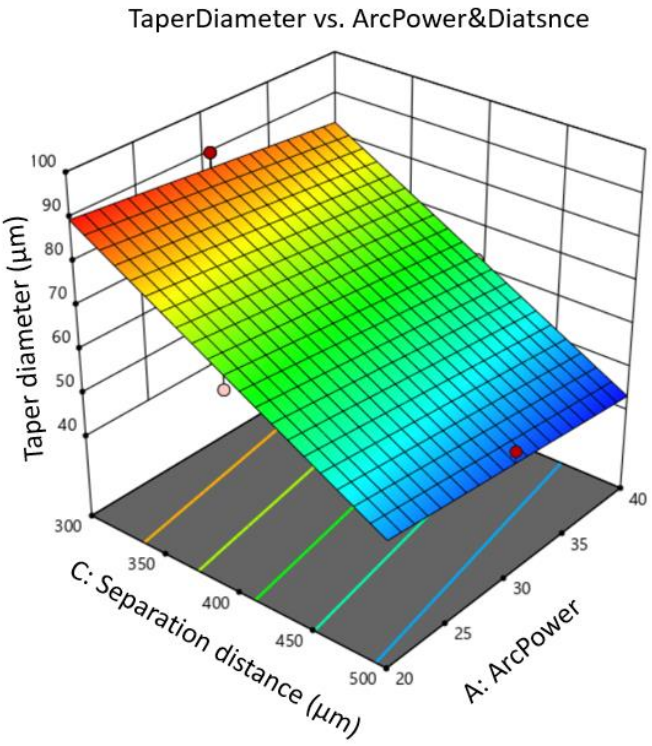

Figure 2-6: Corresponding 3D surface of the tapered fiber model.

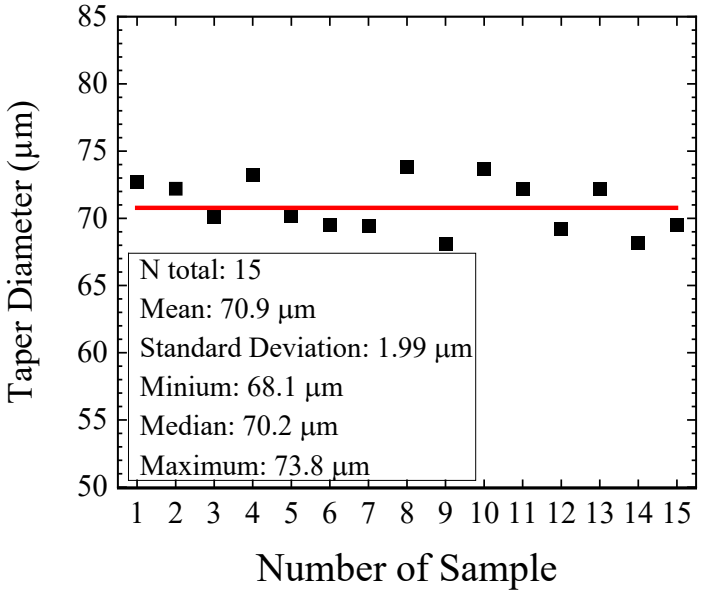

Figure 2-7: Diameter of tapered fibers during repeated preparation.

Figure 2-7 shows the average waist diameter is 70.9 μm, and the standard deviation is 1.99 after repeating the preparation 15 times. The maximum waist diameter is 73.8 μm, while the

minimum is 68.1 μm. By using the equation of percentage error, the error between the calculated diameter and the average diameter is (|70.9 μm - 72.4 μm| / 72.4 μm) × 100% = 2.07%. The error percentage is less than 5.00%, so this process is stable.

Based on waveguide theory, when light propagates along an optical fiber core, part of the light will attenuate exponentially in the cladding. There is no interaction between the evanescent field and the external medium surrounding an optical fiber with a uniform core diameter. This is because the skin depth of the evanescent field is much smaller than the thickness of the cladding. The skin depth (d_s) is defined by: [64]

$$d_s = \frac{\lambda}{2\pi\sqrt{n_{\text{core}}^2 \sin^2(\theta_i) - n_{\text{clad}}^2}} \tag{2-2}$$

The taper structure shown in Figure 2-4 can be simplified as two conical shapes joined at the top, as illustrated in Figure 2-8. The diameter of the fiber core in the taper region decreases on an equal proportion as the diameter of the cladding shrinks during the arc discharge process. In order to verify the propagation of incident light energy, a 2-D finite element analysis has been performed on the tapered fiber junction. This simulation is performed using the commercial simulation software COMSOL Multiphysics. Firstly, the geometry of the fiber taper is drawn using the Polygon Mode. Then, in the Subdomain of material mode, the refractive indices of the cladding and core are defined. The refractive index of the core is 1.4450, and the refractive index of the cladding is 1.4404 in this simulation [65].

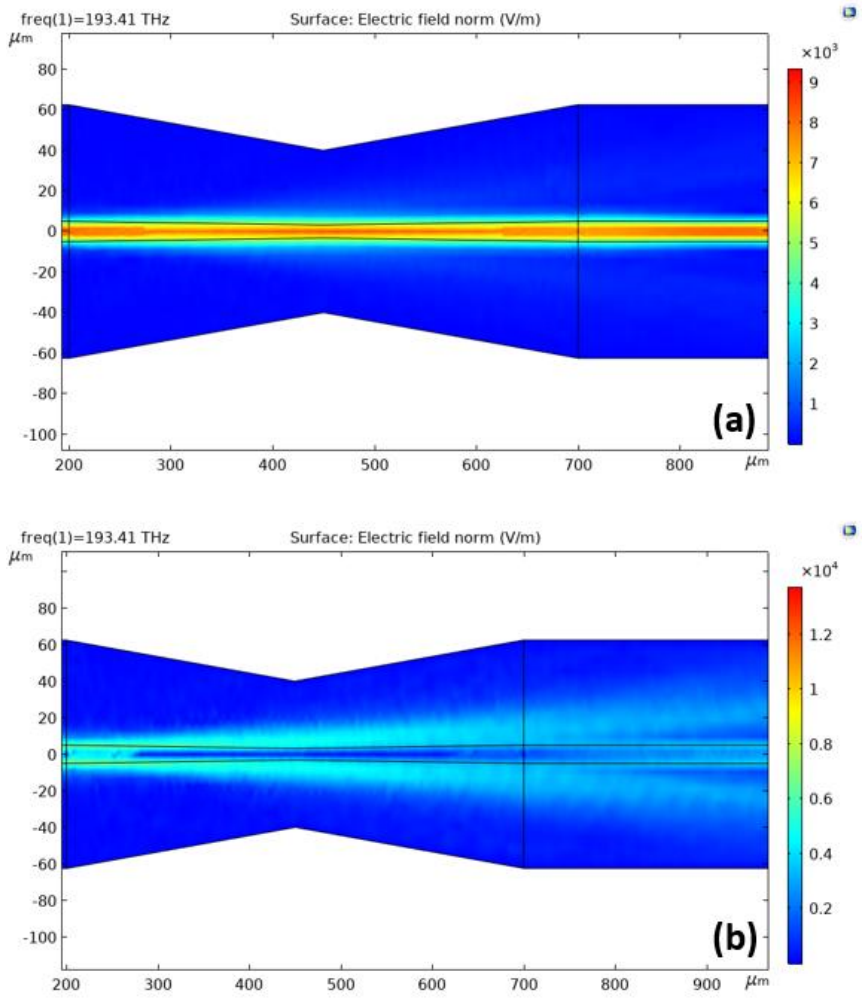

Figure 2-8: Schematic illustration of light energy density distribution along a tapered optical fiber with a diameter of 75 µm at wavelength 1550 nm. (a) Number of modes as 1, (b) number of modes as 2.

The electromagnetic parameters are defined by "Electromagnetic Waves, Beam Envelopes Mode," such as free space wavelength and incident electric field. The electric field components are chosen to be an out-of-plane TE wave, and the upper and lower parts of the geometry are defined as scattering boundary conditions. The Boundary modes analysis is applied to define the intensity distribution of the electric field in the *x*-direction, and the equation applied in the Boundary Mode is (COMSOL Multiphysics 5.5):

$$(\Delta - ik_1) \times \mu_r^{-1}\left((\nabla - ik_1) \times E_1\right) - k_0^2\left(\epsilon_r - \frac{j\sigma}{\omega\epsilon_0}\right)E_1 = 0 \tag{2-3}$$

$$\lambda = -j\beta - \delta_z \tag{2-4}$$

where μ_r, ϵ_r, σ, and ω are the relative permeability, relative permittivity, electrical conductivity of the material, and angular frequency, respectively. The parameters j and β are constant in COMSOL. E_1 is the beam envelope, k_1 is the phase $(\vec{k} \cdot \vec{r})$, $\vec{k}$ is a wave vector, and $\vec{r}$ is the position.

For the tapered fiber, the excitation energy of LP_{01} in fibre core mode will be partly coupled to cladding modes at the beginning of the fibre taper region, shown in Figure 2-8 (a). As a result of the reduction in core diameter and the larger diameter of the cladding, high-order LP_{0n} cladding modes propagate through the cladding. Figure 2-8 (b) depicts how the high-order mode propagates when the desired number of modes is 2.

2.2 Simulation and Fabrication of Tapered Fiber Mach-Zehnder Interferometers

A symmetrically tapered fiber Mach-Zehnder interferometer optical sensor consists of two tapered fiber structures. Eqn. (2-2) shows that the skin depth depends on the complementary incident angle (θ_i). In the tapered region, when the light propagates in the z-direction, the θ_i at the core-cladding interface is affected by the geometry of the tapered structure, as shown in Figure 2-9, where $\theta_i \propto \tan^{-1}(2T_d / T_l)$. T_d is the taper depth, and T_l is the taper length.

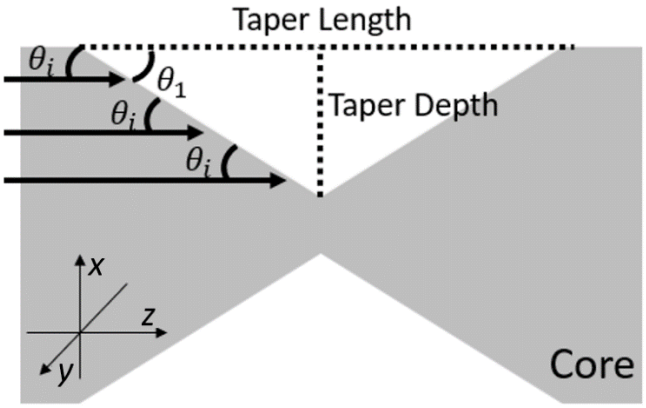

Figure 2-9: Schematic diagram of the light propagating in the *z*-direction with complementary incident angle θ_i, and θ_1 is the angle of the taper.

In COMSOL Multiphysics software, the Beam Envelopes module can be used to simulate the relationship between different tapered waist diameters and transmission spectra of the FMZI. As a result of the symmetry of the cylindrical waveguide, a two-dimensional finite element analysis has been performed on a symmetrical tapered FMZI. The model settings are the same as the single-tapered fiber. The geometry structure and the light energy density distribution of FMZI are shown in Figure 2-10. The FMZI is composed of two identical tapered fibers. In this model, the distance between the two tapered waists is 2.03 cm, while the effective refractive index Δn_{eff} is chosen to be 0.00465. Once the light is incident through port 1, it passes through two tapered sections and then comes out through port 2. The transmission spectrum can be obtained by measuring the transmittance of port 2 (ewbe.Tport2) in the “Wavelength Domain” mode. Different waist diameters can be simulated with the "Parametric Sweep" subset, where the waist diameter is set from 50 to 100 μm.

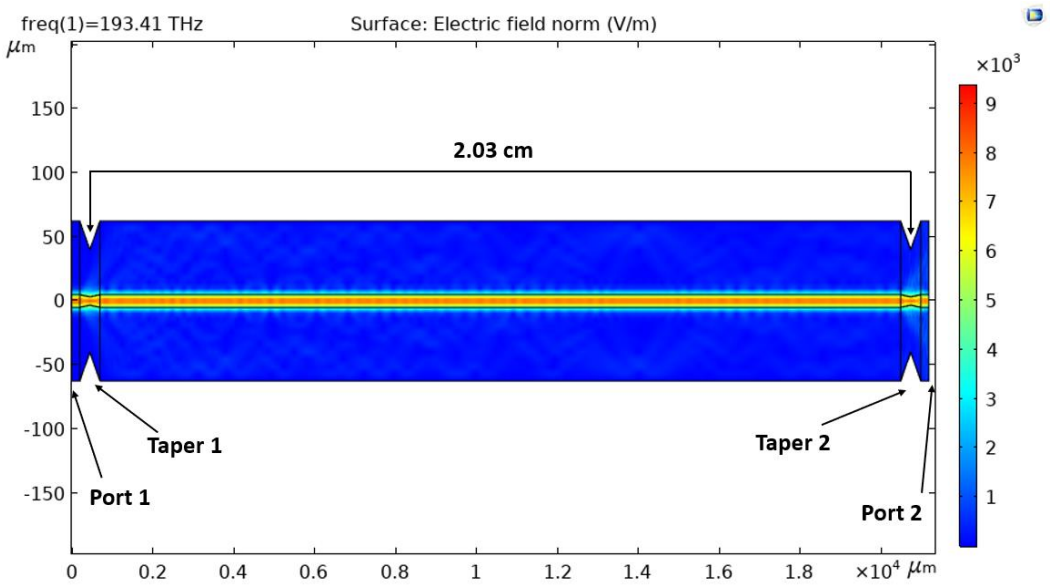

Figure 2-10: Schematic illustration of light energy density distribution along a symmetrical tapered FMZI with a diameter of 75 μm at a wavelength of 1550 nm.

Eqn. (1-7) can be used to identify the interference order:

$$m = \frac{\Delta n_{\text{eff}} L}{\lambda_m} - \frac{1}{2} \tag{2-5}$$

The transmission spectra of FMZI with different waist diameters are shown in Figure 2-11 (a). When the waist diameter exceeds 70 μm, three distinct wave dips can be found in the transmission spectrum in the 1520 to 1610 nm wavelength range. Dips 1 to 3 are defined from left to right. Figure 2-11 (a) shows that the intensity of the transmission spectrum decreases when the diameter becomes smaller. When the diameter is greater than 80 μm, the intensity of those dips decreases inversely with the diameter of the waist.

The interference order *m* can be determined by substituting the dip wavelength into Eqn. (2-5). The order *m* for dip1 is calculated to be 61. From Figure 2-11 (b), the dip m_{61} shows a blue-shift with decreased waist diameter. The FSR of dip1 also shows a nonlinear relationship with the function of waist diameter. The diameter appears to have a greater effect on the FSR

when it is lower than 70 µm. On the other hand, the effect of the waist diameter on the FSR is relatively small when it is greater than 70 µm.

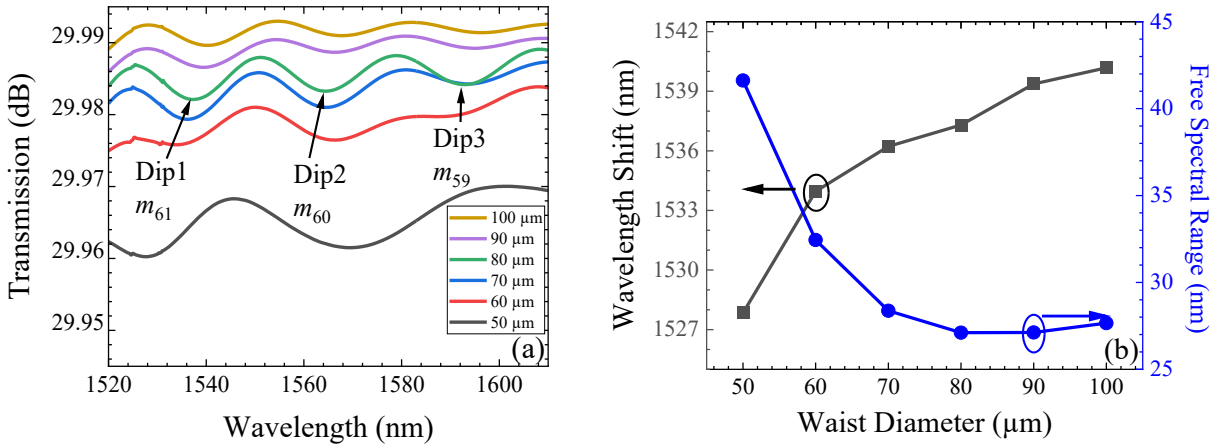

Figure 2-11: Symmetrical tapered FMZI with different waist diameters spaced at 2.03 cm. (a) Transmission spectra. (b) Wavelength shifts and FSR for dip m_{61}.

Since the tapered portion of the fiber has poor mechanical properties, it is necessary to consider the strength of the fiber itself while ensuring the signal strength of dips in the transmission spectrum. In this study, the waist diameter is chosen between 70 and 80 µm.

In Figure 2-12 (a), transmission spectra are shown for four different taper separations from 1520 to 1610 nm in the wavelength range. It can be found from the above figure, as the interval increases, more dips are visible in the same wavelength domain. In addition, with an increase in the taper separation, the intensity of the transmitted light decreases as well. The dip around 1543 nm (dip 1) is selected to analyze the free spectral range (FSR) of each spectrum. Figure 2-12 (b) shows the wavelength difference between dip 1 and its higher-wavelength neighbouring dip (dip 2) of the simulated spectrum and the calculated results of FSR of dip 1.

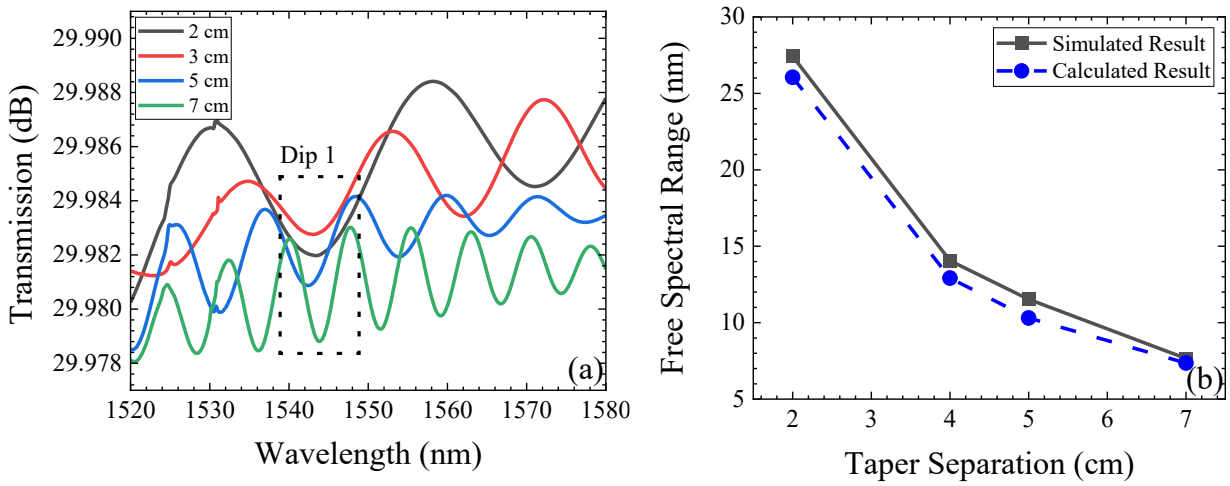

Figure 2-12: Symmetrical tapered FMZI with 75 µm waist diameter and different taper separations. (a) Transmission spectra. (b) Simulated and calculated results of FSR.

By substituting Eqn. (2-5) into Eqn. (1-8), the FSR can be found as follows:

$$\mathrm{FSR} = \Delta\lambda_m = \frac{\lambda_m}{\frac{\Delta n_{\mathrm{eff}} L}{\lambda_m} - 1} \tag{2-6}$$

The interference order m for each dip is shown in Table 4. Whenever the dip wavelengths of FMZI with different taper separations overlap, the distance L and the order m are linearly related.

Table 4: Position of the dip wavelength and the interference order.

Taper separation (cm)	Dip 1 (nm)	Dip 2 (nm)	Simulated FSR (dip2-dip1)	Dip 1 Order m	Calculated FSR
2	1543.15	1571.08	27.93	60	26.05
4	1543.87	1557.93	14.05	120	12.93
5	1542.43	1553.96	11.53	150	10.31
7	1543.87	1551.53	7.66	210	7.36

To supplement the simulation results, tapered FMZIs with a waist diameter of 70 µm are selected in the following investigation, which are fabricated with the following settings in the fusion splicer: arc power 40, pre-fuse time 50 ms, and stretching distance 350 µm. Since the

length between the two stages of the fusion splicer is 3 cm, the maximum distance between the two tapers cannot be greater than 2.5 cm. In this experiment, the FMZI has been fabricated in the configuration shown in Figure 2-13. Prepare the fiber by removing approximately 3.0 cm of the protective jacket using a fiber stripper. Once the jacket is removed, gently wipe the exposed fibers with ethanol to remove any impurities or contaminants. Then the prepared fiber is placed on the fusion splicer for the following steps. One end of the fiber is secured with tape to a linear translator (Thorlabs). Subsequently, a 0.8 g mass is suspended on another end of the fiber to straighten the fiber to make the first taper region; then, the translation stage will move by 0.8 inches (2.03 cm) to form another taper.

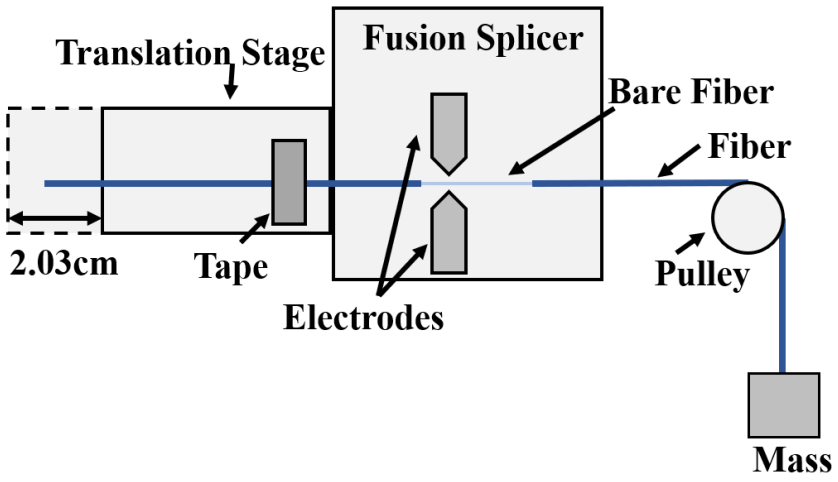

Figure 2-13: Schematic diagram of the setup for FMZI fabrication on single-mode fiber.

After the FMZI sensor is fixed on the glass slide, the transmission spectrum of the FMZI is measured using an Er^{3+} broadband source (EBS-7201) and an optical spectrum analyzer (OSA). Figure 2-14 illustrates the emission spectrum of the broadband light source used in this study. In the range between 1520 and 1610 nm, the output of the light source shows a clear and intense spectrum. This range is selected for this study to measure the spectrum of FMZI. During

the measurement of the transmission spectrum of FMZI, interference from the light source can be removed by subtracting the spectrum of the light source from the measured spectrum.

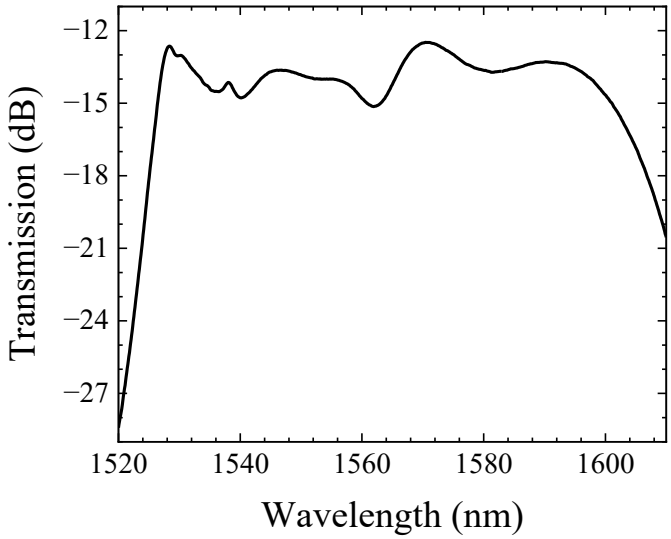

Figure 2-14: Emission spectrum of Er^{3+} broadband source.

The transmission spectrum of an FMZI with waist diameters 72.4 and 74.6 μm is shown in Figure 2-15. The figure shows three distinct wavelength dips at 1539.53, 1561.31, and 1584.44 nm. Eqn. (2-5) can be used to calculate the interference order for those dips. As shown in the figure below, m is 61, 60, and 59 from left to right. The interference order m is inversely proportional to the dip wavelength. Eqn. (2-6) can be used to determine the FSR of each dip at 23.54 ($\Delta\lambda_{61}$), 24.21 ($\Delta\lambda_{60}$), and 24.94 nm ($\Delta\lambda_{59}$), respectively. As the interference order decreases, the FSR increases. In the actual situation, the FSR between dips m_{61} and m_{60} ($\Delta\lambda_{61}$) is 21.78 nm with the interferometer length 2.37 cm, and the FSR between dips m_{60} and m_{59} ($\Delta\lambda_{60}$) is 23.13 nm with the interferometer length 2.30 cm. The actual FSR is smaller than the calculated FSR. The waist diameter of the tapered structure will affect the interference length, thus making the FSR smaller.

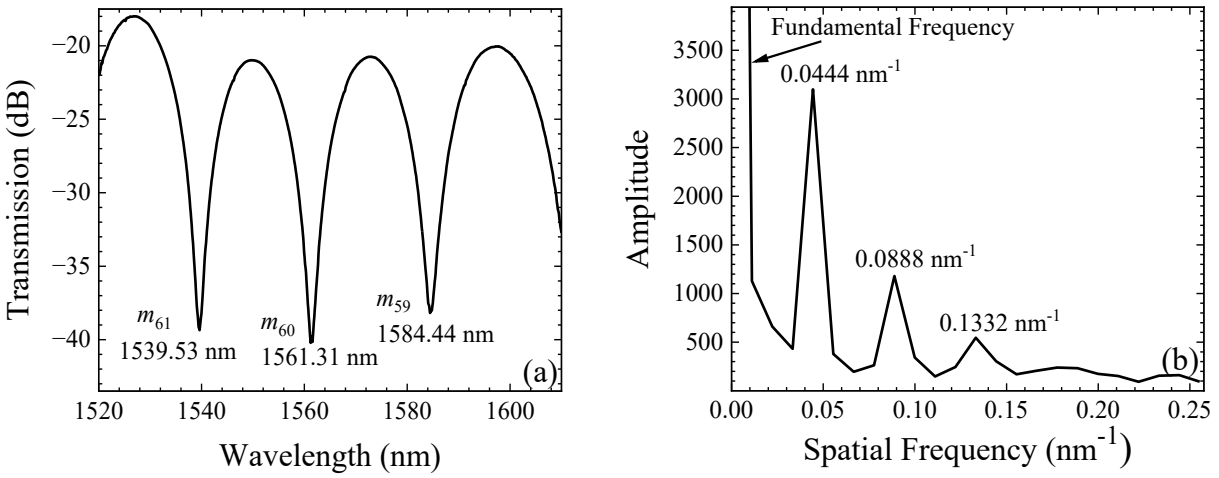

Figure 2-15: Symmetrically tapered FMZI with an interferometer length 2.2 ± 0.1 cm. (a) Transmission spectrum. (b) Fast Fourier transform of the tapered FMZI transmission spectrum.

Due to the large diameter of the cladding, multiple higher-order cladding modes will propagate through it. To further analyze the characteristics of the interference spectrum in Figure 2-15 (a), fast Fourier transform is adopted to analyze the spatial frequency domain, as shown in Figure 2-15 (b). The Fast Fourier Transform (FFT) is the name given to an efficient and fast computation method for computing the discrete Fourier transform using computers. It was developed by J.W. Cooley and T.W. Tukey in 1965 [66]. NumXL, a time series Excel add-ins suite, performs the FFT analysis. The discrete Fourier transform is defined as follows:

$$X_k = \sum_{j=0}^{N-1} x_j e^{-\frac{2\pi i}{N} jk} \tag{2-7}$$

where k is the frequency component, x_j is the values of the input time series, and N is the number of non-missing values in the input time series.

According to the Cooley-Tukey radix-2 decimation-in-time FFT algorithm, a DFT of size N is divided into two overlapping DFTs of size $N/2$ at each stage, as follows:

$$X_k \begin{cases} E_k + \alpha \bullet O_{\mathrm{k}}, & if\ k < \dfrac{N}{2} \\ E_{(\mathrm{k}-\frac{N}{2})} - \alpha \bullet O_{\left(k-\frac{N}{2}\right)}, & if\ k \geq \dfrac{N}{2} \end{cases} \tag{2-8}$$

where E_{k} is the DFT of the even-indices values of the input time series, x_{2n} (x_0 to $x_{\mathrm{N}-2}$), O_{k} is the DFT of the odd-indices values of the input time series, x_{2n+1} (x_1 to $x_{\mathrm{N}-2}$), n is an integer that represents the order of the data, and $\alpha = e^{-2\pi ik/N}$.

During the FFT, the wavelength spectrum changes to the spatial frequency domain. The scale of the x-axis after FFT (f_{m}) can be calculated by:

$$f_{\mathrm{m}} = \frac{m}{\Delta\lambda * N} \tag{2-9}$$

where $\Delta\lambda$ is the interval between each measurement in the wavelength domain.

The spatial frequency of the interferometer, shown in Figure 2-15 (b), clearly shows a dominant and strongly excited cladding mode and several weakly excited modes. There is a fundamental frequency between 0 and 0.0100 nm^{-1}, which indicates the characteristics of the light when it passes through the fiber core without coupling to the cladding. The dominant peak at 0.0444 nm^{-1} indicates the dominant waveform of the transmission spectrum. Since the light is transmitted in mode LP_{01} in the fiber core, this peak is regarded as an interference pattern formed by the light in both the cladding and the core in mode LP_{01}. Multiple high-order LP_{0n} cladding modes propagate through the cladding due to reduced core diameter and increased cladding diameter. At the second taper, the LP_{0n} cladding mode will combine with the LP_{01} core mode to produce the interference pattern shown in Figure 2-15 (b) as peaks 0.0888 nm^{-1} and 0.1332 nm^{-1}.

In the interferometer, mode coupling and interference primarily occur between the cladding and core modes. In Figure 2-15 (b), other high-order cladding modes modify the main interference pattern, resulting in inhomogeneous interference.

2.3 Fabrication of Bulge-Fused Optical Fiber

According to Section 1.2.2, Figure 1-6 illustrates the configuration of various types of FMZIs. There are two ways to make the ball-shaped structure for mode combination by fusion splicer. In the first method, two optical fibers are placed in the machine simultaneously and repeatedly fused until the desired diameter is reached [67]. Alternatively, one end of the fiber can be manually spliced 5 to 6 times to produce a spherical structure. The resulting spherical structure can be arc discharged with the flat end of the other fiber to complete the splice [68]. The peanut-shaped structure can be formed by splicing two spherical structures [42].

In this study, the ball-shaped and peanut structures are combined to make an overlapping peanut structure (bulge-fused) by over-fusing the two spherical ends together. A controlled variable method is used to investigate the effect of arc power on the diameter of the spherical structure at the end of the fiber. The "Arc Duration" factor is set to 750 ms as the discharge time to prepare the spherical structures at the fiber ends. The “Z Push Distance” is set to be 11 μm. The fiber is cut with a fiber cleaver (FITEL model S323) and placed in the V-groove of the L-stage so that the flat end is moved to the center of the arc discharge zone (Figure 2-16). The flat end is treated with the discharge of different arc powers to form a spherical structure.

Four fiber samples have been prepared with four different arc powers. During the discharge process, the fiber end is heated and softened. Due to the surface tension of the material, the surface of the fiber end gradually tends to be curved during the cooling process. After a spherical structure is formed, it is fixed on a glass substrate and observed with a microscope.

When 100, 150, 200, and 250 units of arc power are applied to the fiber, the diameter of the fiber end will be 127.5, 130.5, 145.2, and 183.4 μm, respectively.

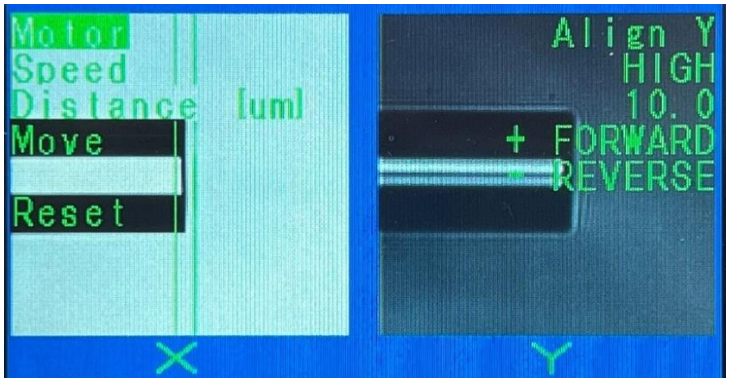

Figure 2-16: Operating interface of the fusion splicer.

Figure 2-17 shows that when the arc power is below 150 units, the structure of the fiber end is less affected by the discharge, a single discharge will only smooth its edges. The spherical structure formed on the end face of the fiber gradually becomes clearer as the arc power increases when the arc power exceeds 200.

As a result of setting the arc power to 250, the shape of the fiber end varies significantly. Multiple discharges can increase the diameter of the spherical structure. An arc power of 250 is used to determine the effect of the discharge position on the diameter of the spherical structure during multiple discharges. Three different positions are used to discharge the spherical structure of the fiber end: at its top, central, and bottom (Figure 2-18).

Figure 2-19 represents the relationship between the diameter of the spherical structure and the different discharge positions. The slope of the diameter versus the number of discharges are 15.22, 21.24, and 29.91, respectively, when the discharge position is at the top, middle, and bottom of the fiber end, shown in Figure 2-18. As the location of the repeated discharges gets closer to the bottom of the structure, the number of discharges has a larger effect on the diameter of the spherical structure.

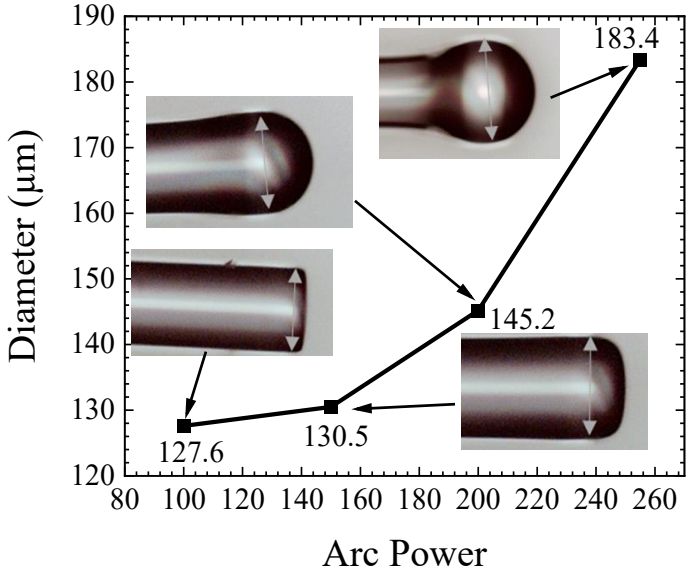

Figure 2-17: Diameter and structure of the fiber end after a single discharge with different arc powers.

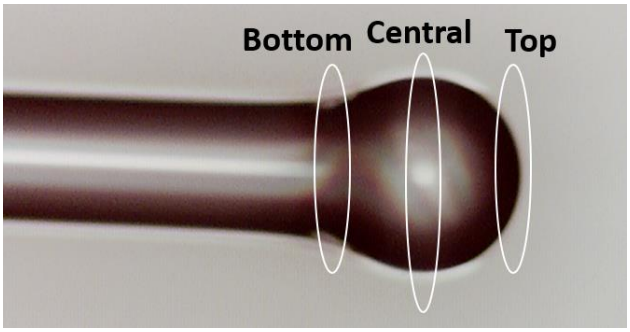

Figure 2-18: Three discharge positions choose to discharge six times.

A larger diameter can be achieved by discharging at the bottom of the spherical structure, as shown in Figure 2-19. The spherical shape at the end of the fiber sags away from its center after six discharges, as shown in Figure 2-19 (c). It shows that melting and cooling occur during the discharge process of fiber material. Due to the difference in the doping levels of GeO_2 between the core and cladding, the effective refractive index between the core and cladding decreases during the fiber melting process. Figures 2-19 (a) and (b) show the coefficient of

determination (R^2) of discharge position at the top and middle are 0.967 and 0.968, respectively. Discharge in the middle part is chosen to make the bulge-fused structure due to its higher slope of the diameter versus the number of discharges.

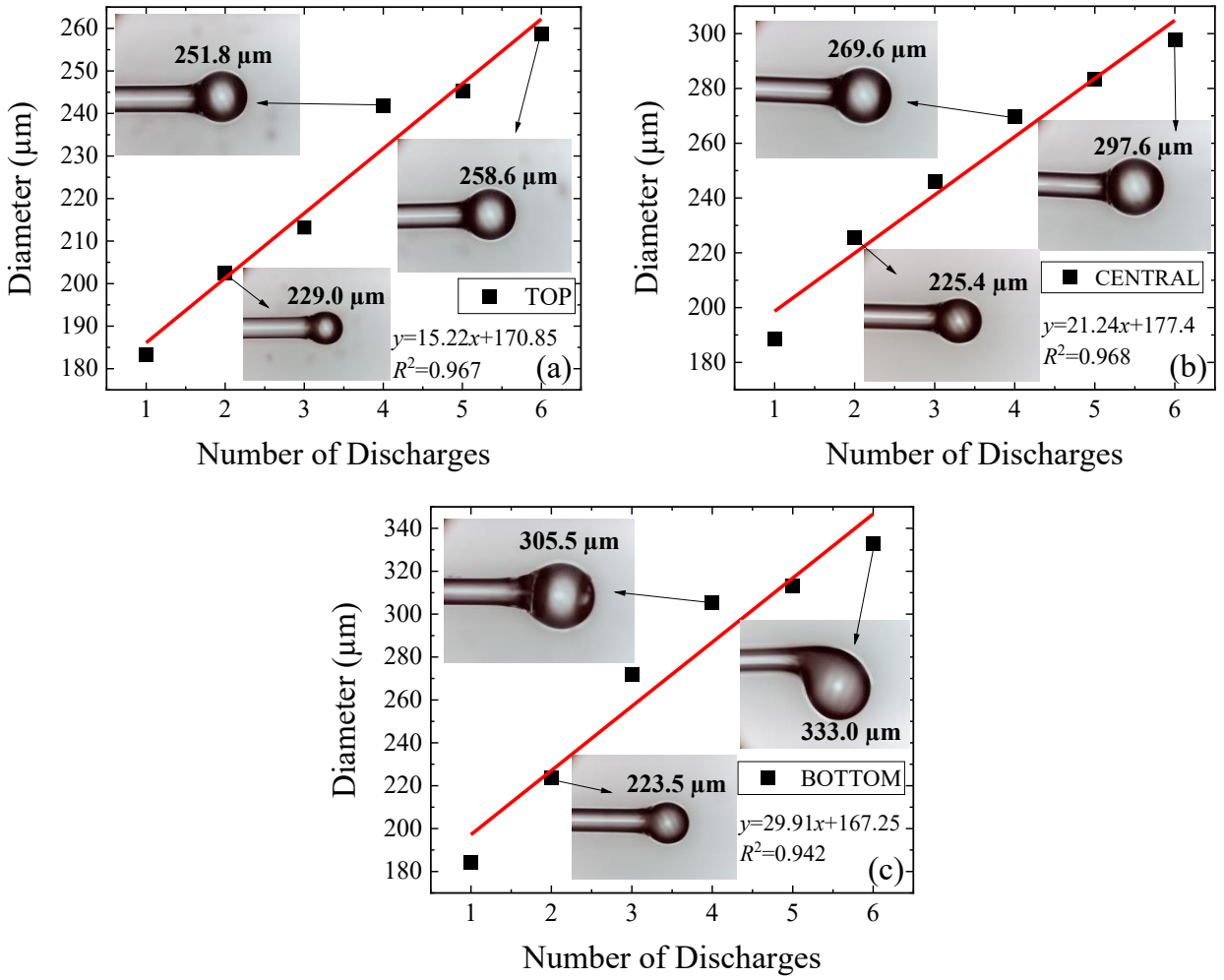

Figure 2-19: Relationship between the number of discharge times and the diameter of the spherical structure at different discharge positions. (a) Top, (b) central, and (c) bottom.

Fusion over two spherical structures forms a bulge-fused structure. During the fusion process, the fusion splicer is set to the following conditions: arc power 250, arc duration 750 ms, and Z push distance 11 μm. The transmission spectra of a single bulge-fused fibers are shown in Figure 2-20.

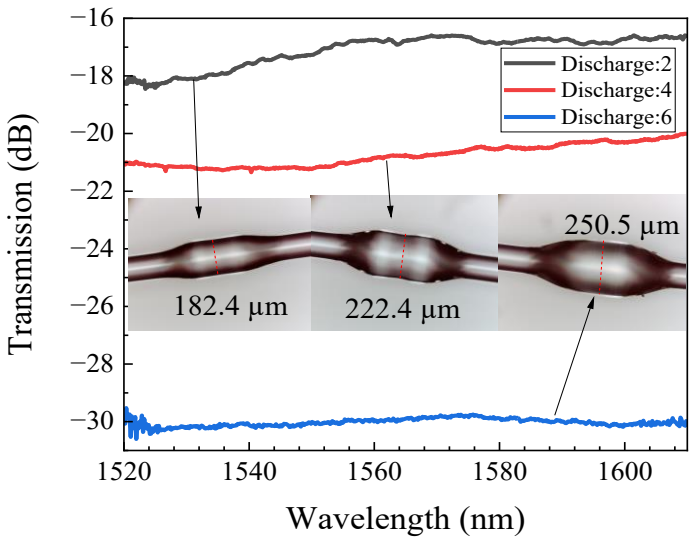

Figure 2-20: Transmission spectra of a single bulge-fused structure with different diameters.

Figure 2-20 shows the transmission spectrum of the bulge-fused structure formed by the fusion of two spherical structures prepared by different numbers of discharges. The diameter of the bulge-fused structure is proportional to the diameter of the spherical structure, but the diameter after fusion is smaller than the spherical diameter. In the case of a bulge-fused structure, the variation of the core diameter allows some of the light in the core to be coupled into the cladding, resulting in a transmission intensity that is inversely proportional to the diameter of the bulge-fused structure.

The bulge-fused structure can be further observed by tuning the focus of the microscope on the inside of the conical structure, as shown in Figure 2-21. Figures 2-21 (a) and (b) show the same fiber at different focusing conditions, suggesting that this structure has interconnected fiber cores. Furthermore, comparing the diameters of the cores inside the different structures (a, b, and d), the diameters are proportional to the diameters of the bulge-fused structures.

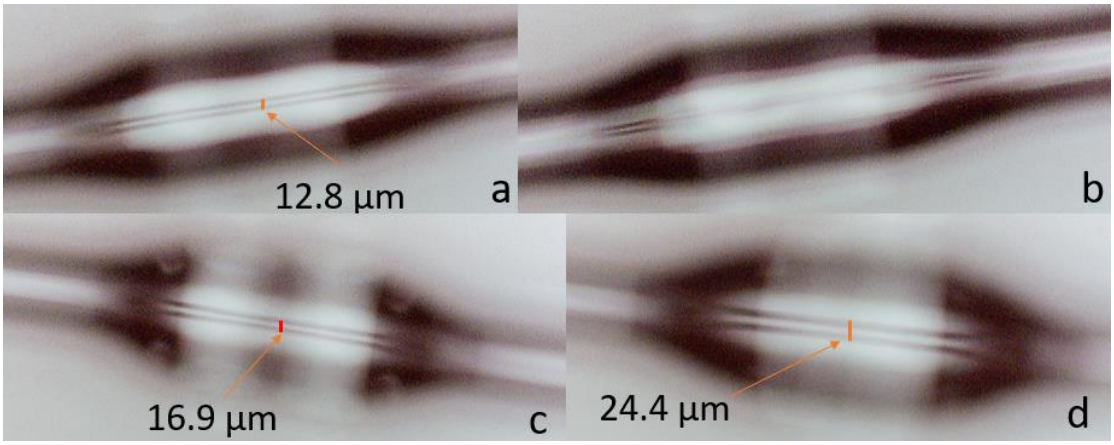

Figure 2-21: Internal structure of the bulge-fused structure. (a), (b) Shapes of core and side of bulge-fused structure prepared by secondary discharges, (b) and (c) core shapes within the bulge-fused structures with discharge numbers of 4 and 6.

To verify the propagation of incident light energy, a 2-D finite element analysis simulated by COMSOL Multiphysics has been performed on the bulge-fused fiber junction. The parameters used for the simulation are the same as in Section 2.1.

From Figure 2-22 (a), as the core diameter increases, the excitation energy of LP_{01} in fiber core mode is partially coupled to cladding modes at the beginning of the fiber taper region, and the reduction of the core diameter at the end of the structure makes core mode further coupled to the cladding mode. High-order LP_{0n} cladding modes propagate through the cladding due to the larger diameter of the cladding. Figure 2-22 (b) depicts how the high-order mode propagates when the desired number of modes is 2.

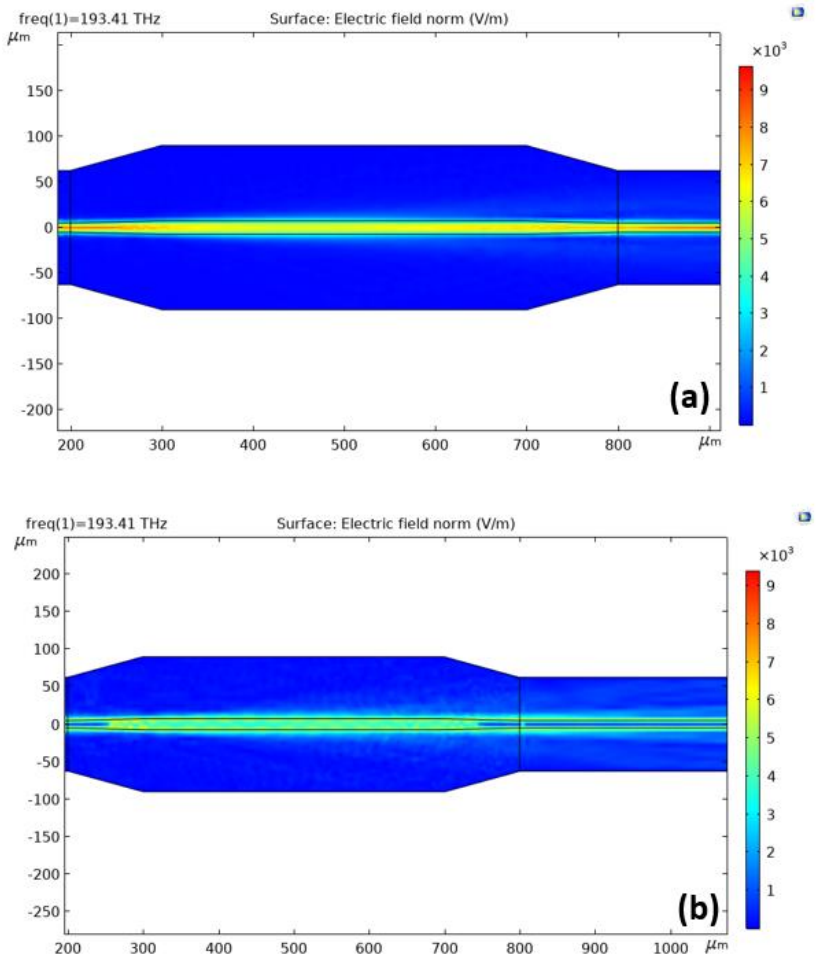

Figure 2-22: Schematic illustration of light energy density distribution along a bulge-fused optical fiber with a diameter of 180 μm at wavelength 1550 nm. (a) Number of modes as 1, (b) number of modes as 2.

2.4 Fabrication and Simulation of Symmetrical Bulge-Fused Fiber Mach-Zehnder Interferometers

A symmetrical bulge-fused Mach-Zehnder interferometric sensor consists of two bulge-fused junctions. The simulation of the relationship between different bulge-fused waist diameters and transmission spectra of the FMZI is conducted using the Beam Envelope module of COMSOL Multiphysics software. The parameters used for the simulation are the same as in Section 2.2.

The transmission spectra of FMZIs with different waist diameters are shown in Figure 2-23 (a). Three different dips can be observed in each of the transmission spectra. Dips 1 to 3 are labeled for dips from lower to high wavelength. It is evident from the figure that the intensity of the transmission spectrum decreases as the diameter becomes larger due to more light coupling to the cladding. Unlike the tapered structure, the depth of those dips is proportional to the diameter as the diameter increases. Increasing the diameter results in sharper interference fringes.

Eqn. (2-3) can be modified by substituting the dip wavelength to determine the interference order *m*. For dip 1, order *m* can be calculated as 61. Figure 2-23 (b) shows that when the waist diameter is smaller than 226 µm, the dip wavelength of m_{61} exhibits a red-shift with increasing waist diameter but stays constant when the diameter exceeds 226 µm. The FSR of dip m_{61} shows a nonlinear relationship with the change in the waist diameter. Due to the low dip intensity, the FSR remains constant when the diameter is smaller than 178 µm. However, when the diameter is larger than 178 µm, the FSR increases with increasing diameter.

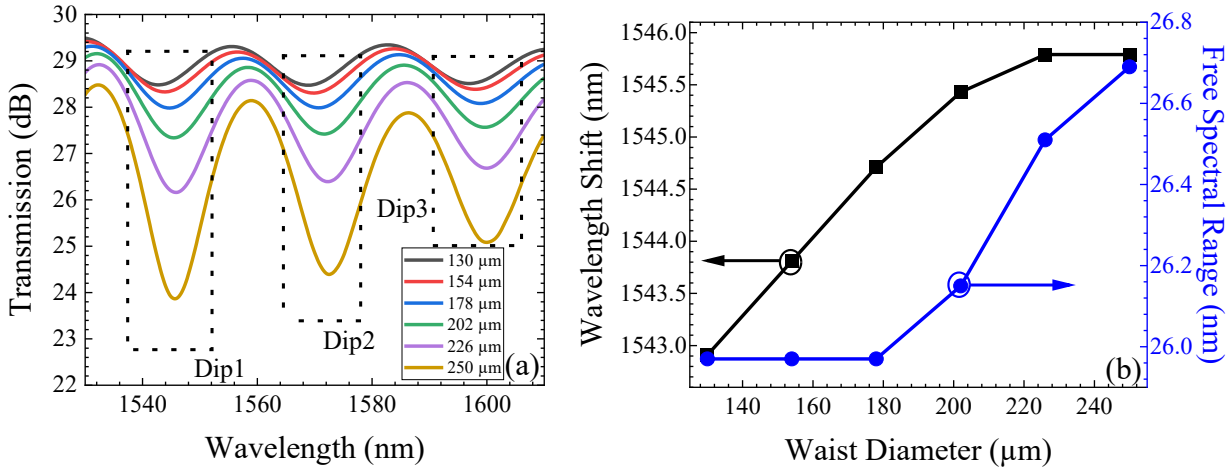

Figure 2-23: Symmetrically bulge-fused FMZIs with different waist diameters spaced at 2.03 cm: (a) Transmission spectra, (b) Wavelength shifts and FSR versus waist diameter for dip m_{61}.

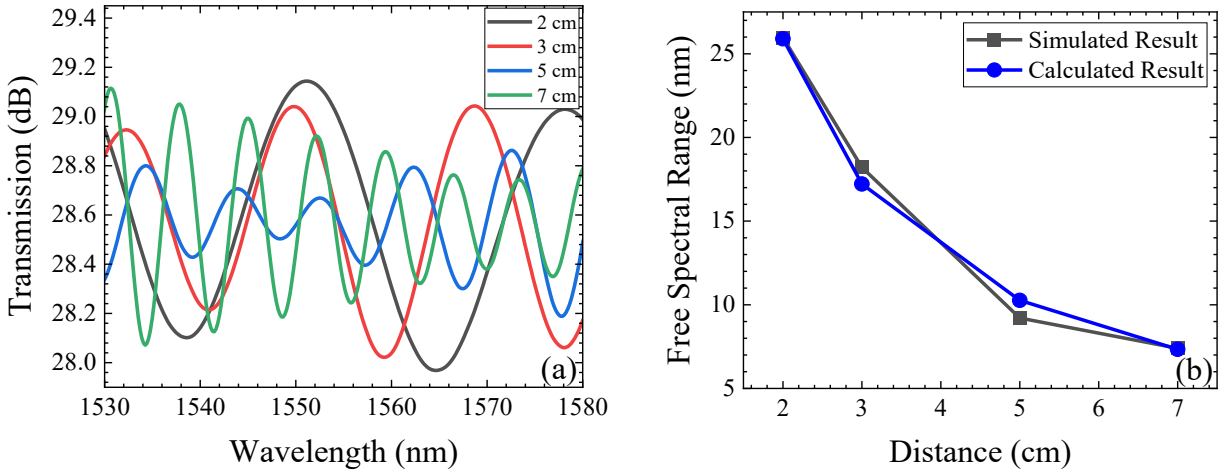

Figure 2-24: Symmetrical bulge-fused FMZI with 180 µm waist diameter and different interval distances: (a) Transmission spectra, (b) Simulated and calculated results.

The transmission spectra at four different taper separations within a wavelength range of 1530 to 1580 nm are shown in Figure 2-24 (a). As the taper separation increases, more dips can be seen within the same wavelength range. In contrast to the tapered structure, the simulation results show that the intensity of transmission spectra does not significantly change with increasing taper separation. The dip near 1540 nm (dip 1) is selected to analyze the FSR of each spectrum. Figure 2-24 (b) shows the wavelength difference between dip 1 and its higher-wavelength neighbouring dip (dip 2) in the simulated spectrum and the calculated free spectral range of dip 1. The interference order *m* and FSR for dip 1 are shown in Table 5.

Table 5: Position of the dip wavelength and the interference order *m* of dip 1.

Taper separation (cm)	Dip 1 (nm)	Dip 2 (nm)	Simulated FSR (dip2-dip1)	Dip 1 Order *m*	Calculated FSR
2	1538.58	1564.55	25.97	60	25.90
3	1540.92	1559.13	18.21	90	17.22
5	1539.11	1548.32	9.21	150	10.26
7	1541.28	1548.68	7.4	211	7.34

Compared with tapered fibers, bulge-fused fibers offer excellent mechanical properties. After preparing the first coupler using the method described in Section 2.3, the fiber cleaver is cut at 2.0 ± 0.1 cm from the first coupler, and a second bulge-fused junction is fabricated similarly.

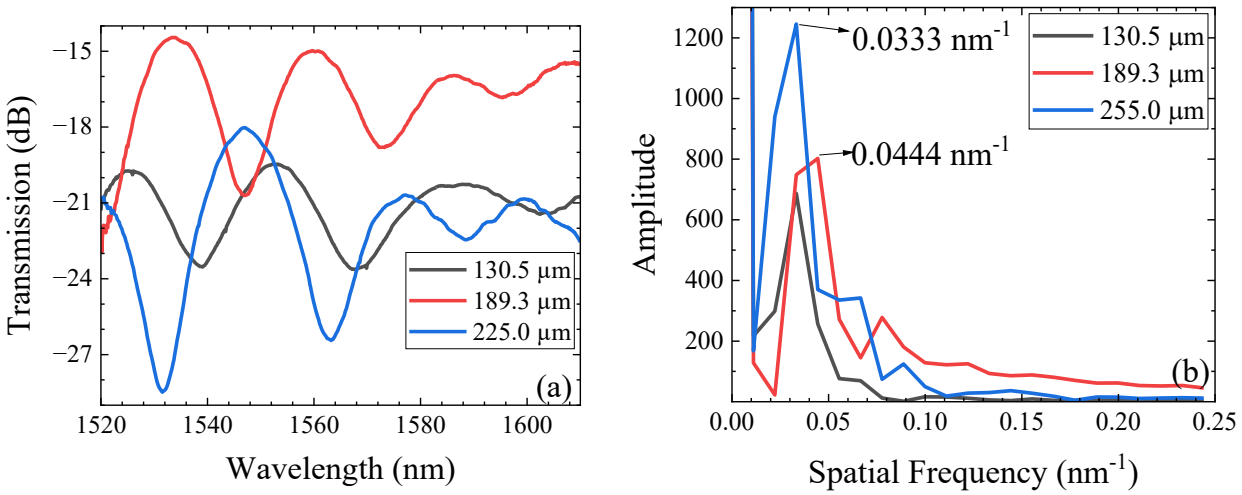

Figure 2-25: Symmetrical bulge-fused FMZIs with different waist diameters with taper separation of 2.0 ± 0.1 cm. (a) Transmission spectra. (b) FFT of those FMZIs transmission spectra.

Figure 2-25 (a) shows that the dips become sharper with increasing diameter, shown in the FFT by the positive correlation between the amplitude of the dominated peak and the diameter. As shown in Figure 2-25 (b), the transmission spectra of the bulge-fused FMZIs have a dominant peak, but compared to the FFT graph of the tapered FMZI, the relative amplitude of minor peaks is higher than the bulge-fused FMZI. The bulge-fused can pass more high-order cladding modes through the interferometer through a larger diameter. However, compared with the tapered structure, the bulge-fused structure has less capability to recouple the high-order cladding modes back to the core mode.

2.5 Preparation of Graphene Oxide Based Coatings

Combined with the discussion in Section 1.3, GO is inherently electronegative, so, its electrostatic repulsion makes it difficult to coat it on optical fiber with a certain thickness. In the present study, GO and two GO-based materials are coated on FMZIs by combining immersed and in-situ layer self-assembly methods.

2.5.1 Material

Anhydrous ethanol, acetone, and distilled water are available in the university chemical store. Sodium hydroxide (NaOH) with 40 mg/ml has been purchased from Thermo Scientific Chemicals Inc. 4 mg/ml dispersion of graphene oxide in aqueous solution, (3-aminopropyl) triethoxysilane (APTES), and alginic acid sodium salt (Algin) from brown algae with medium viscosity have been purchased from Sigma-Aldrich Corp. Calcium chloride ($CaCl_2$) and Fullerenol ($C_{60}(OH)_n$) have been purchased from ACP Chemicals Inc. and Solaris Chem Inc., respectively, where n is in the range of 30 to 50.

2.5.2 In-Situ Layer Self-Assembly Method

In this study, there are three types of coating materials: graphene oxide (GO) [56, 69, 50], graphene oxide and alginic acid sodium (GO/Algin) [70, 71], and the GO and fullerenol nano-composite encapsulated by the hydrogel ($GO/C_{60}(OH)_n$: Hydrogel) [72, 73, 74]. GO is an

important graphene derivative material, which is a nanomaterial with unique physical and chemical properties for many new applications. GO/Algin coating is a nanocomposite material with a 3D network structure and good hydrophilic and water swelling properties. Since the GO/C_{60} nanocomposite is water-soluble, the hydrogel is encapsulated on top of the coating in order to prevent damage to the coating material during the experiment.

After fabricating tapered and bulge-fused FMZIs using the method mentioned in Section 2.1 and 2.3, the prepared FMZIs are soaked in acetone for 30 min to clean the surface from contaminants. Afterwards, the interferometer is washed and dried with distilled water and absolute ethanol. Secondly, the interferometer is immersed in 1.0 M NaOH aqueous solution for two hours for alkali treatment to attach hydroxy groups onto the surface of the fiber. Then, it is removed and rinsed thoroughly with distilled water and absolute ethanol to remove the hydroxy groups. The next step is to silanize the optical fiber by immersing the interferometer in 5% APTES for 4 hours. The 5 wt% APTES solution is prepared by using ethanol as a solvent. During this process, the hydroxyl groups on the silica surface react with APTES to form Si-O-Si bonds. Finally, the interferometer is cleaned with ethanol, air-dried and heated for 10 minutes at 95°C. After the silanization treatment, positively charged NH_2 is formed on the fiber surface, allowing the negatively charged GO nanosheets to be electrostatically adsorbed, as shown in Figure 2-26.

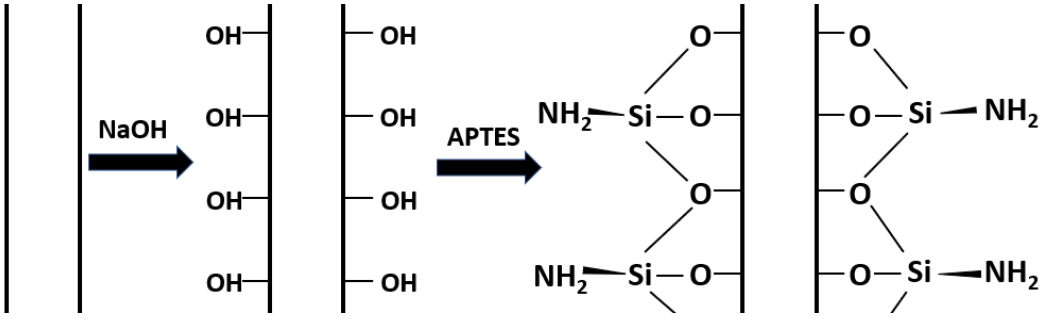

Figure 2-26: Schematic representation of in-situ layer self-assembly method.

Following the processing of the FMZIs with the in-situ layer self-assembly method, the interferometers are immersed in a solution with coating material to form the coating. The 0.8 mg/ml GO solution is used to fabricate a GO coating of 6.85 μm in thickness. This solution is prepared by adding 4.0 ml of distilled water to 1.0 ml of 4.0 mg/ml of GO solution and stirring for two hours at room temperature. The weight ratio of GO to Algin in the GO/Algin coating solution is 2:1. The GO/Algin solution is prepared by mixing 2.0 mg of Algin powder in 4.0 ml of distilled water evenly and refrigerating for twelve hours, then adding 1.0 ml of 4.0 mg/ml GO and stirring for two hours. The GO/$C_{60}(OH)_n$ nano complex solution has a weight ratio of GO to $C_{60}(OH)_n$ of 3:1 [74]. 1.0 ml of GO and 1.3 mg of $C_{60}(OH)_n$ are mixed with 4.0 ml of distilled water and stirred evenly. Then the solution is ultrasonicated for 1.5 hours to obtain a stable aqueous dispersion.

As part of the coating process, the FMZI is elevated by a U-shaped platform (Figure 2-27), and 0.002 ml solution of the coating material is dropped onto the triangular-shaped parafilm using a Syringe Pump (Fusion 400). Due to the hydrophobic properties of parafilm, the droplets can be placed on the interferometer. Then an optical microscope is used to observe droplet position to ensure that the droplets have been uniformly wrapped around the interferometer. Finally, the FMZI is left to dry in the air for 12 hours to ensure complete evaporation of water from the coating layer.

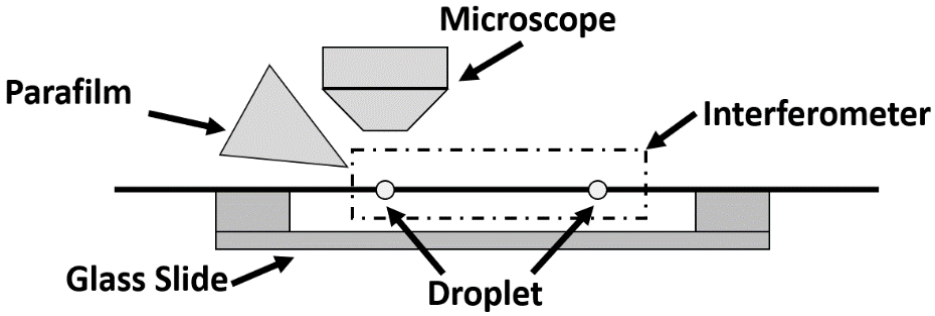

Figure 2-27: Schematic diagram of placing the droplets of coating material on interferometers.

Figure 2-28 shows the images of the coating observed with the optical microscope. Figures 2-28 (a) and (d) show the images observed by the microscope after placing the GO droplet on both fiber interferometers. In the figure, a white spot indicates the light reflection from the droplet surface due to the lensing effect of the curved surface, which can be used to ensure that the center of the interferometer is located at the center of the droplet, allowing the solution to be deposited properly. After the solution is dried, the coating surface is rinsed with distilled water to remove the excess material. Figures 2-28 (b) and (e) show the coating surface after it has dried again and that the coating layer only exists on the interferometer.

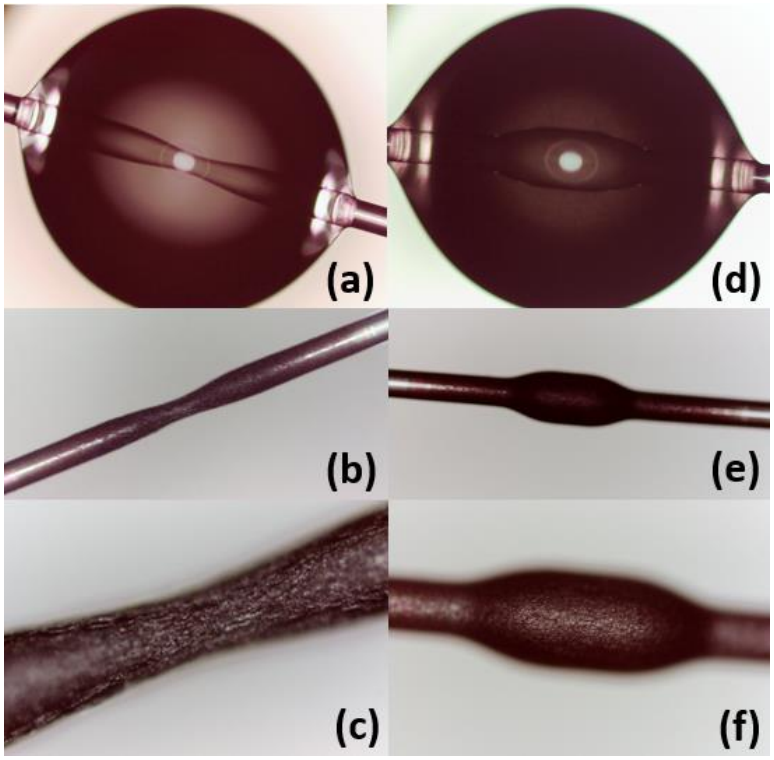

Figure 2-28: Morphology of the coatings on the interferometer observed by the optical microscope. (a), (d) GO droplet on the interferometer (tapered and bulge-fused fiber), (b), (e) GO-coated tapered fiber, and bulge-fused fiber, (c) and (f) surface of the coating.

It can be observed from the figure that the colour of the coating is darker as it gets closer to the center, which is caused by the spherical structure of the droplets and the larger thickness of

the coating at the center of the interferometer. The coating surface is not smooth but has many small puckers, as shown in the partial enlargements of the coating in Figures 2-28 (c) and (f).

The drawback of this method is that the spherical structure of the droplets does not allow the formation of a uniform or well-defined boundary coating in a given area, nor does it allow the application on large areas.

Chapter 3 Refractive Index Sensitivity of Tapered and Bulge-Fused Fiber Mach-Zehnder Interferometers

Interferometric fiber-optic sensors have been extensively studied for measuring variations in physical conditions due to their advantages. Since refractive index (RI) is a fundamental parameter of the optical property of the material. RI sensors can be used to measure the concentrations of gases, and liquids, and are widely used in many applications, including chemical and biological analysis [75], medical diagnosis [76], and food safety control [77, 78]. Optical fiber surface plasmon resonance, fiber Bragg gratings, long-period fiber gratings, and interferometric fiber optic sensors have all been studied as fiber-optic RI sensors [79].

This chapter discusses RI sensing by FMZIs with different types of coating. The sensitivities of RI without and with GO-coated tapered FMZIs with different coating thicknesses are presented in Section 3.3. In Section 3.4, the tapered FMZI coated with GO/Algin is used to measure the RI sensitivity. The RI sensitivity of GO/$C_{60}(OH)_n$: Hydrogel-coated tapered FMZI is discussed in Section 3.5, followed by the discussion on the RI sensitivity of bulge-fused FMZI without and with GO coating in Section 3.6.

3.1 Sensing Mechanisms and Experimental Details

Eqn. (1-7) mentioned in Section 1.2.2 shows the wavelength for attenuation dip is:

$$\lambda_m = \frac{2(n_{\text{core}} - n_{\text{clad}})L}{2m+1} \tag{3-1}$$

When the ambient RI around the interferometer changes leading to a change in the effective RI of the cladding mode, while the effective RI of the core mode does not change, so n_{core} - n_{clad} changes to n_{core} - (n_{clad} + δn_{clad}) leading to a shift of dip wavelength (λ'_m) of the interferometric inclination, which can be expressed as: [79]

$$\lambda'_m = \frac{2(\Delta n_{\text{eff}} + \delta\Delta n_{\text{eff}})L}{2m+1} \tag{3-2}$$

where δn_{eff} is the change of the effective RI of the cladding mode caused by the variation of external RI.

The wavelength shift of the interference dip can be used to measure the RI of the environment. The RI sensitivity (S) of the sensor can be expressed as:

$$S = \frac{\lambda'_m - \lambda_m}{\Delta n} = \frac{2\delta\Delta n_{\text{eff}}L}{2m+1} \tag{3-3}$$

The RI sensing experiments are conducted with the FMZI configuration consisting of a glass slide with a parafilm mounted on the surface, as depicted in Figure 3-1. The FMZI sensor is sensitive to external perturbations such as bending and strain. During the experiment, the FMZIs (without and with coating) are fixed between two translation stages to minimize the impact of perturbations on RI measurement. The translation stages apply a small tension or strain to FMZI to avoid bending. Tuning the concentrations of potassium chloride (KCl) solution will alter the RI at a room temperature of 20.0°C. The KCl powder (≥99.0 wt%) is purchased from ACP

Chemicals Inc. Due to the hydrophobic nature of the parafilm, the drops of the hydrophilic solution on parafilm achieves large contact angles so that the FMZI could be covered completely in the solution. The parafilm is moved to ≈1 mm below the FMZI during the measurement. Subsequently, 2.0 ± 0.1 ml of the aqueous solution is dropped onto the film, and the height of the droplet is adjusted using a vertical axis stage to ensure that the FMZI is immersed in the solution. All experiments are performed in this chapter at a room temperature of 20°C. KCl of specific weight is dissolved in distilled water to prepare potassium ion fluid of preferred concentration. Potassium ion droplets of different concentrations vary from 0 to 24 wt% (with a corresponding RI range from 1.333 to 1.367 RIU). With this configuration, the spectra of the FMZI at different RI are measured using an Er^{3+} broadband source (EBS-7201) and an optical spectrum analyzer (OSA). Before the measurement, the FMZI is rinsed with distilled water three times to remove the dust on the surface and dried for 15 min in the ambient environment. Then the fiber is immersed in KCl solutions of different concentrations for 10 min to conduct the sensing experiments. After each measurement, the interferometer is washed with distilled water and desiccated in the air for 15 min.

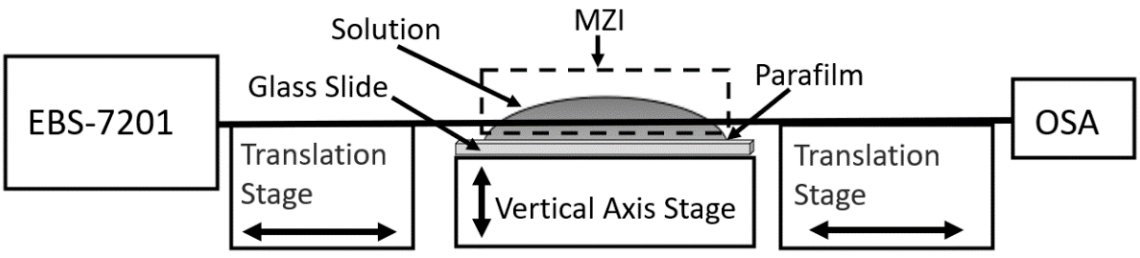

Figure 3-1: Schematic diagram of the experimental setup for RI measurement.

3.2 Simulation of Tapered Fiber Mach-Zehnder Interferometers

The transmission spectra of tapered FMZI without coating simulated by COMSOL Multiphysics with the "Electromagnetic Wave, Beam Envelopes" module is shown in Figure 3-2 (a), and the enlarged figures of dips m_{61} and m_{60} shown in Figures (c) and (d).

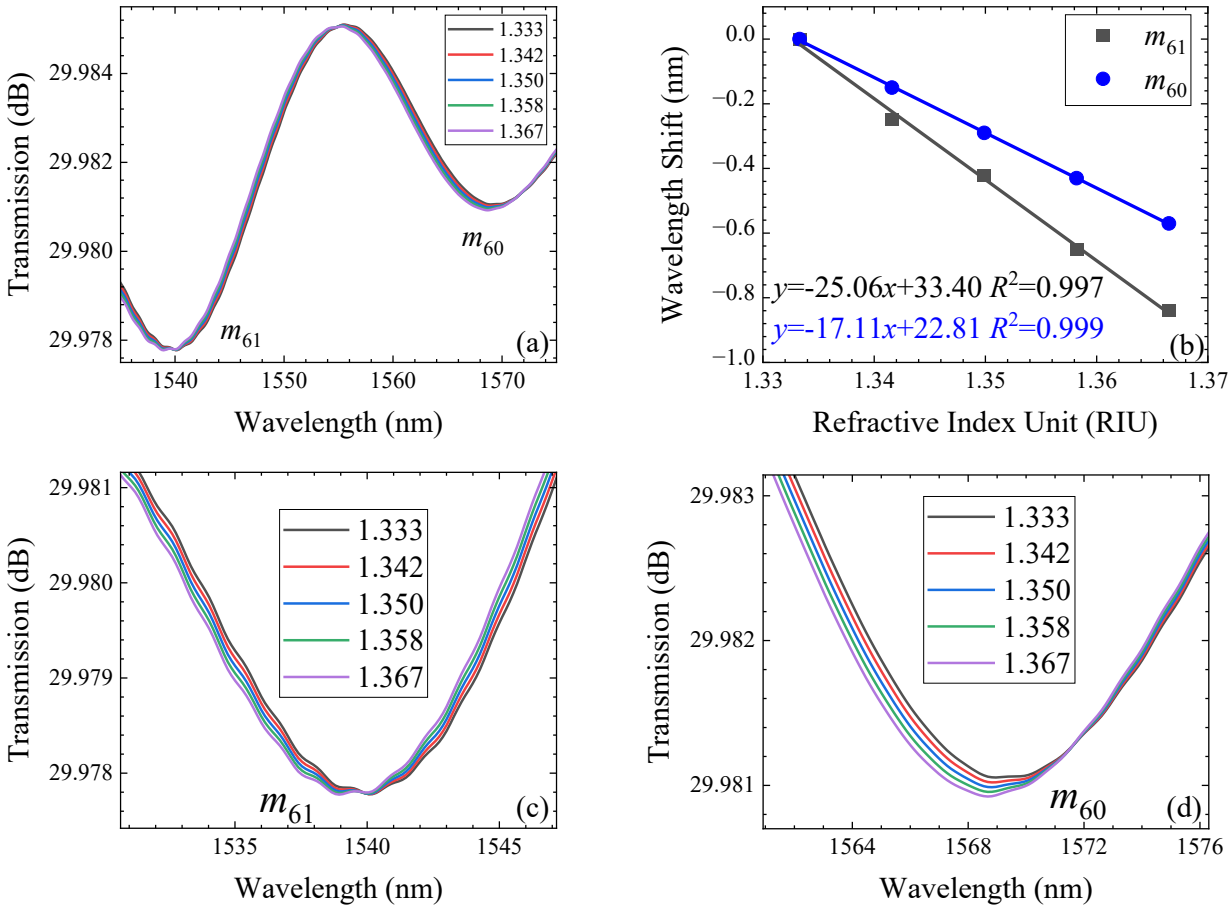

Figure 3-2: Simulated transmission spectra and dip shifts of tapered FMZI without coating. (a) Simulated transmission spectra, (b) wavelength shifts of dips m_{61} and m_{60}, (c) and (d) enlarged dip m_{61} and m_{60} in the transmission spectra.

In this simulation, the length of the tapered structure with a diameter of 75.0 µm is 576.7 µm, and the taper separation is 2.03 cm. The refractive index of the surrounding environment is

set to five values from 1.333 to 1.367 RIU. The dip m_{61} of the FMZI configuration for the simulated uncoated FMZI exhibits a sensitivity of -25.06 nm/RIU for the surrounding RI. The dip m_{60} exhibits a sensitivity of -17.11 nm/RIU, as shown in Figure 3-2 (b). As the surrounding RI increases, a blue-shift is observed in the transmission spectra of dips m_{61} and m_{60}, consistent with Eqn. (3-2) that the increasing surrounding RI decreases the effective refractive index between the core and cladding.

3.3 Refractive Index Sensitivity of Graphene Oxide Coated Optical Fiber Mach-Zehnder Interferometers

GO solutions of 0.5, 0.8, and 1.0 mg/ml are applied to different FMZIs to achieve coating thicknesses of 3.15, 6.85, and 9.45 μm, respectively. Figures 3-3 (a) to (d) show the transmission spectra of uncoated FMZI and GO-coated FMZIs with different coating thicknesses in KCl solution at an interference order of 61. The dip wavelength at n = 1.333 (water) for each interferometer is shown in the figure. The transmission spectrum shifts to a shorter wavelength (blue-shift) with increasing concentration of KCl solution on the interferometer regions of the FMZI configuration.

Figure 3-4 shows the results of linear fitting on RI sensitivities of different thicknesses of GO-coated FMZIs at the m_{61} interference dip. The RI sensitivity is defined as the extent of dip shift in the spectra versus when the surrounding RI changes, which can be read from the slopes of fitted lines. According to this study, the dip shifts of the uncoated tapered FMZI of dip m_{61} exhibit an RI sensitivity of -15.28 nm/RIU for the KCl solution. The coated tapered FMZIs show

sensitivities of -7.42, -17.72, and -9.48 nm/RIU at the GO thickness of 3.15, 6.85 and 9.45 µm, respectively.

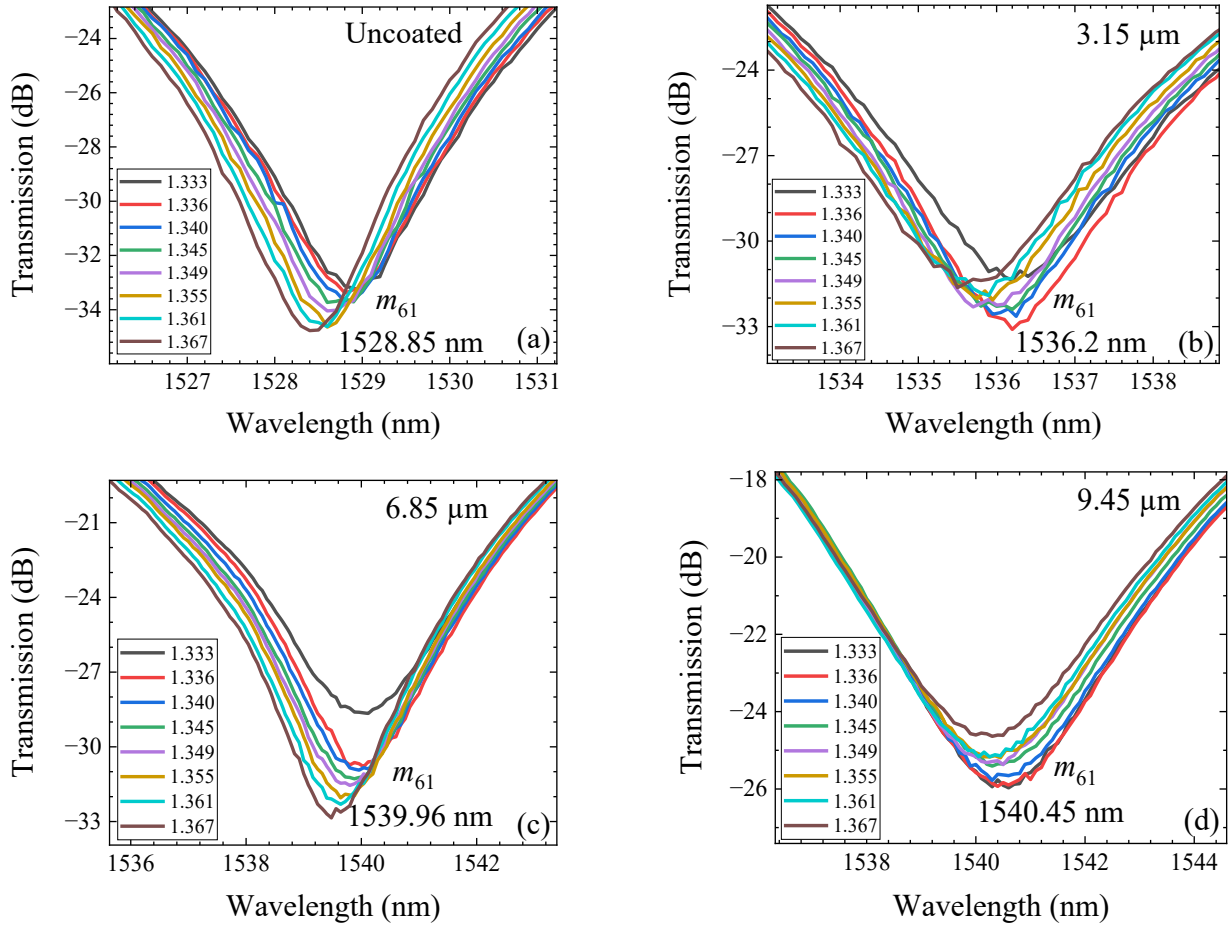

Figure 3-3: Transmission spectra of the interferometer with and without GO coating at interference order 61. (a) Uncoated FMZI. (b) - (d) Corresponds to FMZIs coated with GO layers of thickness 3.15, 6.85, and 9.45 µm, respectively.

Figure 3-4 shows that the RI sensitivity increases with the GO coating thickness when the coating thickness is smaller than 6.85 µm, but when the coating thickness is equal to 9.45 µm, the RI sensitivity of coated FMZI is lower than the uncoated one. As the thickness of the GO coating increases beyond a specific value, the influence of the external RI on the electromagnetic wave propagating in the taper regions diminishes gradually because the propagating wave does not penetrate the coated region of large thickness due to skin depth limitation. Another reason for

the effect of GO thickness is that when the coating thickness is too large, the inner layer of the GO coating remains almost unchanged due to the limited permeability of the absorbed water molecules. The large thickness of the coating isolates the RI sensor to reduce the sensitivity of the measurement.

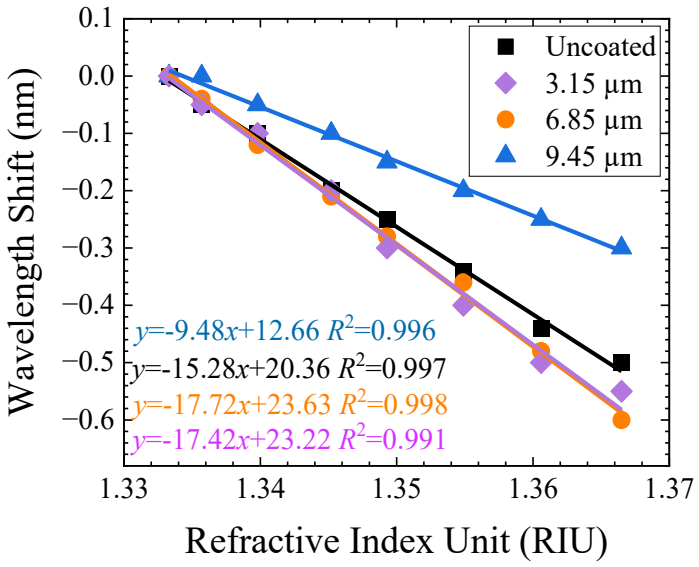

Figure 3-4: Wavelength shifts of dips in the transmission spectra of uncoated and GO-coated tapered FMZIs at interference order 61 when the interferometer is immersed in KCl solutions of different refractive indices.

Figure 3-5 (a) to (d) show the transmission spectra of uncoated FMZI and GO-coated FMZIs with different coating thicknesses in the KCl solution at interference order 60. Similarly, with increasing concentrations of the KCl solution dropped on the FMZI (without and with coating), the transmission spectra shift to a shorter wavelength.

Figure 3-6 shows the results of linear fitting on RI sensitivities at interference dip m_{60}. By calculating the slopes of the fitted lines, the uncoated FMZI shows an RI sensitivity of -10.23 nm/RIU. The RI sensitivities of GO-coated FMZIs are determined to be -17.83, -32.37, and -9.15 nm/RIU for the coating thickness of 3.15, 6.85, and 9.45 µm, respectively.

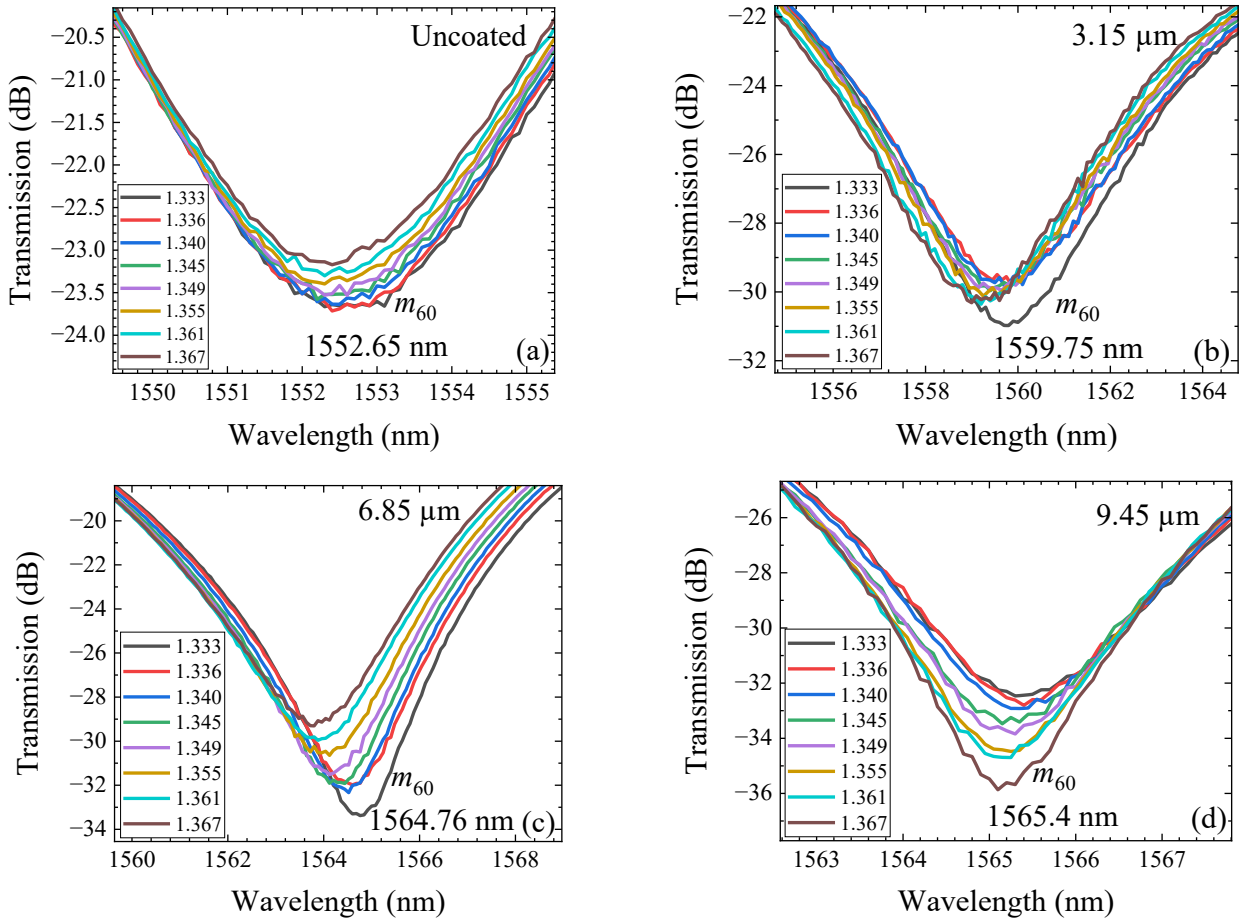

Figure 3-5: Transmission spectra of FMZIs with and without coating at interference order 60. (a) Uncoated FMZI. (b) - (d) Corresponds to FMZIs coated with GO layers of thickness 3.15, 6.85, and 9.45 µm, respectively.

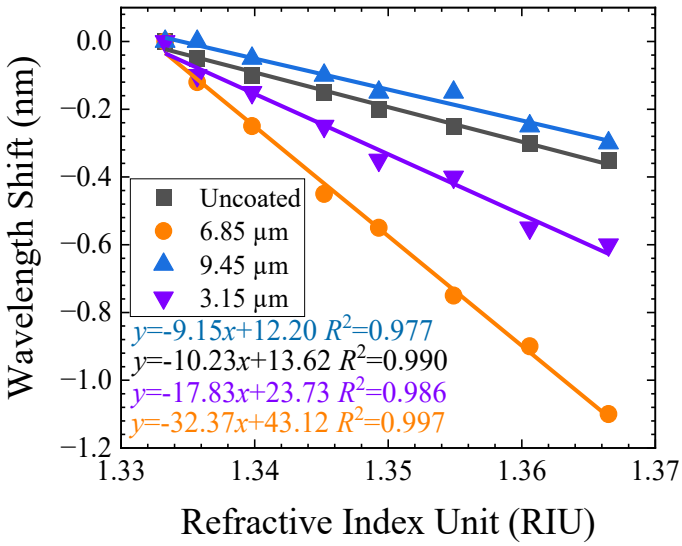

Figure 3-6: Wavelength shifts of dips in the transmission spectra of uncoated and coated FMZIs at interference order 60 when the interferometer is immersed in KCl solutions of different refractive indices.

On the other hand, different dips exhibit different magnitudes in wavelength shift by comparing the results shown in Figures 3-4 and 3-6, which is ascribed to the fact that multiple cladding modes have been excited and have interfered with the core mode. Different cladding modes have various RI dependencies on ambient RI at a specific wavelength [80]. The slope of m_{60} indicates that the RI sensitivity is in direct proportion to the coating thickness when the thickness of GO is between 0 to 6.85 μm. However, when the thickness is increased to 9.45 μm, the sensitivity starts to decrease. Compared with the uncoated FMZI, the rate of sensitivity enhanced with different GO thicknesses can be calculated by:

$$\text{Enhanced Percentage} = \frac{S_{\text{Coated}} - S_{\text{Uncoated}}}{S_{\text{Uncoated}}} \times 100\% \tag{3-4}$$

where S_{Coated} is the sensitivity of coated FMZI, S_{Uncoated} is the sensitivity of FMZI without coating.

At the dip m_{61}, the enhanced percentage after being coated with different thicknesses of GO coating is 14%, 16%, -38% at the GO thickness of 3.15, 6.85, and 9.45 μm, respectively. At the dip m_{60}, the enhanced percentage is 74%, 216%, -11%, respectively. According to the rate of sensitivity increase, the GO coating has a more significant improvement of the RI sensitivity at a dip m_{60}.

The optical energy inside the taper region is primarily contained within the LP_{01} and LP_{02} modes due to the cylindrical symmetry and higher overlap integrals under the weakly guided approximation [81]. The FFT method obtains the spatial frequency spectrum to prove the excitation mode in the tapered fiber configuration. Figure 3-7 shows the excitation signature of dominant modes (LP_{01}) at spatial frequency 0.04 nm^{-1} and a minor peak at 0.08 nm^{-1} (LP_{02}). These two spatial frequencies determine the peak shift of transmission spectra because their amplitudes are relatively large.

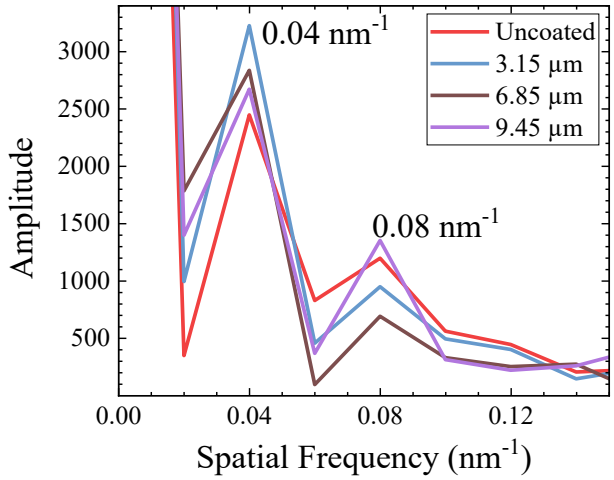

Figure 3-7: FFT on the transmission spectra of the uncoated FMZI and FMZI coated with GO of different thicknesses.

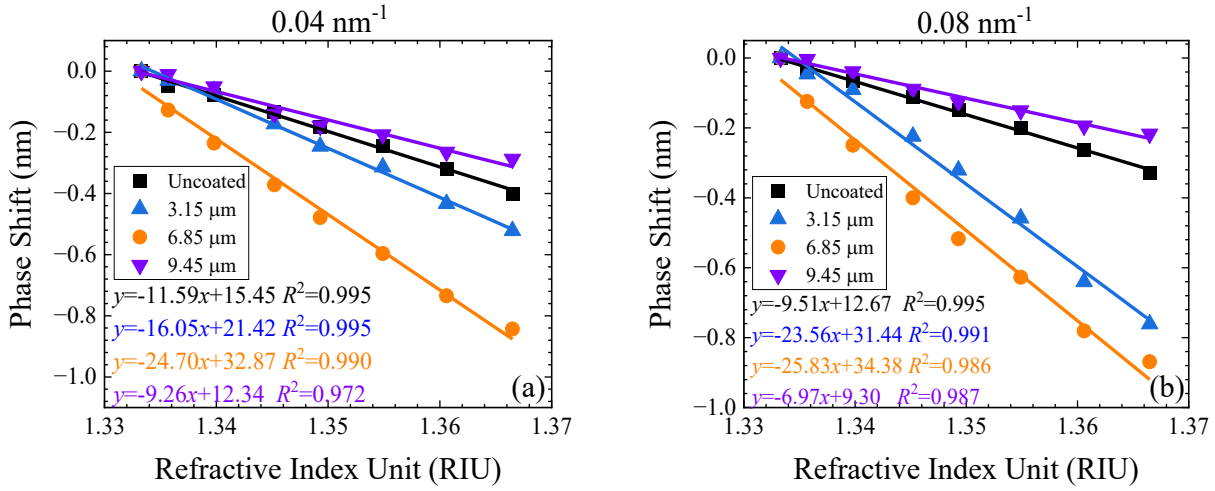

Figure 3-8: Phase shift of bare and coated FMZIs at the spatial frequency of (a) 0.04 nm^{-1}, (b) 0.08 nm^{-1}.

Figures 3-8 (a) and (b) show the phase shift of two spatial frequencies. Compared to the RI sensitivity of the uncoated FMZI in LP_{02} mode (9.51 nm/RIU), it exhibits a higher RI sensitivity in the LP_{01} mode (11.59 nm/RIU). According to Eqn. (3-4), when the GO thicknesses are 3.15, 6.85, and 9.45 μm, the enhanced percentages relative to the LP_{01} mode are 38.47%, 113.05%, and -20.1%, while for the LP_{02} mode, the enhanced percentages are 147.85%, 171.74%, and -26.65%, respectively. Compared with the measurement results of coated FMZI with

different coating thicknesses, the GO coating improves the RI sensitivity when the thickness is from 0 to 6.85 μm. The LP_{02} mode seems more sensitive to the change of surrounding RI after coating with a GO layer. On the other hand, when the thickness is increased to 9.45 μm, the coating layer negatively affects the RI sensitivity in both LP modes. This indicates when the coating thickness increases to a certain level, the water molecules around the coating cannot affect the inner layer of the coating due to the limited permeability.

3.4 Refractive Index Sensitivity of Graphene Oxide/Alginate Coated Fiber Mach-Zehnder Interferometer

The GO/Algin-coated FMZI with a coating thickness of 7.15 μm can be used as a sensor to measure the RI sensitivity. The transmission spectra of GO/Algin-coated FMZI in KCl solutions of different concentrations are shown in Figure 3-9 (a). It shows that dips m_{61} and m_{60} are located at 1537.95 and 1563.00 nm, respectively, when the interferometer is immersed in liquid (water). Those dips are located at 1537.15 and 1563.70 nm after immersing the interferometer in 24 wt% KCl aqueous solution, corresponding to blue-shifts of 0.80 and 0.30 nm, respectively. Figures 3-9 (b) and (c) show the enlarged spectra of dip m_{61} and m_{60} in the transmission spectra.

Figure 3-10 shows the fitting results of the dip shift of GO/Algin-coated FMZI at dip m_{61} and dip m_{60} and the FSR of dip m_{61}. Figure 3-10 (a) shows that the dip m_{61} is linearly blue-shift with the increase of the surrounding RI. Therefore, the RI sensitivity of m_{61} is determined to be -23.91 nm/RIU. Even though the dip m_{60} shifts with the change of surrounding RI, the shift is nonlinear.

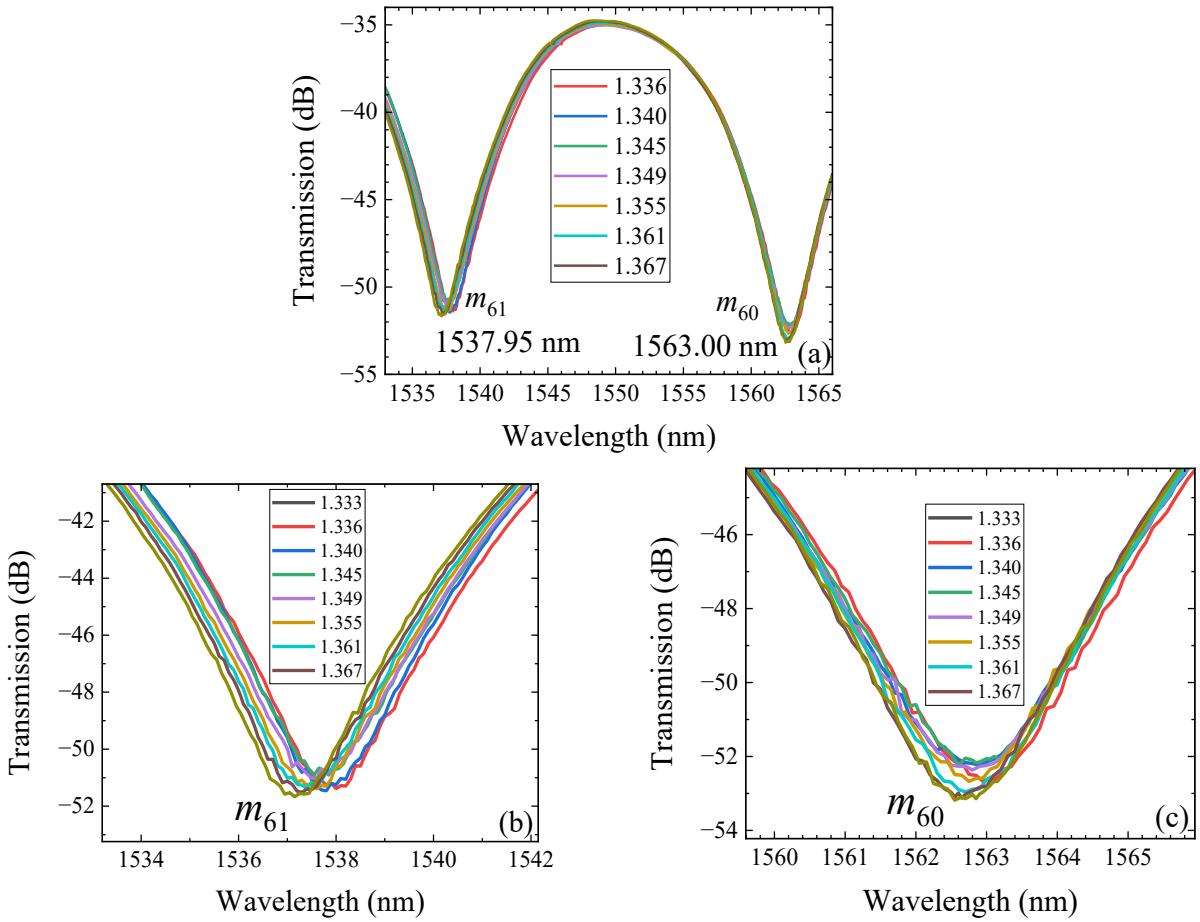

Figure 3-9: Transmission spectra of GO/Algin-coated tapered FMZI. (a) Transmission spectra, enlarged figure of dip (b) m_{61} and (c) m_{60}.

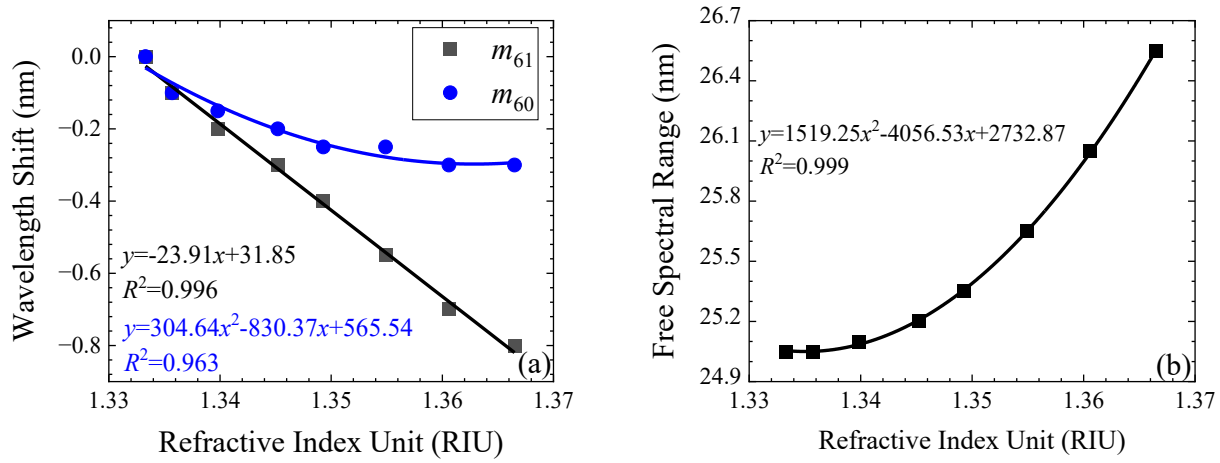

Figure 3-10: RI sensing measurement of the GO/Algin-coated tapered FMZI. (a) Dependence of wavelength shifts on RI for interference orders 61 and 60, (b) FSR of dip m_{61}.

After polynomial fitting, the coefficient of determination for dip m_{60} becomes nonlinear as the surrounding RI increases. Therefore, dip m_{60} cannot be used for measuring RI sensitivity. Due to the different liquid absorption properties of Algin and GO, the nonlinear relationship between dip m_{60} and refractive index is attributed to the non-uniform swelling of the coating in the KCl solution. Another reason for the nonlinearity is the FSR varies simultaneously with the change of the refractive index of surrounding material, thus interfering with the wavelength shift of the dip m_{60}. Eqn. (2-4) shows that the FSR depends on the effective refractive index, where FSR $\propto$ 1 / Δn_{eff}. When the surrounding RI increases, the Δn_{eff} will decrease due to increased cladding RI. FSR is proportional to the external refractive index, as shown in Figure 3-10 (b). After the polynomial fitting,

$$\text{FSR} = 1519.25 \times RI^2 - 4056.53 \times RI + 2732.87,\ R^2 = 0.999.$$

3.5 Refractive Index Sensitivity of Graphene Oxide/Fullerenol: Hydrogel Coated Fiber Mach-Zehnder Interferometer

Fullerenol is a $C_{60}(OH)_n$ derivative with abundant hydroxide bonds attached to its surface, making it highly water soluble. Functional polymeric materials that use water as a dispersion medium are known as hydrogels, which is one of the hygroscopic polymeric materials. Hydrogels are three-dimensional polymer networks capable of reversible volume changes with changes in their Donnan osmotic pressure [82]. In many hydrogel materials, by combining sodium alginate solution and calcium chloride solution, alginate and calcium ions can react sufficiently to form an organically cross-linked polymeric water insoluble material called CaAlg

hydrogel. The hydrophilic residues will bind to water molecules, while the hydrophobic groups will swell, and the three-dimensional network structure of CaAlg hydrogels processes good water absorption properties [83]. For this reason, the hydrogel is attached to the surface of the GO/$C_{60}(OH)_n$ complex coating to prevent the $C_{60}(OH)_n$ from dissolving in water. After coating GO/$C_{60}(OH)_n$ onto the FMZI by self-assembly method and air-dried for 12 hours, the coated tapered fiber is immersed in a 0.5 ± 0.1 wt% sodium alginate solution for 10 seconds and removed. Then, it is immersed in a 1.0 ± 0.1 wt% calcium chloride solution for five minutes to react fully with alginate ions, thus forming a CaAlg hydrogel. Finally, the coating is rinsed with water and then air-dried.

GO/$C_{60}(OH)_n$: Hydrogel-coated FMZI has a coating thickness of 6.91 μm. Figure 3-11 (a) illustrates the transmission spectra at KCl solutions of different concentrations for the coated FMZI. It shows that dips m_{61} and m_{60} are located at 1541.75 and 1567.80 nm, respectively, when the interferometer is immersed in water. As a result of immersion in a 24 wt% KCl aqueous solution, dips are located at 1541.20 and 1568.00 nm. Dip m_{61} corresponds to a blue-shift of 0.55 nm, while the dip m_{60} shifts to a longer wavelength with a red-shift of 0.20 nm. Figure 3-11 (b) and (c) show the enlarged dips m_{61} and m_{60} in the transmission spectra.

Figure 3-12 shows the fitting results of the dip shift of GO/$C_{60}(OH)_n$: Hydrogel-coated FMZI at dips m_{61} and m_{60} and the RI sensitivity of dip m_{61}. Figure 3-12 (a) shows that the dip m_{61} is linearly blue-shifted with the increase of the surrounding RI. Therefore, the RI sensitivity of m_{61} is determined to be -16.40 nm/RIU with $R^2 = 0.999$. The dip m_{60} shows no shift when the RI is lower than 1.340 RIU. Red-shift can be found with the increase of surrounding RI. The RI sensitivity of m_{60} is 6.99 nm/RIU with $R^2 = 0.962$ when the RI is between 1.340 to 1.367 RIU. In

this case, the variation of FSR in response to the surrounding RI is linear, and the change can be obtained by linear fitting as 22.61 nm/RIU with $R^2 = 0.996$, as shown in Figure 3-12 (b).

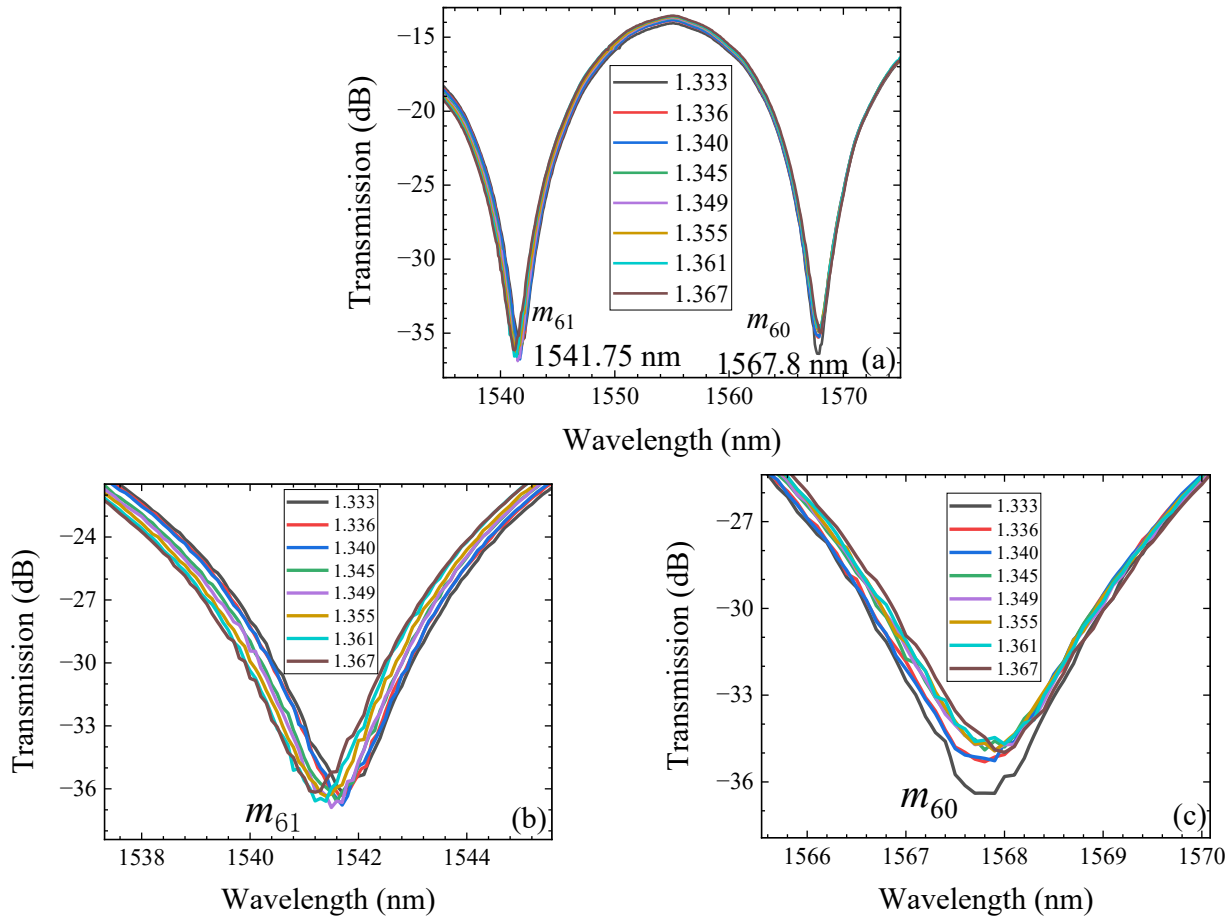

Figure 3-11: Transmission spectra of GO/$C_{60}(OH)_n$: Hydrogel-coated tapered FMZI. (a) Transmission spectra, enlarged figure of dip (b) m_{61} and (c) m_{60}.

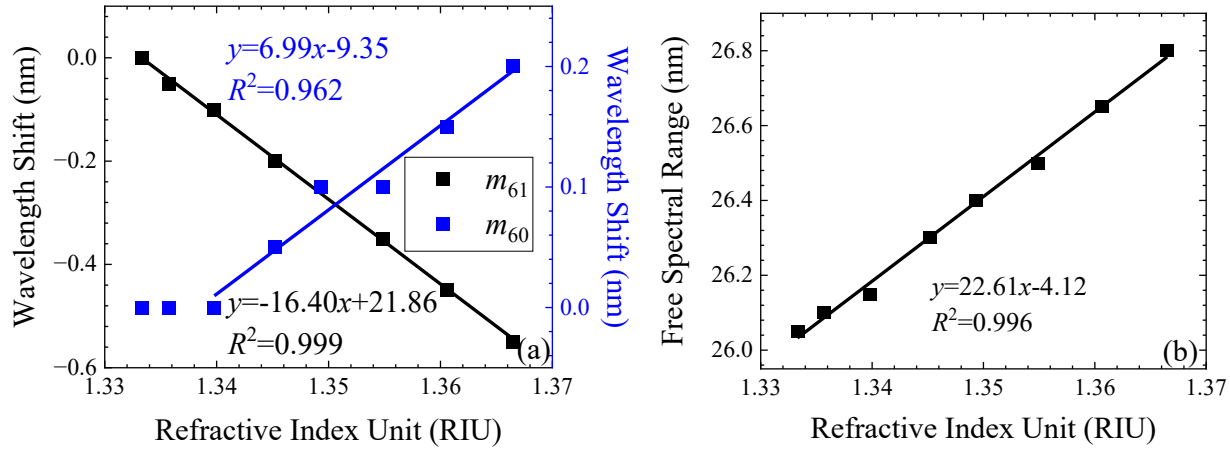

Figure 3-12: RI sensing measurement of the GO/$C_{60}(OH)_n$: Hydrogel-coated tapered FMZI. (a) Dependence of wavelength shifts on RI for interference orders 61 and 60. (b) FSR of dip m_{61}.

According to Eqn. (3-2), when the surrounding RI increases, the RI difference between the core and cladding will decrease, resulting in a blue-shift of the dip. The RI sensitivity of GO/$C_{60}(OH)_n$: Hydrogel-coated tapered FMZI is lower than other types of coating, and the dip m_{60} shows an unusual wavelength shift (red-shift). That is because of the double-layer structure of the coating. The hydrogel coating prevents fullerenol from dissolving in water, but it also serves as a barrier, preventing the internal coating from reacting with the surrounding environment, leading to a decrease in the refractive index sensitivity of the interferometer. In addition, since the whole sensor is immersed in the KCl solution, the change in the surrounding refractive index depends on the taper region and the test arm (cladding) between two tapered structures. The different surrounding RI sensitivity of these two regions leads to a larger change in FSR than the shift of m_{60}, which results in a shift of m_{60} to longer wavelengths. After applying a GO/$C_{60}(OH)_n$: Hydrogel coating, the refractive index sensitivity of dip m_{61} is slightly enhanced, showing an improvement of 7.33%. In contrast, dip m_{60} experiences a significant reduction in sensitivity, decreasing by 31.67% compared to the uncoated FMZI.

3.6 Refractive Index Sensitivity of Graphene Oxide Coated Bulge-Fused Fiber Mach-Zehnder Interferometers

3.6.1 Simulation of Bulge-Fused Fiber Mach-Zehnder Interferometer

Based on the COMSOL Multiphysics simulation, Figure 3-13 (a) shows the transmission spectra of a bulge-fused FMZI without coating. Figure 3-13 (c) and (d) show the enlarged dips m_{60} and

m_{59} in the transmission spectra. This simulation used a bulge-fused structure with a diameter of 180 µm and a taper separation of 2.0 cm. For the simulated FMZI, dip m_{60} exhibits a sensitivity value of -42.41 nm/RIU with $R^2 = 0.988$, while dip m_{59} exhibits a sensitivity value of -64.70 nm/RIU with $R^2 = 0.995$. Dips m_{60} and m_{59} show blue-shifts as the surrounding RI increases, and dip m_{59} shows a higher sensitivity, as shown in Figure 3-13 (b).

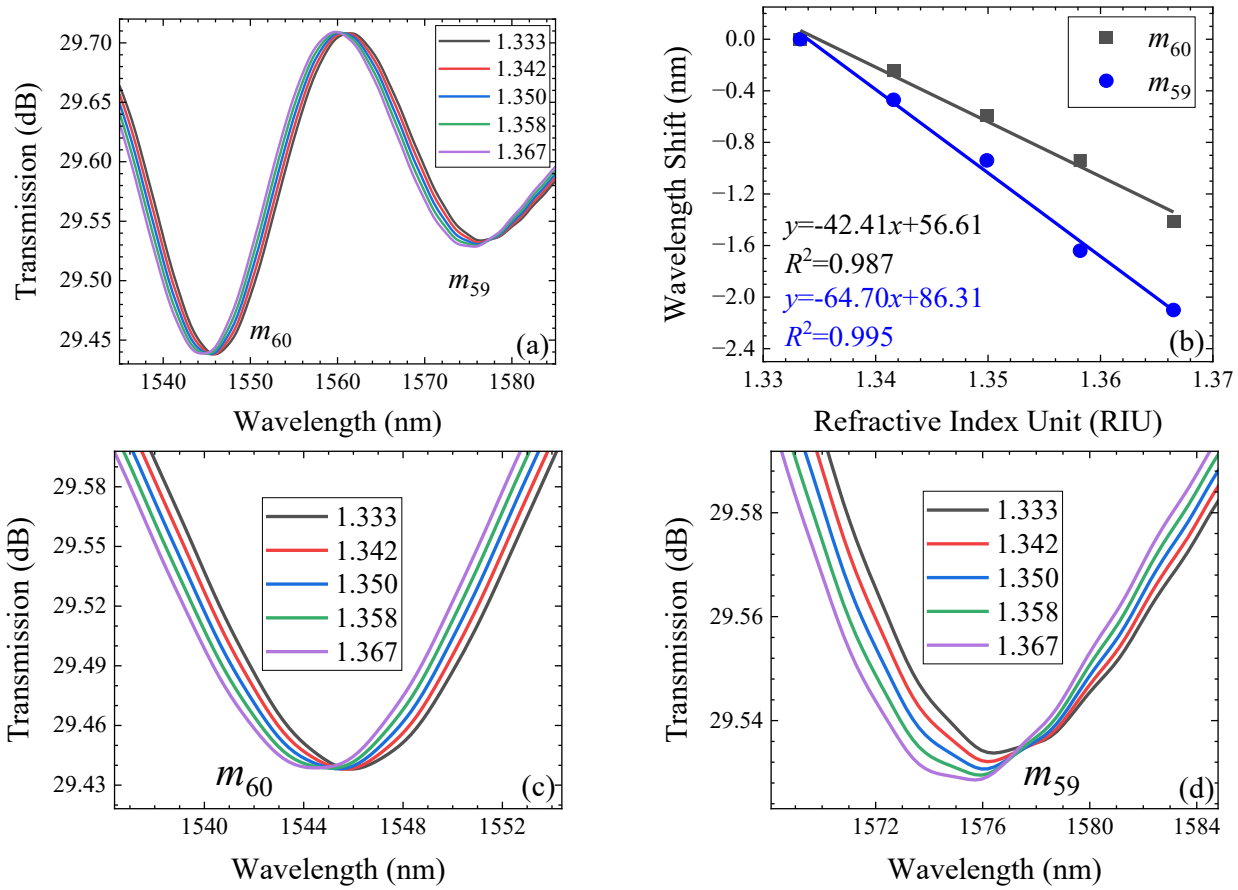

Figure 3-13: Simulated transmission spectra and dip shifts of bulge-fused FMZI without coating. (a) Simulated transmission spectra, (b) dependence of wavelength shifts on RI for interference orders 60 and 59, (c) and (d) enlarged dip m_{60} and m_{59} in the transmission spectra.

3.6.2 Uncoated Bulge-Fused Fiber Mach-Zehnder Interferometer

The uncoated fiber optic sensor is used to measure the refractive index of potassium chloride at different concentrations. It consists of two bulge-fused junctions with an interference length of

2.0 ± 0.1 cm and a diameter of 213 ± 1 µm. As shown in the transmission spectra in Figure 3-14 (a), when the interferometer immerses in water the dips m_{60} and m_{59} are located at 1531.65 and 1561.65 nm, respectively. Those dips are located at 1530.90 and 1560.60 nm when the surrounding RI is 1.367 RIU, corresponding to blue-shifts of 0.75 and 1.05 nm, respectively. Figure 3-14 (c) and (d) show the enlarged dip m_{60} and m_{59} in the transmission spectra.

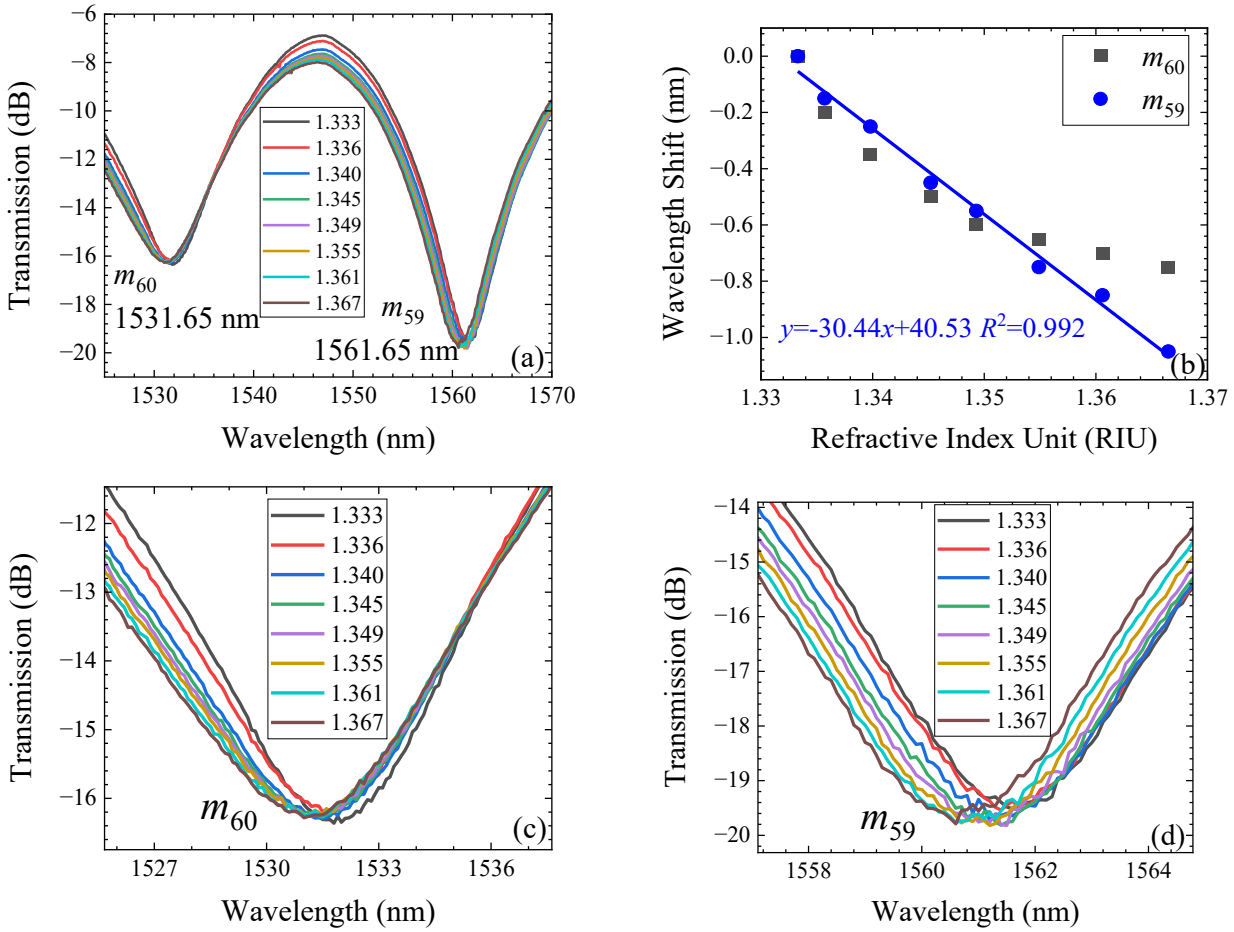

Figure 3-14: Transmission spectra and dip shifts of bulge-fused FMZI without coating when the interferometer is immersed in KCl solutions of different refractive indices. (a) Transmission spectra, (b) dependence of wavelength shifts on RI for interference orders 60 and 59, (c) and (d) enlarged dip m_{60} and m_{59} in the transmission spectra.

Figure 3-14 (b) shows the fitting results of the dip shift of bulge-fused FMZI at dip m_{60} and m_{59}, from which the RI sensitivity of dip m_{59} can be derived from the slope of the linear fit. The figure shown above indicates that the dip m_{59} is a linearly blue-shift with the increase of the

surrounding RI. However, the dip m_{60} shows a nonlinear shift with the change in RI. The dip m_{60} is more sensitive when the RI of the environment is lower than 1.349 RIU with a 0.6 nm wavelength shift. The dip m_{59} is chosen to analyze the RI sensitivity due to its linear property of -30.44 nm/RIU with $R^2 = 0.992$. Also, the overall wavelength shifts of those two dips shows that dip m_{59} has a higher sensitivity, which matches the simulation results.

3.6.3 GO-Coated Bulge-Fused Fiber Mach-Zehnder Interferometer

When a bulge-fused junction of the fiber optic sensor is coated with 0.002 ml of 0.8 mg/ml GO aqueous solution, after the droplet is dried, the thickness of the GO coating is found to be 6.0 ± 0.1 μm. The GO-coated bulge-fused FMZI is used to measure the refractive index of potassium chloride at different concentrations. Figure 3-15 (a) shows that, when the interferometer is immersed in water dips m_{60} and m_{59} are located at 1531.50 and 1561.35 nm, respectively. In the transmission spectra, when the surrounding RI is 1.367 RIU, dips m_{60} and m_{59} are located at 1531.25 and 1560.45 nm, corresponding to blue-shifts of 0.25 and 0.90 nm, respectively. Figures 3-15 (c) and (d) show enlarged spectral curves of dips m_{60} and m_{59}.

Figure 3-15 (b) shows the fitting results of the dip shift of bulge-fused FMZI at dips m_{60} and m_{59}, from which the RI sensitivity of each dip is the slope of the linear fit. Dip m_{59} shows a linear blue-shift with the increase of the surrounding RI and exhibits a sensitivity of -26.44 nm/RIU with $R^2 = 0.995$. However, when the environmental RI is lower than 1.340 RIU, the shift of dip m_{60} remains constant. When the RI is higher than 1.340 RIU, the dip m_{60} exhibits a sensitivity of -9.42 nm/RIU with $R^2 = 0.997$. Equation (3-4) shows that the RI sensitivity of the uncoated bulge-fused FMZI decreased by 13.14% after a GO layer of 6.0 μm in thickness is

coated on the surface in the comparison measurement. The refractive index sensitivity of the bulge-fused FMZI decreases after coating with GO because the strength of the higher-order cladding modes in the bulge-fused structure is weaker, while the large thickness of GO isolates the cladding modes from external influences.

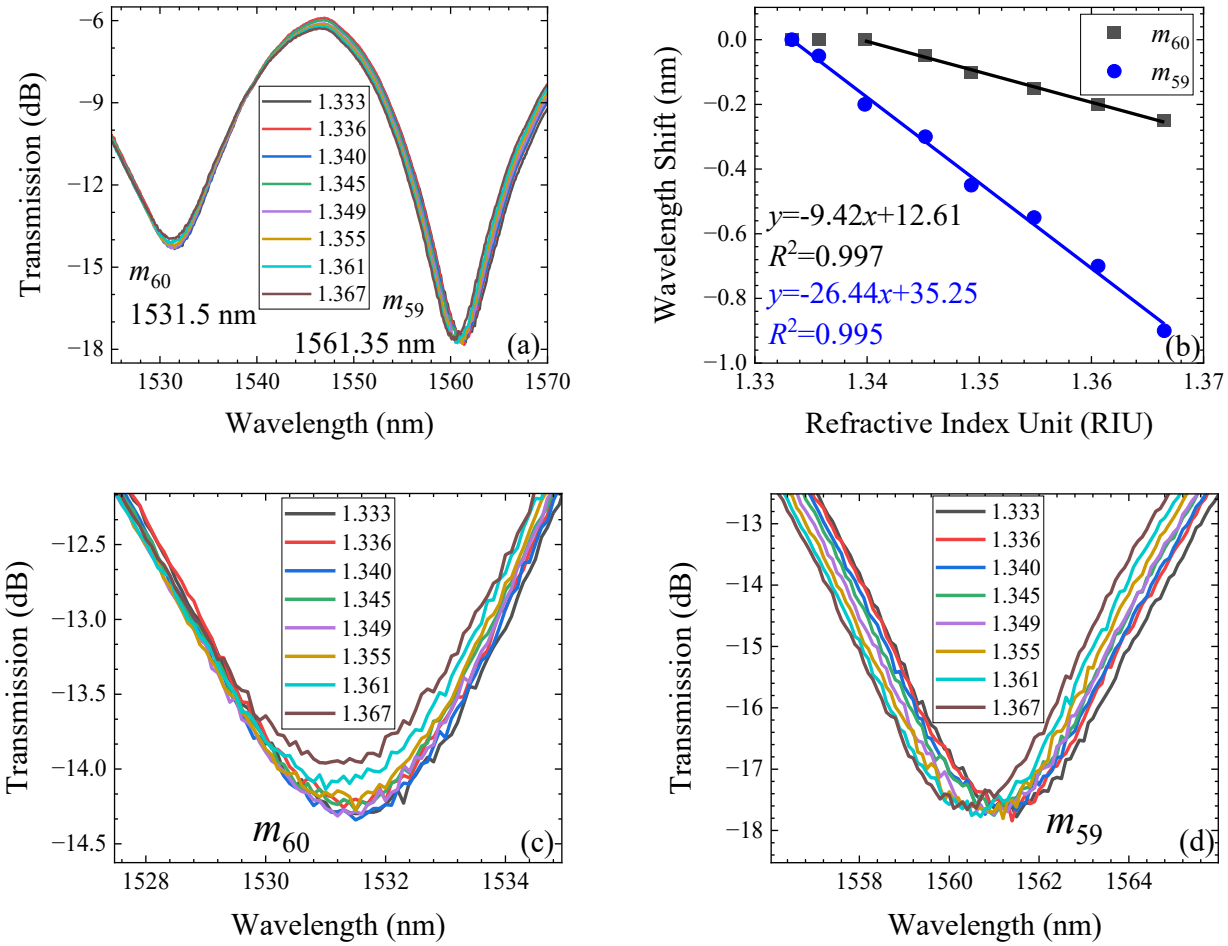

Figure 3-15: Transmission spectra and dip shifts of GO-coated bulge-fused FMZI when the interferometer is immersed in KCl solutions of different refractive indices. (a) Transmission spectra, (b dependence of wavelength shift on RI for interference orders 60 and 59, (c) and (d) enlarged dip m_{60} and m_{59} in the transmission spectra.

Chapter 4 Temperature and Humidity Sensitivities of Tapered and Bulge-Fused Fiber Mach-Zehnder Interferometers

Fiber-optic-based temperature sensors have been proposed for various industrial uses, including many biomedical, geological, automotive, and defence applications [84]. Relative humidity and temperature are equally important environmental conditions in many industrial sectors, such as applications in food, textiles, paper, semiconductors, weather services, etc. [85, 86]

This chapter will investigate temperature and humidity sensing using FMZIs with different types of GO-based coatings. The temperature and humidity sensitivities can be derived from the shift of the dip at different temperatures and humidity levels.

4.1 Sensing Mechanisms and Experimental Details

As shown in Eqn. (1-7), i.e., $\lambda_m = 2L\,(n_{core} - n_{clad}) / (2m + 1)$, the location of the attenuation dip wavelength λ_m depends on the effective refractive index of the core and cladding and the length of the interferometer. When FMZI is placed at different temperatures, the refractive index of the fiber material will change with the temperature. Meanwhile, the size of the fiber itself will change due to thermal expansion. The photothermal effect at different temperatures is also a

factor that affects the dip shift. The temperature sensitivity derived from the shift of the interference dip can be expressed as [87]:

$$\frac{\partial \lambda_{\mathrm{dip}}}{\partial T}=\frac{2L}{2m+1}\frac{\partial \Delta n_{\mathrm{eff}}}{\partial T}+\frac{2\Delta n_{\mathrm{eff}}}{2m+1}\frac{\partial L}{\partial T}=\frac{2}{2m+1}[L\left(\xi_{\mathrm{core}}n_{\mathrm{eff}}^{\mathrm{core}}-\xi_{\mathrm{clad}}n_{\mathrm{eff}}^{\mathrm{clad}}\right)+\Delta n_{\mathrm{eff}}\frac{\partial L}{\partial T}] \tag{4-1}$$

where $\partial L/\partial T = \alpha L$, α is the thermal expansion coefficient. ξ_{core} and ξ_{clad} represent the effective thermo-optic coefficients of the core and cladding, respectively.

When the temperature changes, the thermal expansion and thermo-optic coefficients governors the effective RI changes of the core and cladding modes, respectively. Therefore, the sensitivity of dip wavelength can be expressed as: [88]

$$\frac{\partial \lambda_{\mathrm{dip}}}{\partial T}=\lambda_{\mathrm{dip}}(\alpha+\frac{\xi_{\mathrm{core}}n_{\mathrm{core}}-\xi_{\mathrm{clad}}n_{\mathrm{clad}}}{\Delta n_{\mathrm{eff}}}) \tag{4-2}$$

Relative humidity is a fundamental physical parameter related to RI. The change of water vapour concentration in the air causes a change in the RI around the sensor. The changing RI of the dominant cladding mode is related to the external refractive index as:

$$\Delta n_{\mathrm{clad}}=\frac{\partial n_{\mathrm{clad}}}{\partial RI}\Delta RI \tag{4-3}$$

Therefore, the humidity sensitivity can be approximately represented as: [89]

$$\frac{\partial \lambda_{\mathrm{dip}}}{\partial RH}=\frac{2L}{2m+1}\frac{\partial (n_{\mathrm{core}}-n_{\mathrm{clad}})}{\partial RH} \tag{4-4}$$

The relationship between the transmitted light power P_0 and incident light power P_{i} after passing through the interference region with a length of L is as follows:

$$P_0=P_{\mathrm{i}}\exp(-\gamma L)=P_{\mathrm{i}}\exp(-NTL) \tag{4-5}$$

where γ is the effective evanescent wave absorption coefficient of the cladding at the interference region, $\gamma = NT$, N is the number of reflections per unit length, and T is the transmission coefficient.

Transmission coefficient (T) is expressed with the following equation:

$$T = \frac{\alpha\lambda n_{\text{clad}}\cos\theta}{\pi(n_{\text{core}}^2 - n_{\text{clad}}^2)\sqrt{\sin^2\theta - \frac{n_{\text{clad}}^2}{n_{\text{core}}^2}}} \tag{4-6}$$

where α is the absorption coefficient of cladding, and θ is the angle between incident light and the normal.

Based on the equation above, the transmitted light power P_0 can be calculated as follows [90]:

$$P_0 = P_i \exp\left(-\frac{NL\alpha\lambda n_{\text{clad}}\cos\theta}{\pi(n_{\text{core}}^2 - n_{\text{clad}}^2)\sqrt{\sin^2\theta - \frac{n_{\text{clad}}^2}{n_{\text{core}}^2}}}\right) \tag{4-7}$$

The intensity of the transmission spectrum is determined by both the refractive indices of the cladding and the core. The intensity will change at different temperatures and humidity levels. When the environmental temperature changes, the refractive indices of the core and cladding change due to the thermal expansion and the effective thermo-optical coefficients. In humidity measurements, the sensor measures the difference in refractive indices between the surrounding environment and the core while the RI of the core remains constant. The transmission spectra change with the change in the cladding RI. According to Eqns. (4-2) and (4-4), the temperature and humidity sensitivities can be inferred by detecting the wavelength shift.

The experimental setup for the temperature and humidity measurement is illustrated in Figure 4-1. The experimental setup mainly includes the Er^{3+} broadband source (EBS-7201), an environmental chamber and an OSA. During the experiment, the sensor is fixed on a glass slide to avoid external interference, thus ensuring temperature and humidity stability near the sensing element. The two ends of the sensing element are connected to the EBS-7201 and the OSA,

respectively. The values of the temperature and humidity are derived from the measured dip shift of the transmission spectra by the OSA.

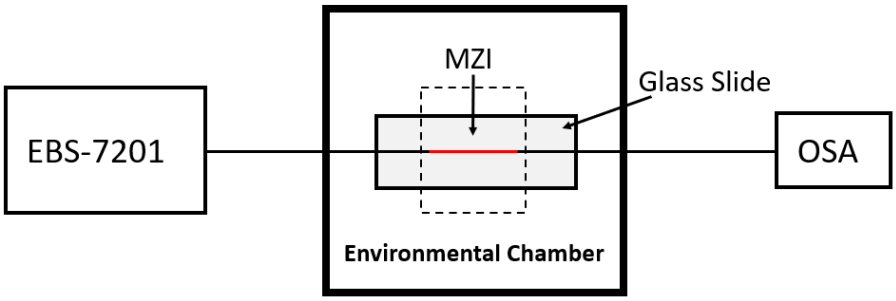

Figure 4-1: Schematic diagram of the experimental setup for measuring temperature and humidity sensitivities.

In the temperature experiment, the relative humidity (RH) is kept at 40 RH%. The temperature range is from 30 to 70℃, and the interval is 5℃. A broader spectral range was selected to investigate the impact of temperature variations on individual dips because the dip wavelengths of the FMZIs used for temperature measurements exhibit significant shifts within the measurement range. This wider spectral range allows for a more comprehensive assessment of the temperature sensitivity of dips m_{61} to m_{59}. The measured wavelength range of transmission spectra is 1520.00 to 1610.00 nm with a resolution of 0.09 nm. After the temperature reaches the set point, the transmission spectrum is recorded and saved by OSA, and the dips can be identified from the spectral curve.

The experimental setup for humidity measurement is the same as the temperature experiment. With the temperature remaining at 40℃, the relative humidity is increased from 20 to 90 RH%. The relative humidity interval is 10 RH%. The decision to confine the spectral range of analysis to dips 61 and 60 is made to enhance the precision and accuracy of the measurement. The transmission spectra are recorded in the wavelength range from 1520.00 to 1570.00 nm with a resolution of 0.05 nm, the highest resolution achievable from the OSA used in this study.

4.2 Uncoated Tapered Fiber Mach-Zehnder Interferometer

The transmission spectra of an uncoated FMZI at different temperatures are shown in Figure 4-2. This FMZI device consists of two tapers with a separation of 2.03 cm. The three dips with interference orders 61, 60, and 59 shift to longer wavelengths with increasing temperature (red-shift). When the temperature is changed from 30 to 70°C, the dip wavelengths of m_{61}, m_{60} and m_{59} shift from 1529.72 to 1531.61 nm by 1.89 nm, 1553.48 to 1555.28 nm by 1.80 nm, and 1574.90 to 1576.61 nm by 1.71 nm, respectively.

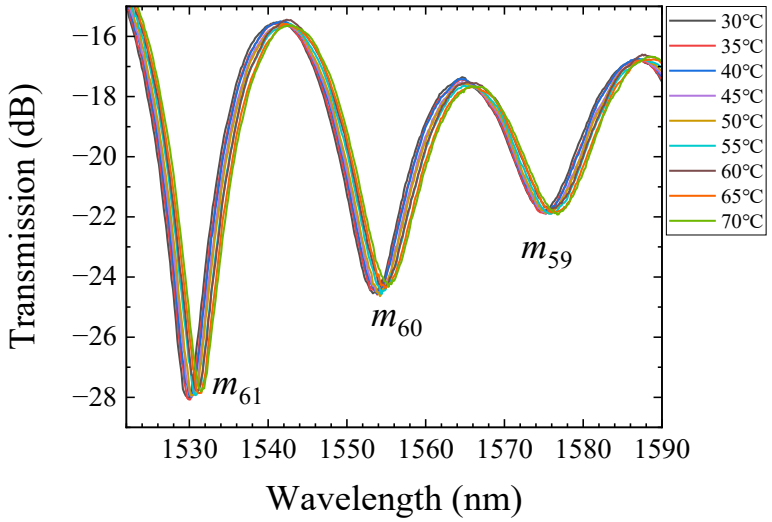

Figure 4-2: Transmission spectra of the FMZI without coating at interference orders of 61, 60, and 59 at different temperatures with relative humidities at 40 RH%.

Figure 4-3 shows that the dips are recorded at each temperature and then analyzed with the linear fitting. Accordingly, temperature sensitivities of individual dips are defined as the shift in the dip wavelength of the FMZI per unit temperature, which is the slopes of the fitted lines. The temperature sensitivities of the selected dips (m_{61}-m_{59}) are 0.0462, 0.0444 and 0.0423 nm/°C

with the corresponding R^2 values of the linear fits as 0.997, 0.997 and 0.993, respectively. The sensitivity of each dip is similar but becomes smaller as the interference order *m* decreases.

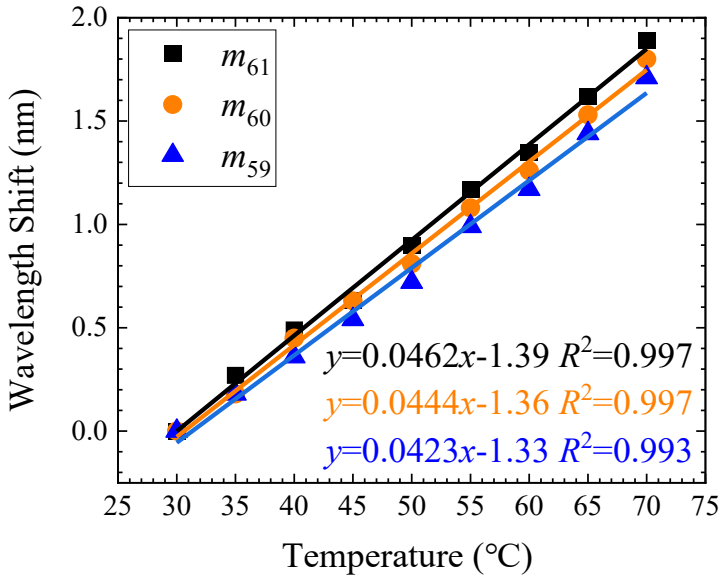

Figure 4-3: Wavelength shifts of dips of the FMZI without coating as a function of increasing temperature.

When the uncoated FMZI is used to measure humidity at 40°C, the dips m_{61} and m_{60} are chosen to analyze the sensitivity. Figure 4-4 (a) shows the dip wavelengths at different humidity levels and the linear fitting result of temperature sensitivities at two interference dips (m_{61} and m_{60}), and Figures 4-4 (c) and (d) show the enlarged spectral curves of each dip. Both dips show a 0.25 nm blue-shift when the humidity is increased from 30 to 90 RH%, as shown in Figure 4-4 (b). With the increase of relative humidity, the shift of both dips is smaller than the OSA resolution, and four relative humidity values are used in the linear fit analysis. As the humidity increases, the water molecules increase the environmental RI, which increases the RI of the cladding, causing a decrease in effective RI, resulting in a blue-shift. This effect is attributed to the phase-matching condition for mode coupling, which depends on the RI of the external surrounding medium at the taper region.

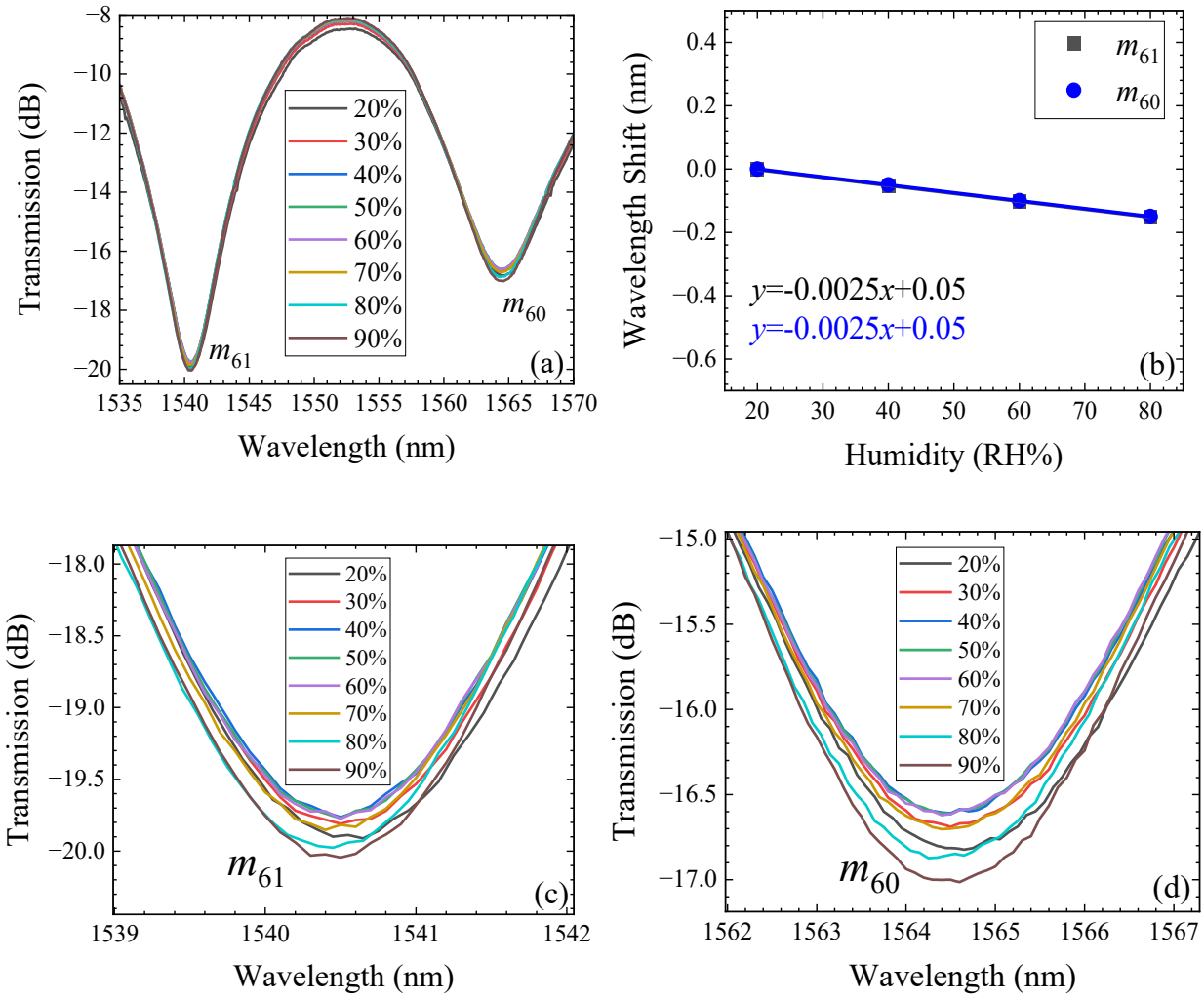

Figure 4-4: Transmission spectra and dip shifts of uncoated tapered FMZI at different relative humidities at 40°C. (a) Transmission spectra, (b) Dependence of wavelength shifts on RH for interference orders 61 and 60, (c) and (d) enlarged dips of m_{60} and m_{59} in the transmission spectra.

4.3 Graphene Oxide Coated Tapered Fiber Mach-Zehnder Interferometer

The GO-coated tapered FMZI with a coating thickness of 6.85 µm is chosen for temperature and humidity sensitivity measurements due to its high RI sensitivity demonstrated in Section 3.3. As the temperature increases, the transmission spectra corresponding to these three dips with interference orders of 61, 60, and 59 exhibit red-shifts, as shown in Figure 4-5. The dip wavelength of m_{61}, m_{60} and m_{59} shift from 1542.14 to 1543.49 nm by 1.35 nm, 1565.54 to 1566.89 nm by 1.35 nm, and 1588.13 to 1590.56 nm by 2.43 nm, respectively.

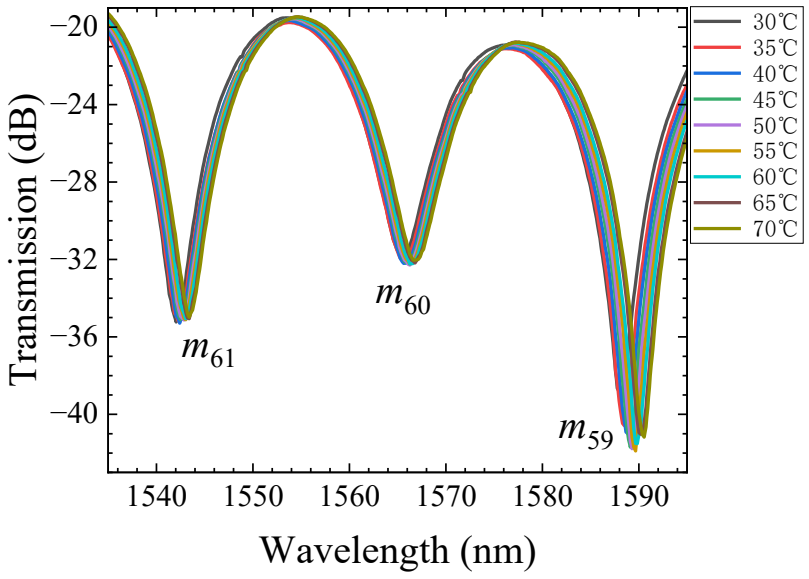

Figure 4-5: Transmission spectra of the GO-coated FMZI at interference order of 61, 60, and 59 at different temperatures and constant 40 RH%.

The shift of those dips at different temperatures are collected and shown in Figure 4-6, which gives the relationship between temperature and dip wavelength shift and the results of linear fitting on the temperature sensitivities of three dips. The temperature sensitivities of dip orders m_{61}, m_{60}, and m_{59} are 0.0345, 0.0356, and 0.0591 nm/°C with the corresponding R^2 values of 0.998, 0.997, and 0.998, respectively. The dip m_{59} has a higher temperature sensitivity, and m_{61} and m_{60} have similar temperature sensitivity.

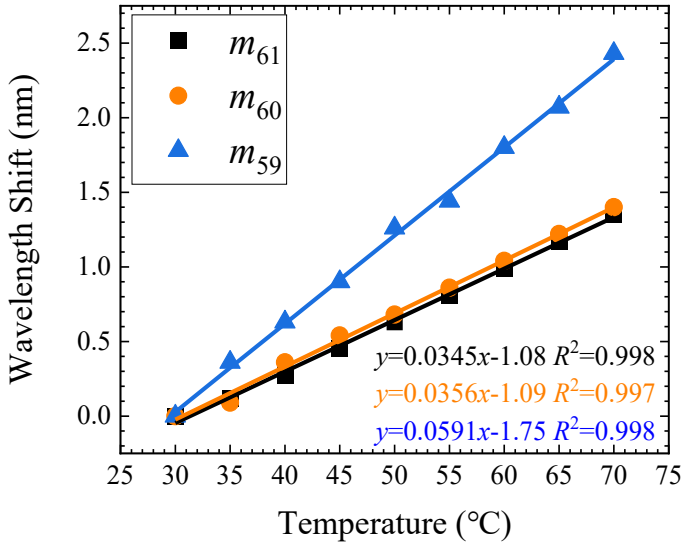

Figure 4-6: Wavelength shifts of dips of the GO-coated FMZI for interference orders of 61, 60, 59 as a function of increasing temperature.

When the GO-coated FMZI is placed in the environmental chamber at a temperature of 40°C, Figure 4-7 shows the transmission spectra of GO-coated FMZI at different humidity levels. As the humidity increases, the dips of two interference orders 61 and 60 exhibit a red-shift in the transmission spectra. Figure 4-7 shows that the uncoated FMZI and the GO-coated FMZI have opposite trends in dip shift during increasing humidity. The change in RI of the GO film coated on the surface of the tapered regions can be attributed to the fact that the GO film absorbs water molecules as the RH increases. Due to the high carrier activity of graphene, polar (water) molecules are easily absorbed by graphene, and the water molecules can be used as electron

acceptors. The absorbed water molecules will adhere to the GO surface or fill the GO layer slices. The surface charge carrier density of GO will increase when the water molecules are attached to the GO. The Fermi level of the GO increases over the Dirac point, which results in the block of interband transition and the decrease in conductivity. The Dirac point is a unique point in energy-momentum space where electron energy is zero. The valence and conduction bands meet at this point, and electrons behave as massless particles. [91] The relationship between the conductivity of GO and the chemical potential is as follows [92]:

$$\sigma = j\frac{e^2 k_B T}{\pi\hbar(w - j2\Gamma)}\left[\frac{\mu_c}{k_B T} + 2\ln\left(e^{-\frac{\mu_c}{k_B T}}\right) + 1\right] + j\frac{e^2}{4\pi\hbar}\ln\left[\frac{2|\mu_c| - (w + j2\Gamma)\hbar}{2|\mu_c| + (w + j2\Gamma)\hbar}\right] \quad (4\text{-}7)$$

where σ is the conductivity, μ_c is the chemical potential, e is the charge of an electron, k_B is Boltzmann's constant, j is the core mode order, T and Γ are the environment temperature, and vibration frequency, $\hbar$ is Planck's constant.

When the RH increase, the wavelength of the resonant dip of GO-coated FMZI will move to a longer wavelength. Hence, the ambient relative humidity can be obtained by measuring the shift in λ_{dip}.

Figure 4-7 shows the central wavelength of dip m_{61} and m_{60} shift from 1540.30 to 1542.50 nm by 2.2 nm and 1563.30 to 1566.25 nm by 2.95 nm, respectively. Figure 4-8 gives values of humidity sensitivities derived from linear fittings on the wavelength shifts. The humidity sensitivities of dip orders m_{61} and m_{60} are 0.0323 and 0.0427 nm/RH% with the corresponding R^2 values of 0.997, and 0.996, respectively.

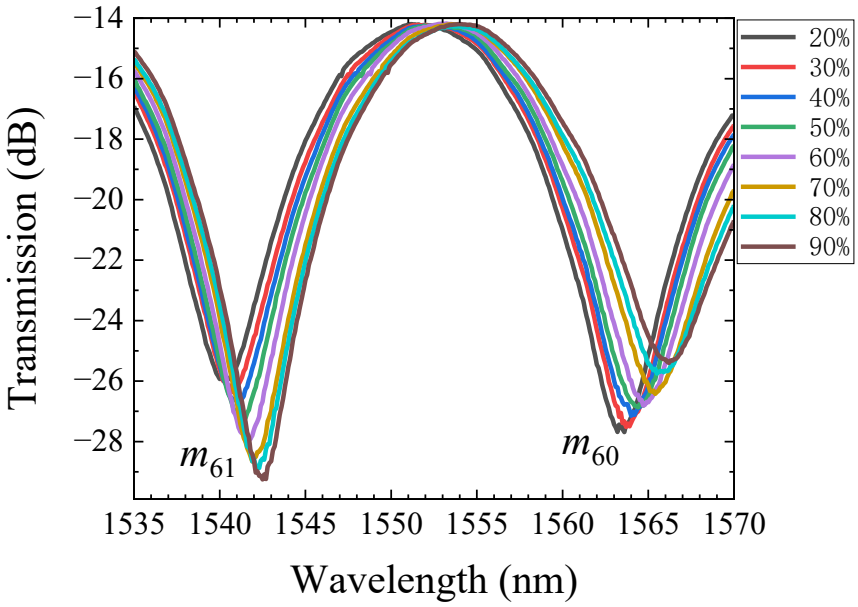

Figure 4-7: Transmission spectra of the GO-coated FMZI for interference orders 61 and 60 at different relative humidities at 40℃.

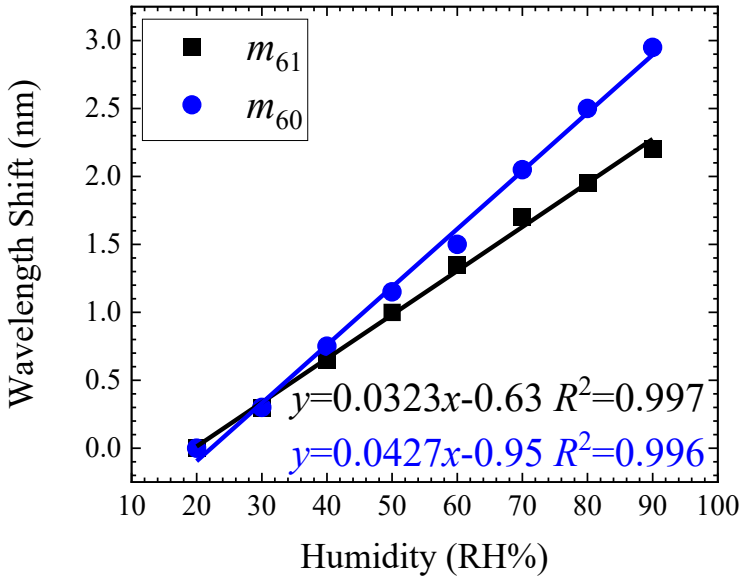

Figure 4-8: Wavelength shifts of dips of the GO-coated FMZI as a function of increasing humidity.

Wavelength shifts from two different interference dips can be used to eliminate the cross-sensitivity when the external environment changes. The dependence of the temperature and

humidity sensitivities on the dip wavelength shifts in the FMZI sensor when the conditions of the external environment change can be obtained from the following matrix of sensitivity coefficients:

$$\begin{bmatrix} \Delta T \\ \Delta RH \end{bmatrix} = \begin{bmatrix} S_{\mathrm{T}}^{m61} & S_{\mathrm{RH}}^{m61} \\ S_{\mathrm{T}}^{m60} & S_{\mathrm{RH}}^{m60} \end{bmatrix}^{-1} \begin{bmatrix} \Delta\lambda_{m61} \\ \Delta\lambda_{m60} \end{bmatrix} \tag{4-8}$$

where S_{T}^{m61} and S_{RH}^{m61} are the temperature and relative humidity sensitivities of the dip at m_{61}, S_{T}^{m60} and S_{RH}^{m60} are the temperature and relative humidity sensitivities of the dip at m_{60}, $\Delta\lambda_{\mathrm{m61}}$ and $\Delta\lambda_{\mathrm{m60}}$ are the shift of the dips m_{61} and m_{60}, respectively. This matrix can be employed to deduce the precise value of either temperature or humidity when one of the two conditions is already known. The results measured in the experiment are:

$$\begin{bmatrix} \Delta T \\ \Delta RH \end{bmatrix} = \begin{bmatrix} 0.0345 & 0.0323 \\ 0.0356 & 0.0427 \end{bmatrix}^{-1} \begin{bmatrix} \Delta\lambda_{m61} \\ \Delta\lambda_{m60} \end{bmatrix} \tag{4-9}$$

4.4 Graphene Oxide/ Sodium Alginate Coated Tapered Fiber Mach-Zehnder Interferometer

Owing to its excellent hydrophilic and water swelling properties, sodium alginate is mixed with graphene to create a 3D structured GO/Algin coating. Figure 4-9 shows the transmission spectra of GO/Algin-coated FMZI at different temperatures. As the temperature increases, the central wavelengths of the three dips with interference orders 61, 60, and 59 exhibit red-shifts, which changes from 1539.26 to 1541.24 nm by 1.98 nm, 1562.75 to 1564.91 nm by 2.16 nm, and 1584.71 to 1586.60 nm by 1.89 nm, respectively. Figure 4-10 shows the temperature sensitivities

of three dips, which indicate that the temperature sensitivities of m_{61}, m_{60}, and m_{59} are 0.0492 nm/°C (0.994), 0.0525 nm/°C (0.996), and 0.0462 nm/°C (0.996), respectively, the numbers in the brackets represent the R^2 values in linear fittings.

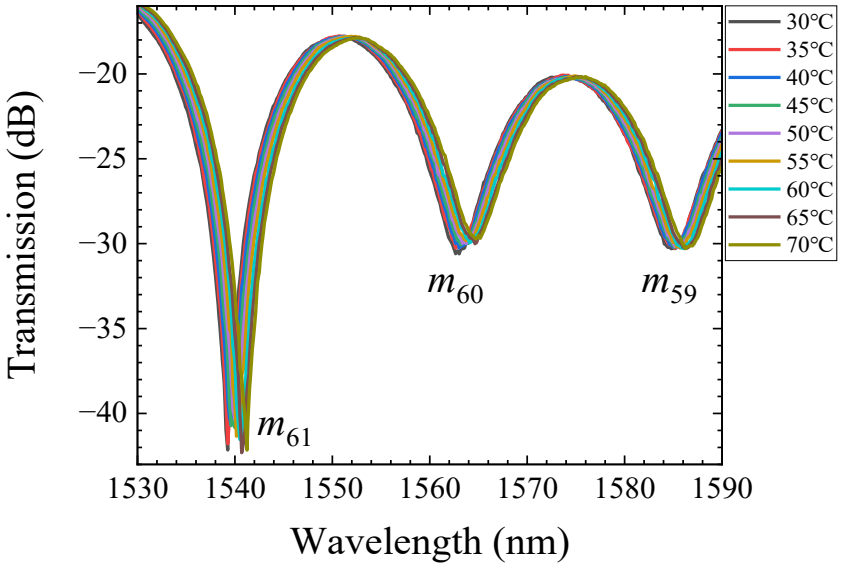

Figure 4-9: Transmission spectra of the GO/Algin-coated FMZI for interference orders 61, 60, and 59 at different temperatures with constant humidity of 40 RH%.

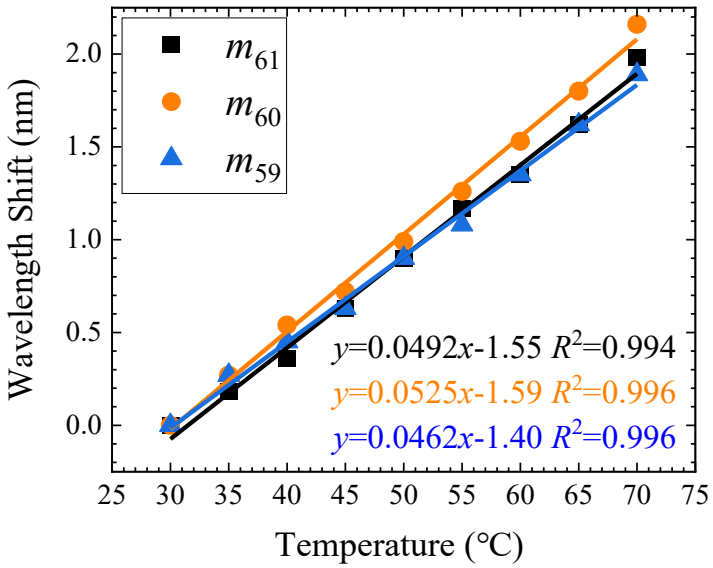

Figure 4-10: Wavelength shifts of dips of the GO/Algin-coated FMZI as a function of increasing temperature.

The GO/Algin-coated FMZI is placed in the environmental chamber at a temperature of 40°C. Figure 4-11 shows the transmission spectra of GO/Algin-coated FMZI at different relative humidity levels. As the humidity increases, the two dips with interference orders 61 and 60 show red-shifts. The dips of m_{61} and m_{60} shift from 1538.30 to 1539.50 nm by 1.20 nm, and 1561.90 to 1563.10 nm by 1.20 nm, respectively.

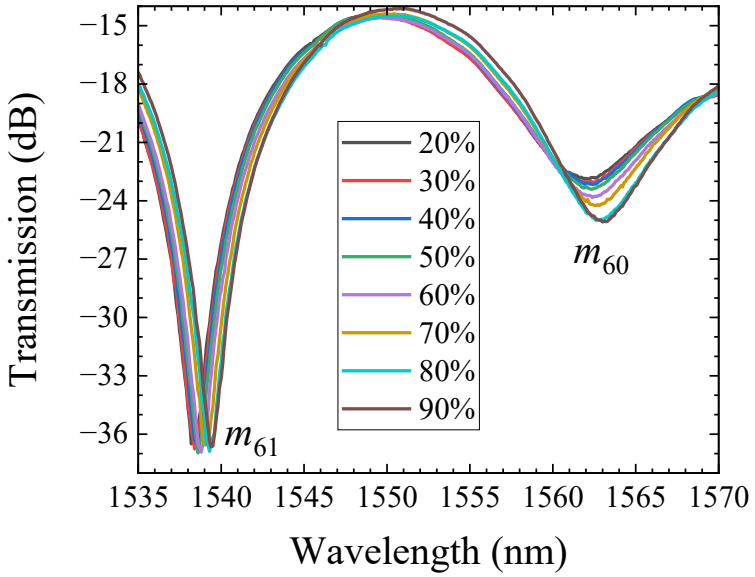

Figure 4-11: Transmission spectra of the GO/Algin-coated FMZI for interference order m_{61} and m_{60} at different humidity levels with constant temperature of 40°C.

Figure 4-12 shows the wavelength shift of each dip as humidity changes. It can be observed that a nonlinear relationship exists between the dip shift and RH in the measured range. In dip m_{61}, R^2 values of 0.993 and 0.998 are obtained for the humidity ranges of 20 to 50 RH% and 50 to 90 RH%, respectively. The corresponding sensitivities are found to be 0.0120 and 0.0215 nm/RH%. Moreover, in dip m_{60}, R^2 values of 0.992 and 0.996 are obtained in the 20 to 50 RH% and 50 to 90 RH%, respectively, with a sensitivity of 0.0135 and 0.0205 nm/RH%.

Figure 4-12 gives the humidity sensitivity at different interference orders, showing both dips shift to longer wavelengths with the change of surrounding RH, but the shift is nonlinear.

This is attributed to the water-absorbing and swelling properties of the three-dimensional structure of sodium alginate. When the environmental humidity is low, the coating exhibits uneven swelling of its outer and inner layers due to water sealing capacity. On the other hand, when the humidity rises to a certain level, the entire coating becomes fully penetrated by water molecules, resulting in increased sensitivity to variations in water molecule density in the surrounding environment.

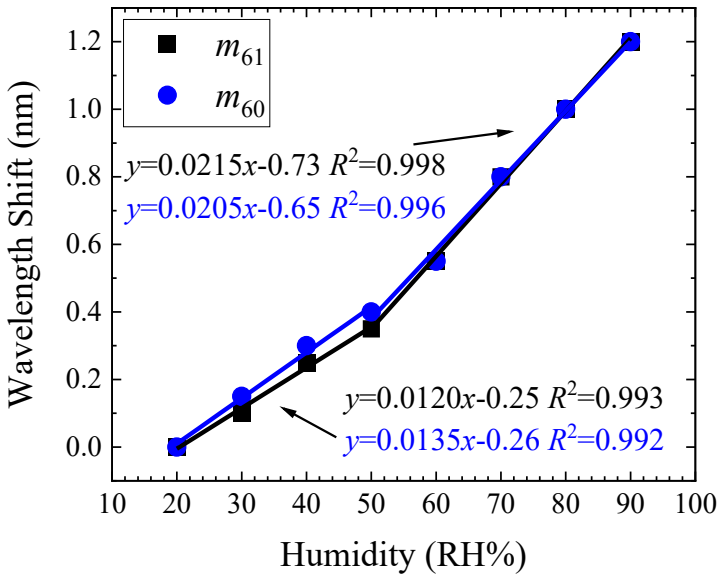

Figure 4-12: Wavelength shifts of dips of the GO/Algin-coated interferometer as a function of increasing humidity.

Eqn. (4-8) can be used to calculate the wavelength shift of dip m_{61} and m_{60}. The relations corresponding to the humidity level lower or higher than 50% are revealed in Eqns. (4-10) and (4-11), respectively:

$$\begin{bmatrix} \Delta T \\ \Delta RH \end{bmatrix} = \begin{bmatrix} 0.0492 & 0.012 \\ 0.0525 & 0.0135 \end{bmatrix}^{-1} \begin{bmatrix} \Delta\lambda_{m61} \\ \Delta\lambda_{m60} \end{bmatrix} \tag{4-10}$$

$$\begin{bmatrix} \Delta T \\ \Delta RH \end{bmatrix} = \begin{bmatrix} 0.0492 & 0.0215 \\ 0.0525 & 0.0205 \end{bmatrix}^{-1} \begin{bmatrix} \Delta\lambda_{m61} \\ \Delta\lambda_{m60} \end{bmatrix} \tag{4-11}$$

4.5 Graphene Oxide/Fullerenol: Hydrogel Coated Fiber Mach-Zehnder Interferometer

The transmission spectra of tapered FMZI coated with GO/$C_{60}(OH)_n$: Hydrogel at different temperatures are shown in Figure 4-13.

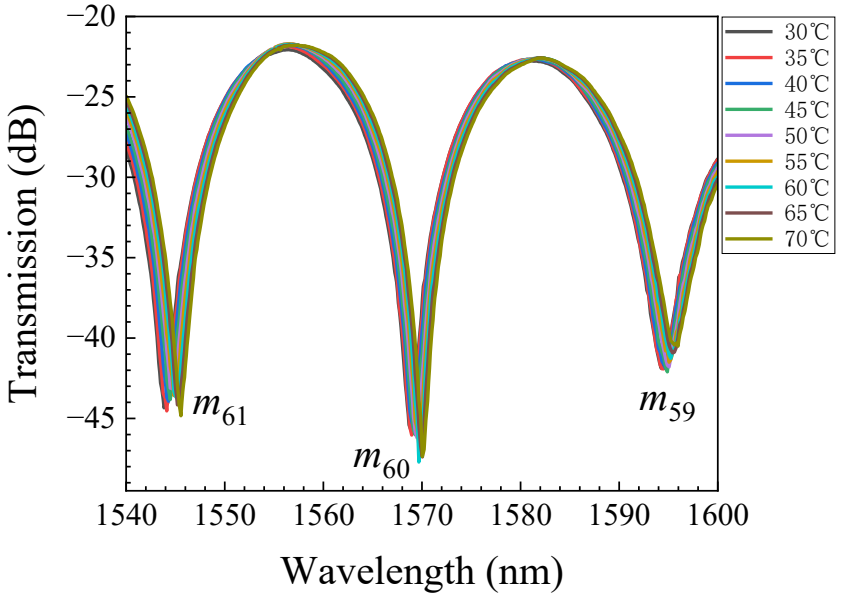

Figure 4-13: Transmission spectra of GO/$C_{60}(OH)_n$: Hydrogel-coated FMZI for interference order 61, 60, 59 at different temperatures when relative humidity is 40 RH%.

As the temperature increases, all three dips with interference orders 61, 60, and 59 exhibit red-shifts in the transmission spectra. The dips m_{61}, m_{60} and m_{59} shift from 1543.94 to 1545.56 nm by 1.62 nm, 1568.78 to 1570.22 nm by 1.44 nm, and 1594.25 to 1595.69 nm by 1.44 nm, respectively. The shift of dips m_{60} and m_{59} show the same magnitude. Figure 4-14 gives the fittings on the wavelength shifts of three dips. The temperature sensitivities of m_{61}, m_{60}, and m_{59}

can be derived as 0.0402 nm/°C (0.997), 0.0351 nm/°C (0.992), and 0.0351 nm/°C (0.992), respectively, with the numbers in the brackets represent the R^2 values obtained from linear fittings.

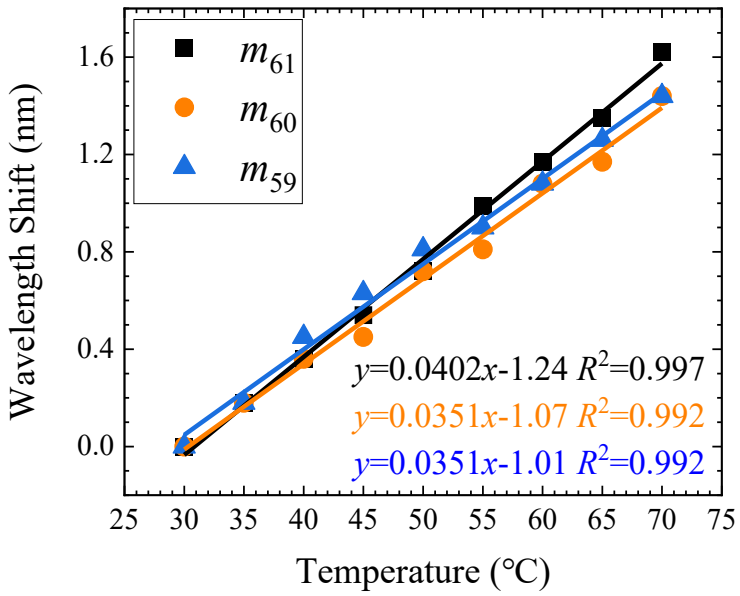

Figure 4-14: Wavelength shifts of dips of the transmission spectra of the GO/$C_{60}(OH)_n$: Hydrogel-coated FMZI as a function of increasing temperature.

Figure 4-15 (a) shows the transmission spectra of GO/$C_{60}(OH)_n$: Hydrogel-coated FMZI at different levels of RH in the environmental chamber while the temperature remains constant at 40°C. Figures 4-15 (c) and (d) show the enlarged spectral curves of each dip. As the humidity increases, the dip m_{61} remains at the same wavelength. However, dip m_{60} shows a red-shift when the humidity is above 50 RH%.

The shift of dips m_{61} and m_{60} at different humidity levels are shown in Figure 4-16. The wavelengths of the dip m_{61} at different humidity levels remain roughly the same with a fluctuation within the resolution of the OSA (0.05 nm), which can be regarded as humidity insensitive. The dip wavelength of m_{60} remains constant when the RH is between 20 to 50 RH%

and then shifts to longer wavelengths as the humidity increases. The humidity sensitivity of dip m_{60} at the humidity above 50% is 0.0075 nm/RH% with $R^2 = 0.987$.

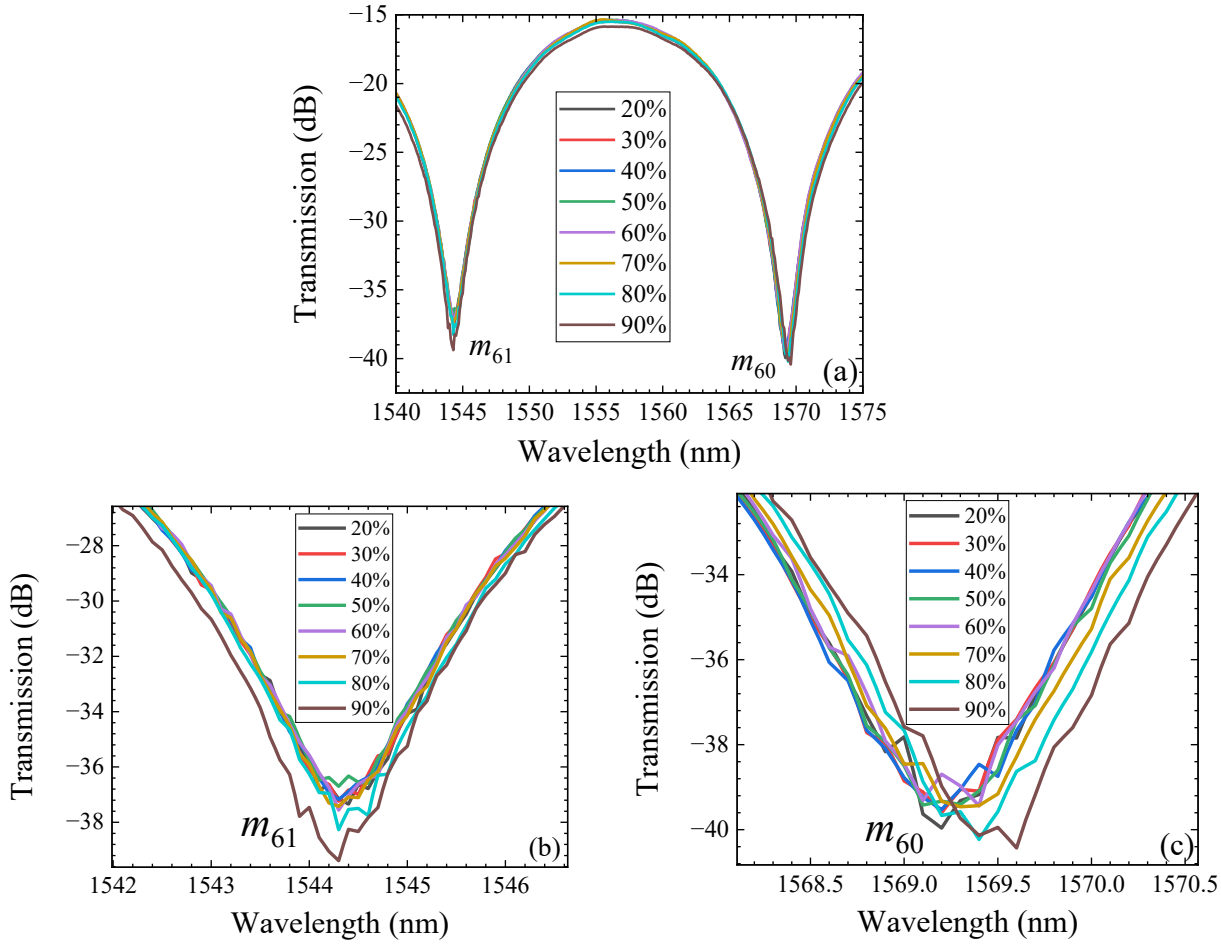

Figure 4-15: Transmission spectra of the GO/$C_{60}(OH)_n$: Hydrogel-coated FMZI at different humidity levels with the temperature of 40℃. (a) Transmission spectra, enlarged figure of dip (b) m_{61} and (c) m_{60}.

The GO/$C_{60}(OH)_n$: Hydrogel-coated tapered FMZI exhibits a low sensitivity with the change of humidity, as well as a nonlinear change. Both GO/Algin and GO/$C_{60}(OH)_n$: hydrogel-coated tapered FMZI show insensitivity at low humidity because the water sealing effect of the coating requires the humidity to increase to a certain level so that the water molecules are able to pass through the coating and thus affect the interferometer. This phenomenon reduces the capability of the device on humidity measurements at low humidity scenarios.

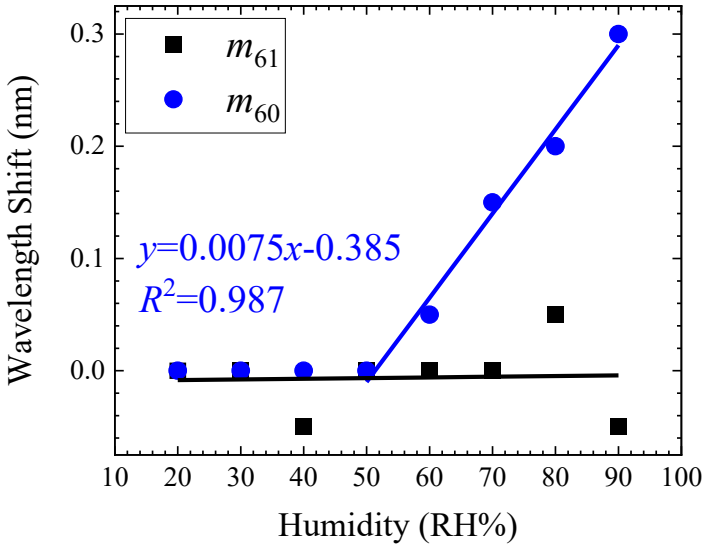

Figure 4-16: Wavelength shifts of the GO/$C_{60}(OH)_n$: Hydrogel-coated FMZI as a function of increasing humidity.

Equations (4-8) can be utilized to calculate the wavelength shifts of dip m_{61} and m_{60}. The equations corresponding to humidity levels lower and higher than 50% are described in Eqn. (4-12) and (4-13) respectively:

$$\begin{bmatrix} \Delta T \\ \Delta RH \end{bmatrix} = \begin{bmatrix} 0.0402 & 0 \\ 0.0351 & 0 \end{bmatrix}^{-1} \begin{bmatrix} \Delta\lambda_{m61} \\ \Delta\lambda_{m60} \end{bmatrix} \tag{4-12}$$

$$\begin{bmatrix} \Delta T \\ \Delta RH \end{bmatrix} = \begin{bmatrix} 0.0402 & 0 \\ 0.0351 & 0.0075 \end{bmatrix}^{-1} \begin{bmatrix} \Delta\lambda_{m61} \\ \Delta\lambda_{m60} \end{bmatrix} \tag{4-13}$$

4.6 Graphene Oxide Coated Bulge-Fused Fiber Mach-Zehnder Interferometer

Figure 4-17 illustrates the transmission spectrum of an uncoated bulge-fused FMZI at different temperatures. The device consists of two bulge-fused components with a separation of 2.0 ± 0.1 cm. When the temperature is increased from 30 to 70°C, all three dips with interference orders 60, 59, and 58 shift to a longer wavelength. The wavelength shifts of dips m_{60}, m_{59}, and m_{58} are found from 1539.49 to 1541.47 nm by 1.98 nm, 1561.85 to 1564.37 nm by 2.52 nm, and 1587.68 to 1590.29 nm by 2.61 nm, respectively.

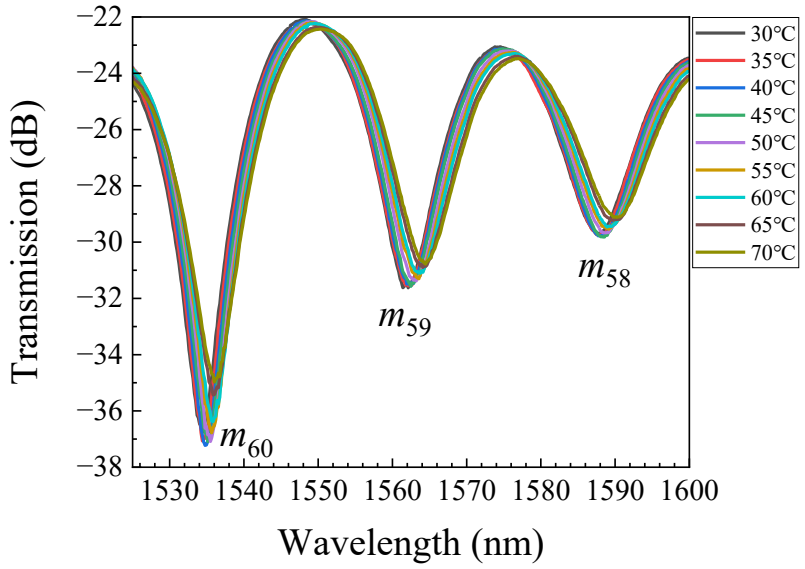

Figure 4-17: Transmission spectra of the uncoated bulge-fused FMZI for interference orders 61, 60, and 59 at different temperatures and constant humidity of 40 RH%

Figure 4-18 shows the results of linear fitting on the temperature sensitivities of these three dips. The dip m_{60} shows a linear dependence on the increasing temperature with a temperature sensitivity of 0.492 nm/°C, and R^2 value of 0.996. The temperature sensitivity of m_{59}

is 0.0636 nm/°C with R^2 = 0.986. The relationship between the dip wavelength shift and temperature of m_{59} and m_{58} are $0.000608x^2 + 0.00282x - 0.65$ and $0.000725x^2 - 0.00887x - 0.35$, where x is the temperature. The R^2 values for the linear fits of m_{60} and m_{59} are both 0.997.

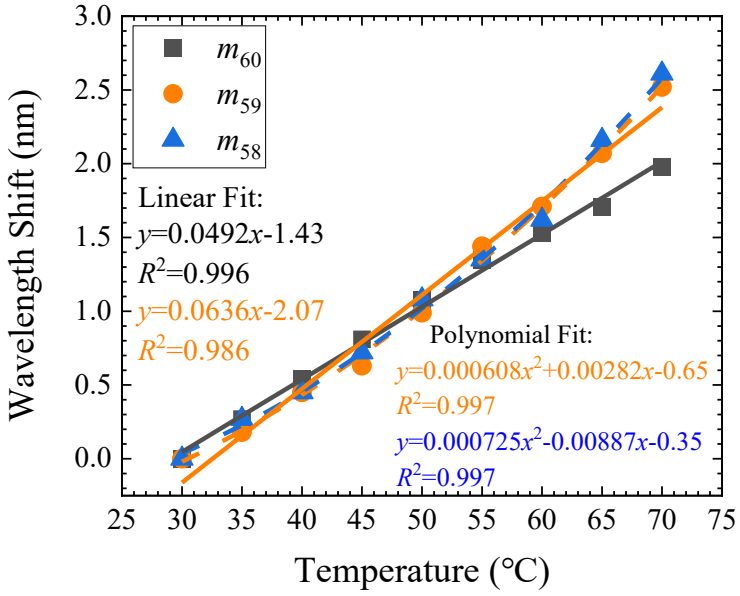

Figure 4-18: Dip shifts of the uncoated bulge-fused interferometer as a function of increasing temperature.

Figure 4-18 shows, as the number of interferences order decreases, the R^2 value of the linear relationship between dip shift and temperature decrease. Therefore, the bulge-fused is adopted to measure the humidity sensitivity at 40°C. The transmission spectra at different humidity levels are shown in Figure 4-19 (a), with the enlarged spectra curves of dip m_{60} and m_{59} shown in (b) and (c), respectively.

From Figure 4-19, the dip m_{59} shows no shift with the change of RH, and the dip m_{60} shows a blue-shift with the increase of surrounding RH. The dip m_{60} shifts from 1534.20 to 1533.80 nm by 0.40 nm. Figure 4-20 represents the dip shifts of dip m_{60} as humidity changes. The dip m_{60} shows a linear relation with the increasing humidity with the sensitivity -0.00542 nm/RH% with R^2 = 0.988.

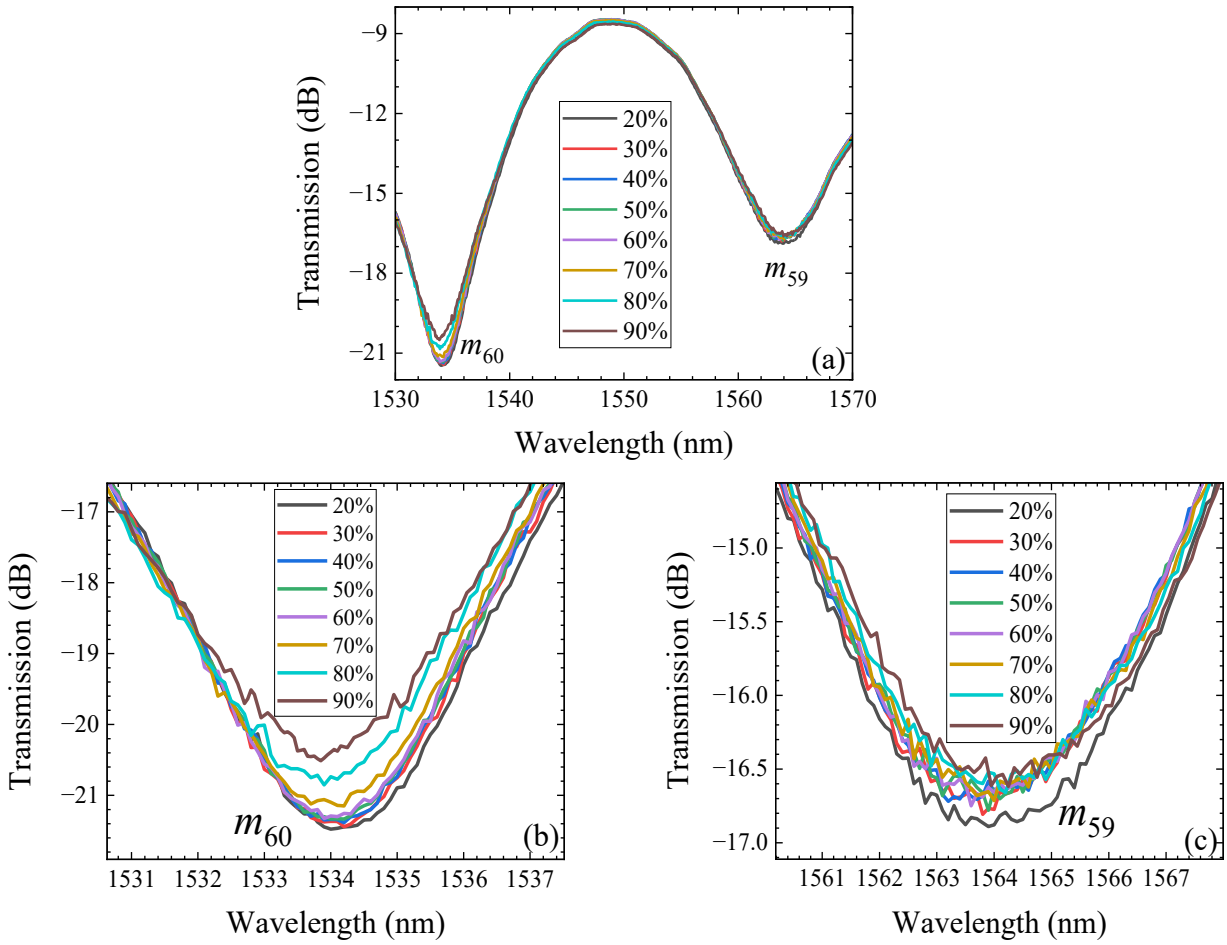

Figure 4-19: Transmission spectra of the uncoated bulge-fused FMZI at different humidity levels with the temperature of 40℃. (a) Transmission spectra, enlarged figure of dip (b) m_{60} and (c) m_{59}.

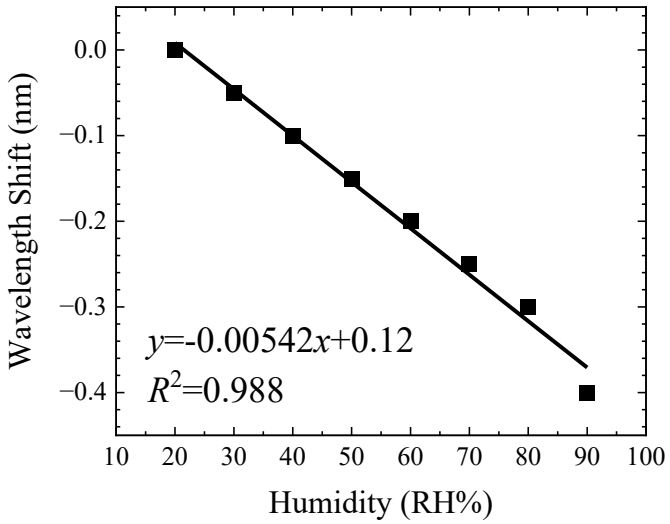

Figure 4-20: Wavelength shifts of the uncoated bulge-fused FMZI for dip m_{60} as a function of increasing humidity.

The bulge-fused FMZI with 6.0 µm coating is used to measure the temperature sensitivity, and the transmission spectra at different temperatures are shown in Figure 4-21 (a). The dip m_{60} shows a red-shift from 1532.33 to 1534.85 nm by 2.52 nm. The dip m_{59} shifts to the longer wavelength region by 2.34 nm from 1563.74 to 1566.08 nm, and m_{58} shifts from 1589.39 to 1591.46 nm by 2.07 nm.

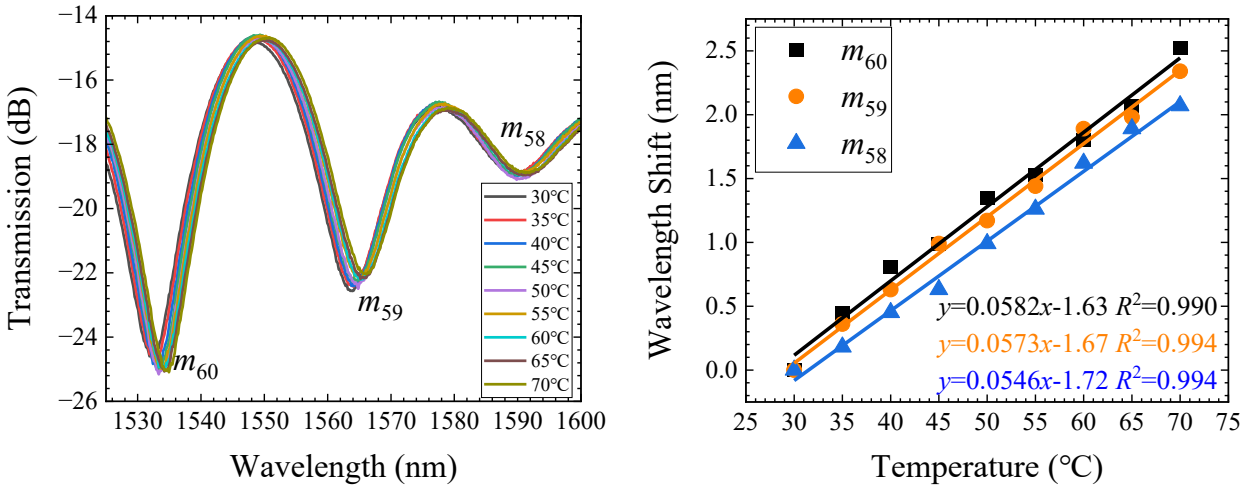

Figure 4-21: GO-coated bulge-fused FMZI at different temperatures and constant humidity of 40 RH%. (a) Transmission spectra. (b) Dependence of wavelength shifts on different temperatures for interference orders 60, 59, and 58.

Figure 4-21 (b) shows the result of linear fitting on the temperature sensitivities of three dips. The temperature sensitivities of m_{60}, m_{59}, and m_{58} are 0.0582 nm/°C (0.990), 0.0573 nm/°C (0.994), and 0.0546 nm/°C (0.994), respectively, in which the numbers in the brackets represent the R^2 values obtained from linear fittings.

From Figure 4-22 (a), the dips m_{60} and m_{59} shift to a shorter wavelength with the increasing humidity, and the enlarged spectra curves of dip m_{60} and m_{59} are shown in Figure 4-22 (b) and (c), respectively. Dip m_{60} experiences a wavelength shift from 1533.35 to 1532.75 nm, resulting in a shift of 0.60 nm. On the other hand, dip m_{59} undergoes a blue-shift from 1564.50 to 1564.05 nm, with a shift of 0.45 nm.

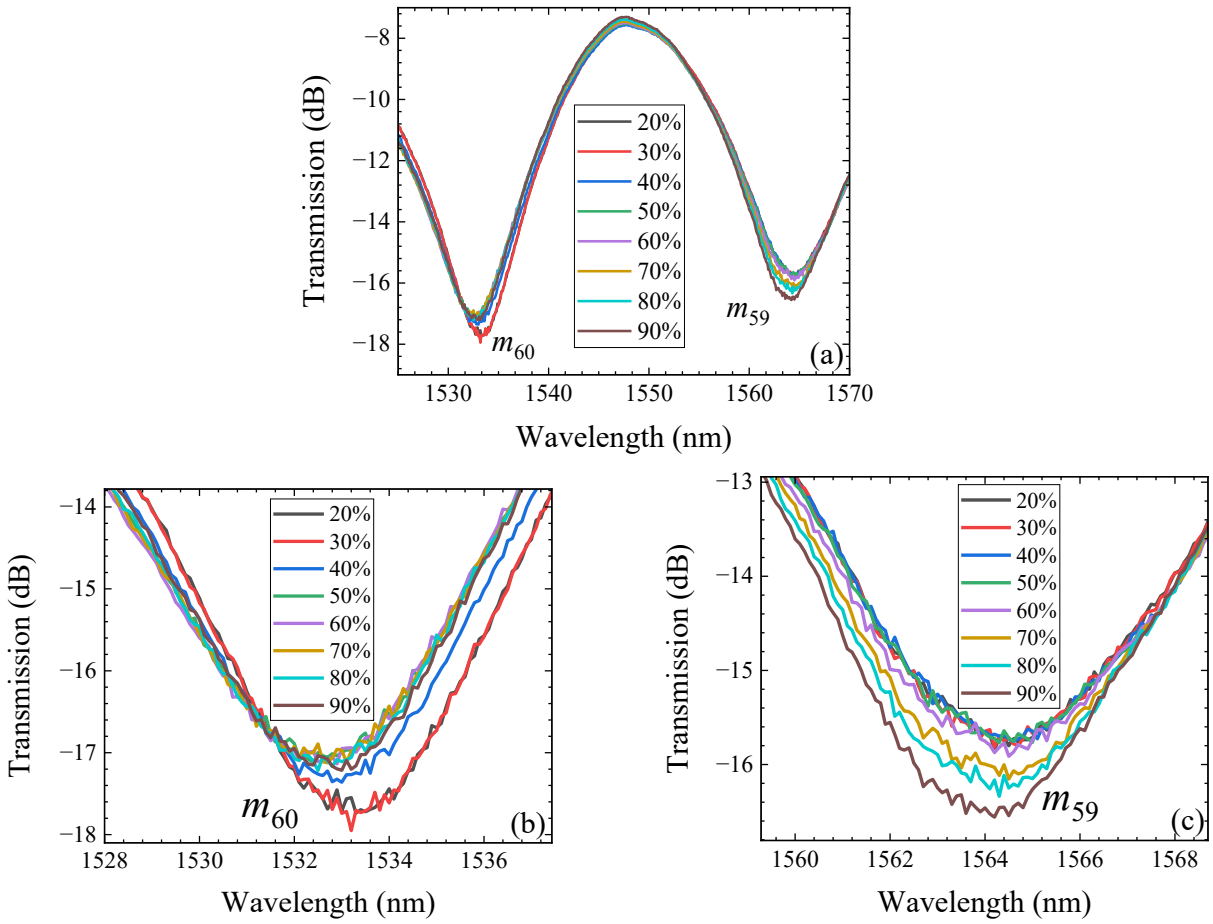

Figure 4-22: Transmission spectra of the GO-coated FMZI at different humidity levels with the temperature of 40°C. (a) Transmission spectra, enlarged figure of dip (b) m_{60} and (c) m_{59}.

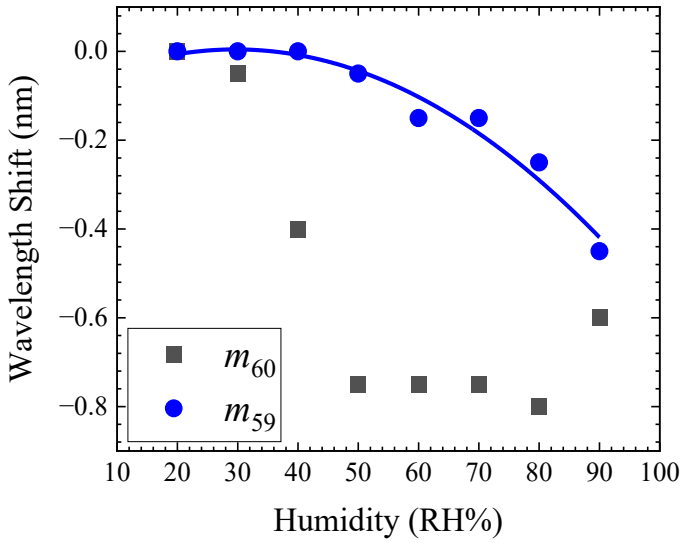

Figure 4-23: Wavelength shifts of dips of the GO-coated bulge-fused interferometer as a function of increasing humidity.

Figure 4-23 shows the dips m_{60} and m_{59} at different humidity levels. As the humidity is increased from 20 to 50 RH%, the dip wavelength of m_{60} shows a blue-shift of 0.75 nm, but with a further increase in humidity, a red-shift of 0.2 nm occurs at 90 RH%.

The temperature sensitivity of m_{60} increases by 18.29% after coating, whereas the temperature sensitivity of m_{59} decreases by 9.91%. However, the dip shift is linearly related to the temperature change after coating, which is more favourable for sensing applications. The GO coating increases the blue-shift in both dips of the spectrum during humidity measurement, as Eqn. (4-7) indicates that the RI of the GO coating decreases with increasing humidity, so the interferometric arm between the two bulge-fused components serves as the main sensing area of the bulge-fused FMZI for humidity measurement.

Chapter 5 Curvature Sensitivity of Graphene Oxide Coated Tapered Fiber Mach-Zehnder Interferometers

Bending deformation measurement plays an important role in mechanical engineering and structural health monitoring, such as mechanical bending angle measurement, human posture detection, bridge and road construction, and structural deformation [93]. In 1980, American researchers J. N. Fields and J. H. Cole proposed the fiber micro-bend sensor for the first time [94]. Various optical fiber bending sensors can be divided into several categories according to the modulation principles: intensity modulation [95], wavelength modulation [96], and frequency modulation [97]. Since then, many optical fiber curvature sensors have been developed by using various optical devices, such as fiber gratings [98], interferometers [99] and special fiber devices [100,101]. The FMZI is desirable due to its small size and simple configuration. Several fabrication techniques have been successfully implemented, such as peanut-shape structure [102], waist-enlarged structure [103], abrupt-tapers [104] and others.

This chapter will discuss tapered FMZI with GO-based coatings used to measure curvature sensitivity. During curvature measurements, deformation occurs between the fiber core and the cladding, allowing more core modes to leak into the cladding modes results in wavelength shifts. During the bending process, the taper region is more affected by deformation due to its lower diameter, allowing more light to be coupled to the cladding. The performance of the tapered structure in curvature measurements is improved by changing the interference pattern

of the cladding mode by applying different high-refractive index coatings to the taper region. The effect on the dip wavelength shift with the curvature changing will be studied.

5.1 Sensing Mechanisms and Experimental Details

The distribution of refractive index over a bent fiber can be found by converting a curved fiber into an equivalent straight fiber by the conformal mapping technique, as illustrated in Figure 5-1. The distribution of refractive index $n_c(x,y)$ after the coordinate transformation is [105, 106]:

$$n_c = n_0 e^{\frac{x}{R}} \approx n_0(1+\frac{x}{R}) \tag{5-1}$$

where n_0 is the refractive index profile when the fiber is uncurved, R is the curvature radius, and x is a coordinate along a line connecting the center of fiber and curvature.

The exponential term accounts for the increase in optical path length along the fiber with distance from the center of curvature. This means a tilted refractive index profile with a decrease for the stretched outer part and an increase for the compressed inner part.

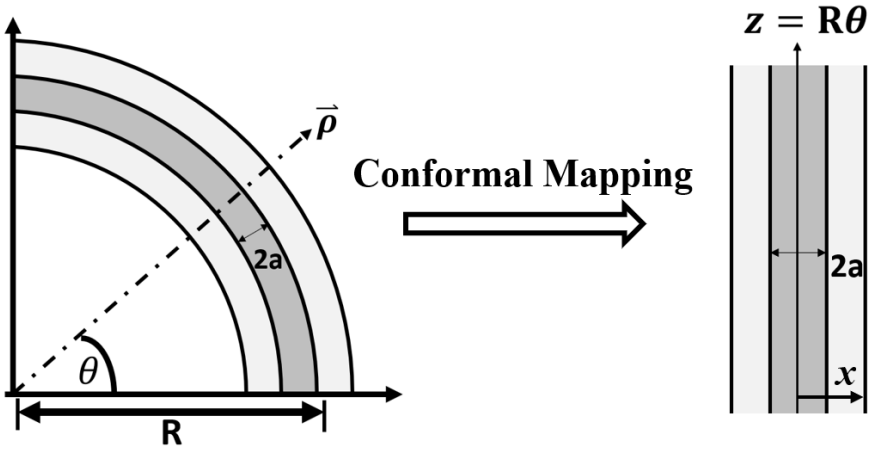

Figure 5-1: Schematic diagram of a circularly bent fiber and its equivalent straight fiber after conformal mapping.

An additional change occurs to the physical refractive index of the fiber upon bending due to stress-optic effects. When a compression along the inner side of the fiber occurs, towards the center of the bend, while a tension emerges along the outer side, the refractive index of the material will vary according to the following [106, 107]:

$$n_0 = n\left[1 - \frac{n^2 x}{2R}[P_{12} - \nu(P_{11} + P_{12})]\right] \tag{5-2}$$

where n is the refractive index of the straight fiber, ν is Poisson's ratio, and P_{11} and P_{12} are components of the photo-elastic tensor. The refractive index tilts with bending, but in this case, it typically decreases toward the outside of the bend.

Eqn. (5-2) can be substituted into Eqn. (5-1) to find the equivalent bend radius as:

$$R_{\text{eff}} \equiv \frac{R}{1 - \frac{n^2}{2}[P_{12} - \nu(P_{11} + P_{12})]} \tag{5-3}$$

In the silica fiber $R_{\text{eff}} \approx 1.28R$ [108]. Refractive index distribution after coordinate transformation incorporating the effect of optic stress is:

$$n_{\text{c}} = (1 + \frac{x}{1.28R}) \tag{5-4}$$

Combining Eqn. (1-7) with Eqn. (5-4), the sensitivity of curvature is defined as:

$$\frac{d\lambda_m}{dC} = \lambda_m[\frac{1}{n}\frac{\partial n}{\partial C} + 1] \tag{5-5}$$

where C represents the curvature in units of m^{-1} and $C = 1/R$.

The asymmetric index profile will change the symmetry of the cladding modes. The direction and rate of the dip shift during the bending process determine which cladding modes dominate in interfering with the core modes.

Due to the phase match condition, the intensity of the dip varies periodically with the bending of the fiber: [108]

$$T_m = 1 - |\sin(k_m L)|^2 \tag{5-6}$$

where the k_mL is the coupling strength for m^{th} cladding mode.

When $k_mL = \pi/2$, the light is completely coupled to the cladding mode resulting in a 100% transmission loss, whereas all the light is coupled back to the core mode, indicating a zero-transmission loss if $k_mL = \pi$.

Figure 5-2 shows the simulation on the light energy density distribution along tapered FMZI with a tapered diameter of 80 μm at a wavelength of 1550 nm. It is apparent from the figure that, as the curvature increases, the angle of incidence of light changes, and light from the core mode leaks out of the taper region and couples to the cladding mode, and the edge of the tapered structure also affects the propagation mode of the light in the fiber.

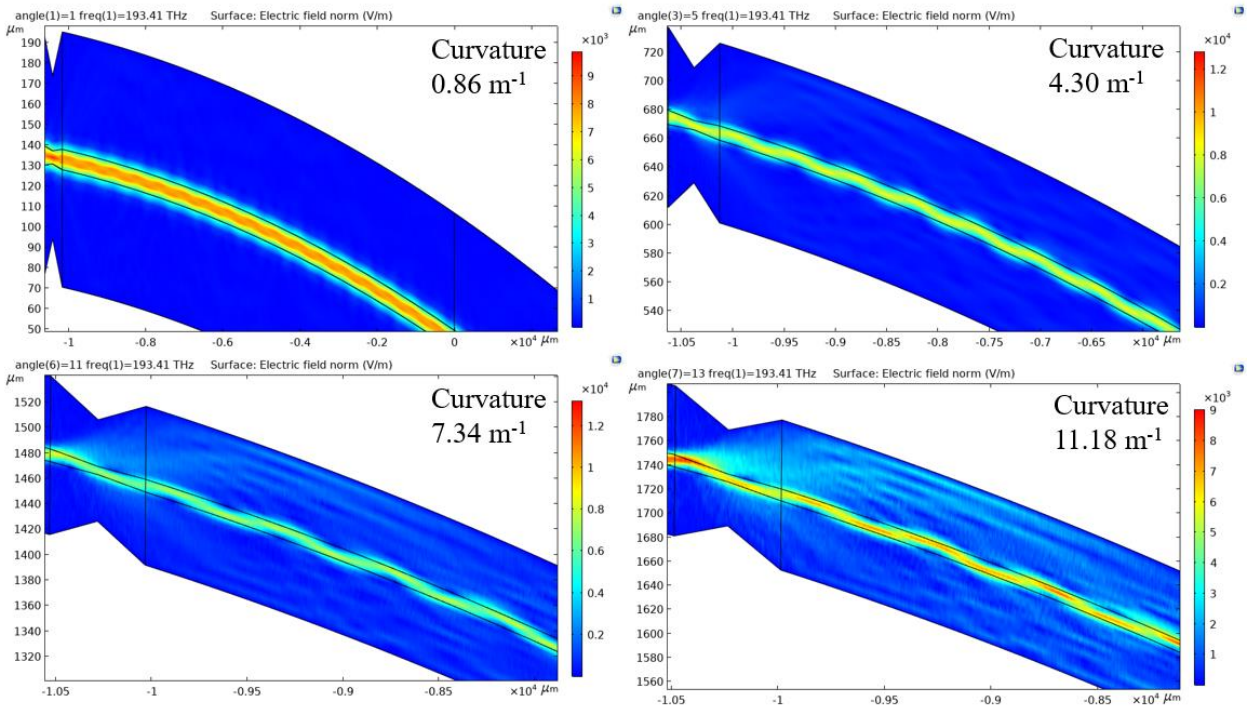

Figure 5-2: Simulation on the light energy density distribution along the uncoated tapered FMZI at different curvatures.

The tapered FMZI (without and with coating) is bent during the experiment at room temperature (20℃) to measure the curvature, as shown in Figure 5-3. An EBS-7201 is a light source, and the optical spectrum analyzer receives light passing through the FMZI. The fiber sample is fixed to one fixed and one moveable translation stages at the two ends of the device using tape. The curvature of the fiber varies with the distance between those two translation stages. The relationship between the radius of curvature and displacement can be obtained from the following equation: [109]

$$R\sin(\frac{L}{2R}) = \frac{L-d}{2} \tag{5-7}$$

where L is the distance between the two translation stages, d is the displacement of the stage, and R is the radius of curvature.

The bending curvature can be calculated by: [110]

$$C = \sqrt{\frac{24d}{(L-d)^3}} \tag{5-8}$$

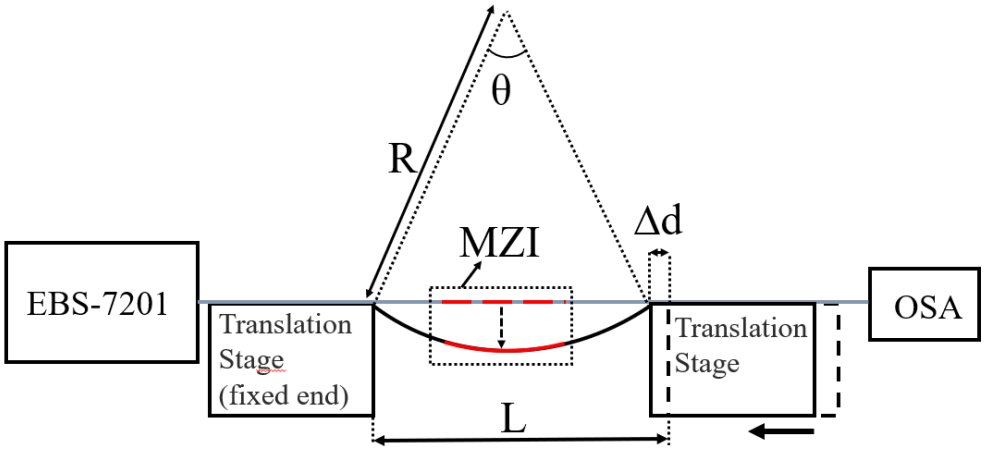

Figure 5-3: Schematic diagram of the experimental setup for curvature measurement.

In the experiment, the measurement range of the transmission spectrum is 1520 to 1610 nm. The initial separation between the two translation stages is 21.2 cm, the accuracy of the motion stage is 10.0 μm, and the maximum displacement is 1.5 cm. By using Eqn. (5-8), the range of the curvature measurement can be calculated to be in the range from 0 to 7.86 m^{-1}.

5.2 Curvature Sensitivity of Uncoated Tapered Fiber Mach-Zehnder Interferometer

As the curvature increases, the transmission spectra of uncoated tapered FMZI at different curvatures are shown in Figures 5-4 (a) and (b). It can be found from the figure below that the dip wavelength exhibits a blue-shift with increasing curvature and a gradual decrease of the intensity of the dip until it disappears at a curvature of 4.20 m^{-1}. Subsequently, the intensity of the dip increases gradually with increasing curvature, as shown in Figure 5-4 (b). The Fourier transformation is used to further analyze the effect of curvature on propagation modes by selecting some data in the middle of the measurement range in both transmission spectra, as shown in Figure 5-4 (c). When the curvature is below 4.20 m^{-1}, there is a dominant peak with a spatial frequency of 0.033 nm^{-1} and a 0.078 nm^{-1} minor peak. Furthermore, when the curvature is above 4.20 m^{-1}, the amplitude of the dominated peak rapidly declines with two peaks at 0.022 and 0.044 nm^{-1}. Although the amplitude of the minor peak 0.078 nm^{-1} is invisible at high curvature, the amplitude of the minor peak increases with the increasing curvature when the curvature is between 1.57 to 4.20 m^{-1}.

Figure 5-5 illustrates the wavelength shifts of dips m_{60}, m_{59}, and m_{58}, from which the sensitivity of the curvature can be obtained by calculating the slope of the linear fitting of the wavelength shift using Eqn. (5-5). The curvature sensitivities of m_{60}, m_{59}, and m_{58} are -11.11 nm/m^{-1} (0.980), -10.20 nm/m^{-1} (0.992), and -12.79 nm/m^{-1} (0.993), respectively, in which the numbers in the brackets represent the R^2 values obtained from linear fittings. The dip m_{59} exhibits a higher curvature sensitivity, and m_{60} and m_{58} show similar curvature sensitivities.

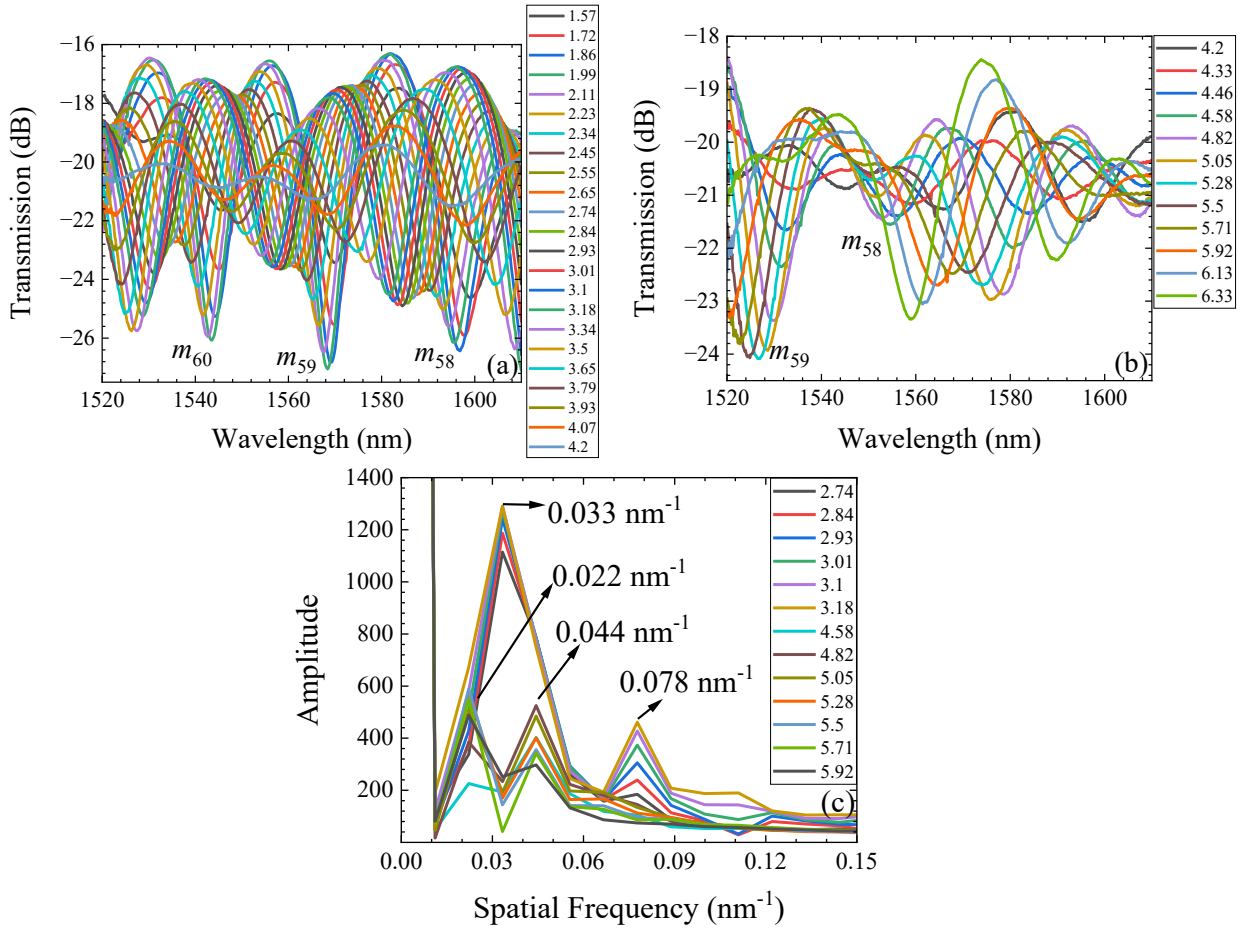

Figure 5-4: Transmission spectra are recorded at various curvatures ranging from (a) 1.57 to 4.20 m^{-1}, (b) 4.20 to 6.33 m^{-1}, and (c) FFT of the spectra.

When the curvature is 4.20 m^{-1}, a discontinuous break in the wavelength shift appears, then shows a different sensitivity with the increasing curvature. This phenomenon is attributed to

the fact that the tapered segment has a smaller diameter. When the FMZI is bent to a certain level, the tapered segment is subjected to a larger deformation, allowing more light to be coupled to the cladding, resulting in a change in the coupling pattern. As shown in Figure 5-4 (c), the changes in the main interference pattern when the curvature is above 4.20 m^{-1}.

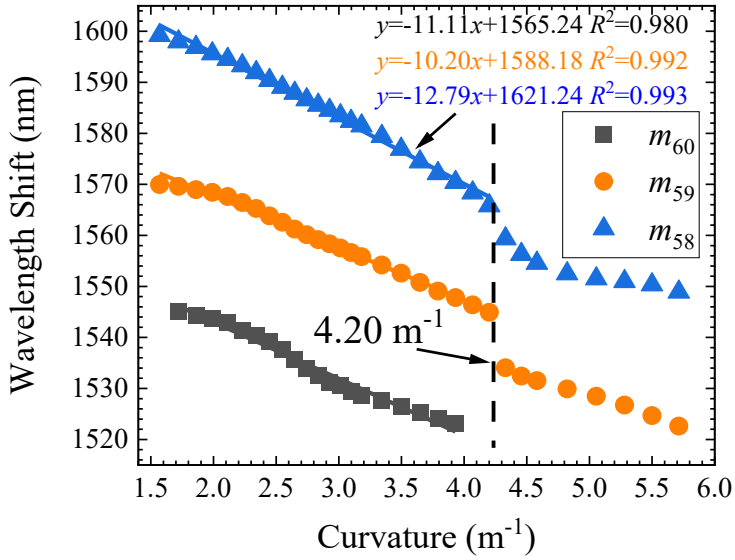

Figure 5-5: Dependence of wavelength shifts of uncoated FMZI on the increase of curvature and the results of linear fitting for dips m_{60}, m_{59}, and m_{58}.

5.3 Curvature Sensitivity of Graphene Oxide Coated Fiber Mach-Zehnder Interferometer

The GO-coated FMZI is used for measuring the curvature sensitivity due to the excellent optical absorption characteristics of graphene. Graphene exhibits strong polarization-dependent optical absorption in total internal reflection that it absorbs the TE (transversal electric wave) mode more than the TM (transversal magnetic wave) [111]. The GO coating absorbs some higher-

order cladding modes under large curvature. Moreover, the strength of the coating can reduce the effect of bending on the spectrum caused by the tapered segment.

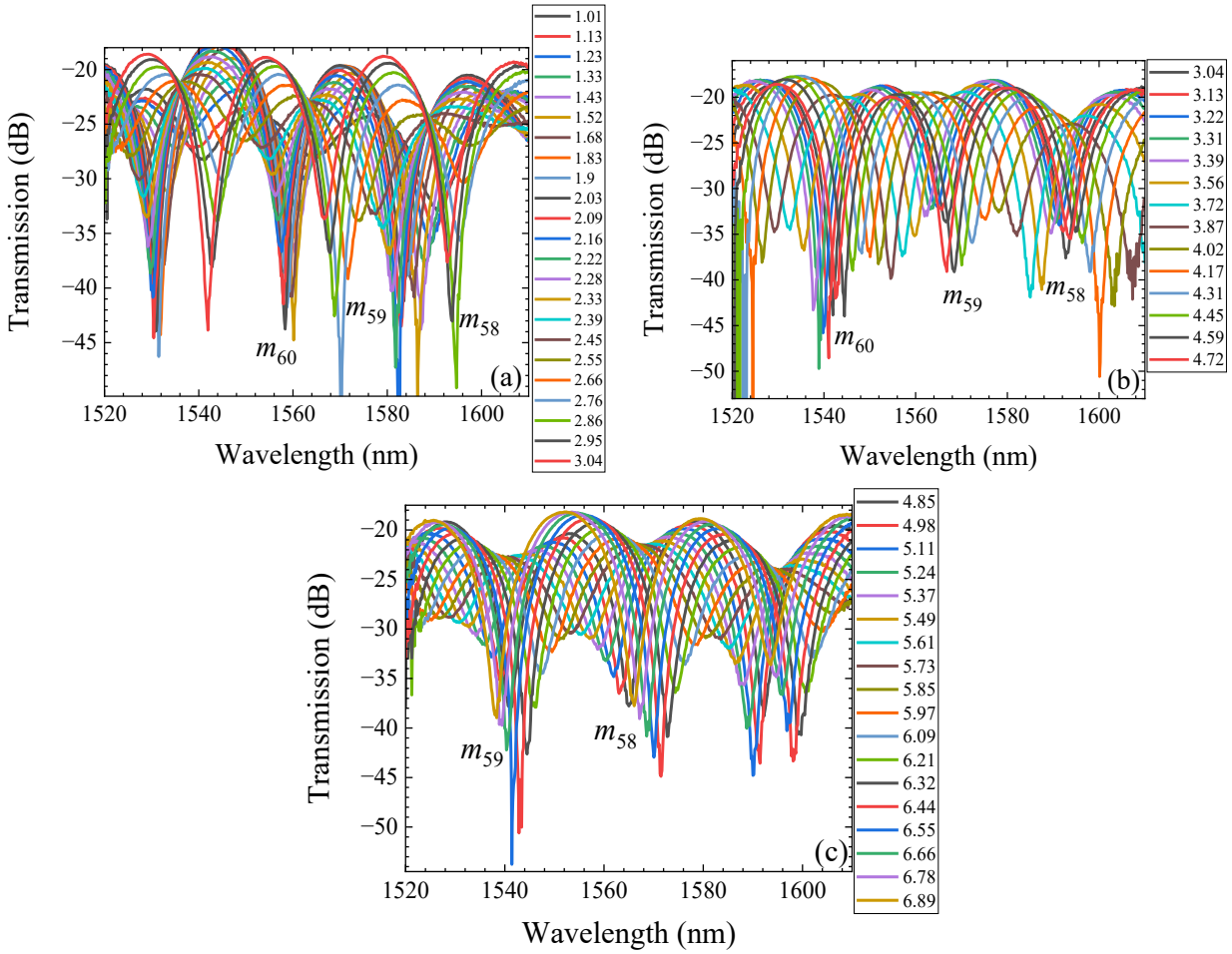

Figure 5-6: Transmission spectra of the GO-coated tapered FMZI, which are recorded at various curvatures ranging from (a) 1.01 to 3.04 m^{-1}, (b) 3.04 to 4.72 m^{-1}, and (c) 4.85 to 6.89 m^{-1}.

Figure 5-6 depicts the transmission spectra of GO-coated FMZI at different curvatures, which indicate that the dip wavelength exhibits a blue-shift with increasing curvature. Additionally, according to Eqn. (5-6) the intensity of the dip undergoes periodic changes as the curvature increases, completing the first cycle of variation at a curvature of 2.45 m^{-1}, as shown in Figure 5-6 (a). Figure 5-6 (b) and (c) illustrate that the intensities of the transmission spectra exhibit periodic changes with a further increase in curvature. The effect of curvature on the

propagation pattern is then further analyzed by FFT by selecting some data in the middle of the measurement range, as shown in Figure 5-7.

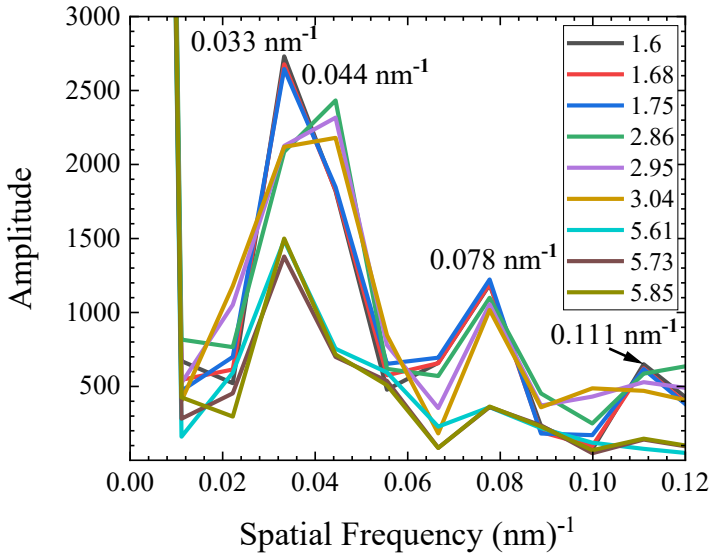

Figure 5-7: FFT of the transmission spectra of the GO-coated tapered FMZI.

Figure 5-7 shows the FFT of the transmission spectra of the GO-coated FMZI at different curvatures. When the curvature is smaller than 2.45 m^{-1}, a dominant peak with a spatial frequency of 0.033 nm^{-1} and two minor peaks at 0.078 and 0.111 nm^{-1} can be found. Furthermore, when the curvature is around 2.95 m^{-1}, the dominant peak is located between 0.033 to 0.044 nm^{-1}, with a minor peak at 0.078 nm^{-1}. When the curvature increases to 5.61 m^{-1}, the dominant peak is located at 0.033 nm^{-1}, and the minor peak exists at 0.078 nm^{-1}. The phenomenon here shows that the amplitude of each peak decreases as the curvature increases. Additionally, at higher curvatures, the transmission spectrum is less affected by minor cladding modes due to the decreased amplitude of minor peaks.

Figure 5-8 shows the wavelength shifts of dips m_{60}, m_{59}, and m_{58}. The curvature sensitivity is the slope of the linear fitting lines of the dip shift. Since a turning point exists at a curvature of 2.45 m^{-1} in the curve, the two ranges of curvature have been found to possess two

different sensitivities. When the curvature is smaller than 2.45 m^{-1}, the curvature sensitivity of m_{60} is found to be -4.65 nm/m^{-1} with an R^2 value of 0.974. Similarly, the curvature sensitivity of m_{59} is determined to be -7.23 nm/m^{-1} with an R^2 value of 0.990. When the curvature is higher than 2.45 m^{-1}, the sensitivities of the three dips determined are -15.76, -14.41 and -14.54 nm/m^{-1}, where the R^2 are 0.985, 0.998 and 0.997, respectively.

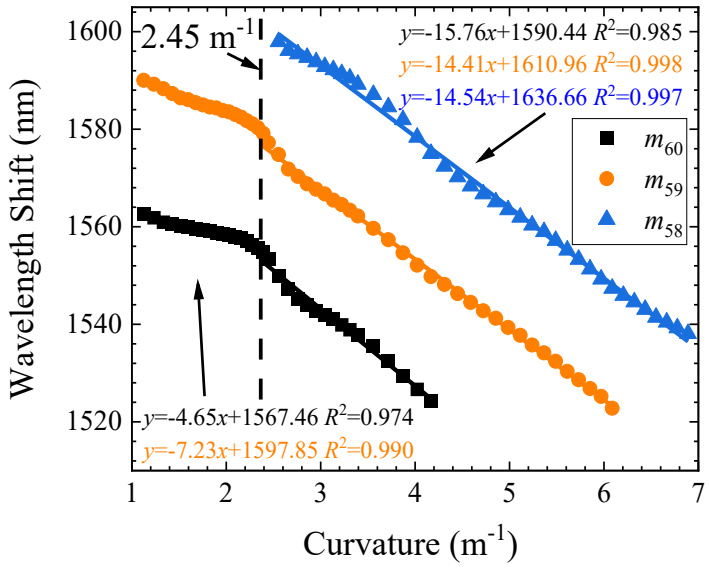

Figure 5-8: Dependence of dip shift of GO-coated FMZI on the increase of curvature and the results of linear fitting for dips m_{60}, m_{59}, and m_{58}.

5.4 Curvature Sensitivity of Graphene Oxide/ Sodium Alginate Coated Fiber Mach-Zehnder Interferometer

The transmission spectrum of GO/Algin-coated FMZI at different curvatures is shown in Figure 5-9. As the curvature increases, the dip wavelength becomes blue-shifted while its intensity changes periodically during the first measurement range for the curvature up to 2.55 m^{-1}, as shown in Figure 5-9 (a). Figures 5-9 (b) and (c) illustrate the transmission spectra of GO/Algin-coated FMZI in the measurements corresponding to the curvature in 2.55 to 4.92 m^{-1} and 4.92 to

6.95 m^{-1}, respectively. Using FFT, the effect of curvature on the propagation pattern is further examined by selecting some random data in the middle of the measurement range, as shown in Figure 5-10. When the curvature is 1.75 m^{-1}, there is a dominant peak with a spatial frequency of 0.044 nm^{-1} and a minor peak at 0.078 m^{-1}. Furthermore, when the curvature increases to 6.95 m^{-1}, the dominant peak is located at 0.033 nm^{-1}, with a minor peak at 0.067 nm^{-1}. The observed results indicate that as the curvature reaches 2.39 m^{-1}, the major peak shifts towards a smaller spatial frequency. Additionally, the amplitude of the minor peak at 0.078 nm^{-1} gradually decreases, while the amplitude at 0.067 nm^{-1} gradually increases with increasing curvature.

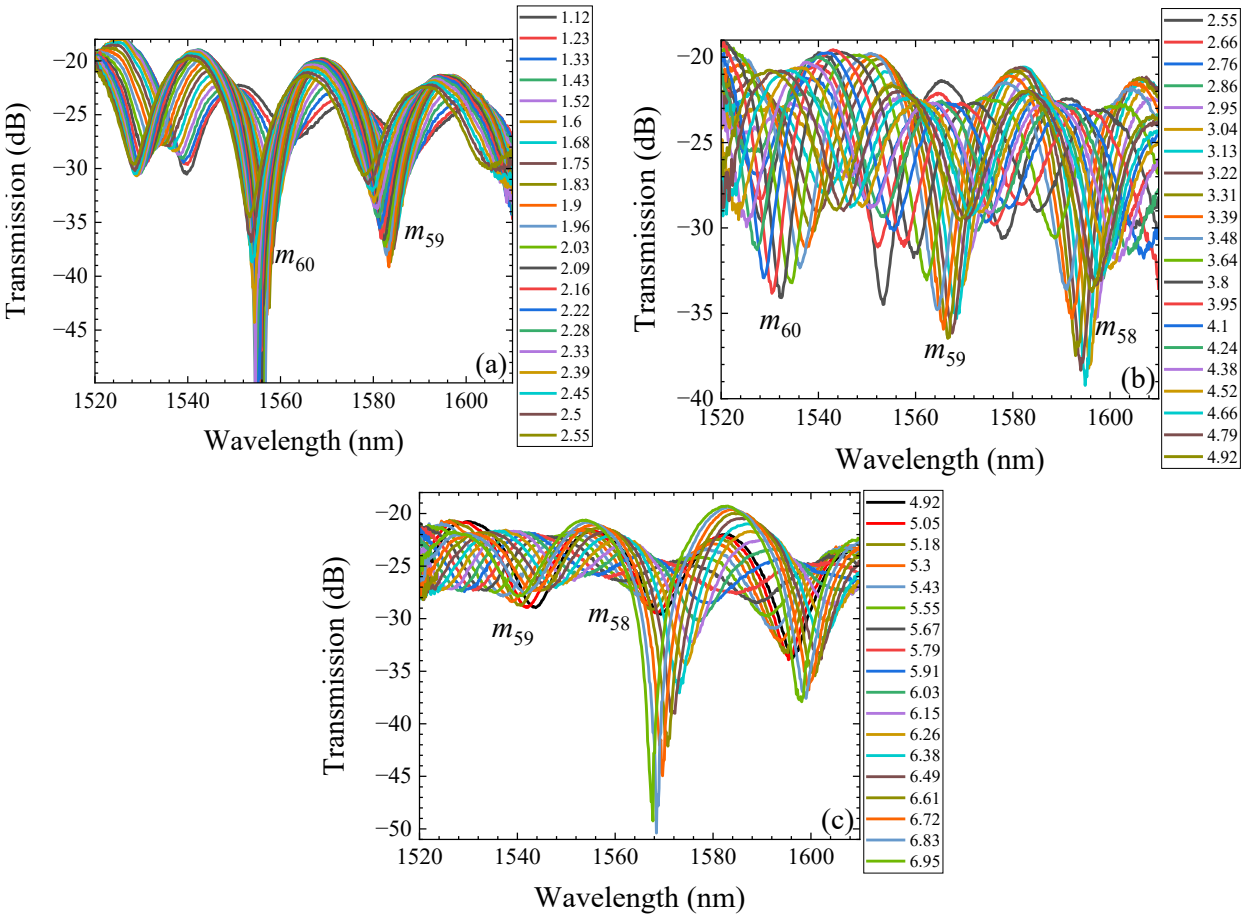

Figure 5-9: Transmission spectra of the GO/Algin-coated tapered FMZI, which are recorded at various curvatures ranging from (a) 1.12 to 2.55 m^{-1}, (b) 2.55 to 4.92 m^{-1}, and (c) 4.92 to 6.95 m^{-1}.

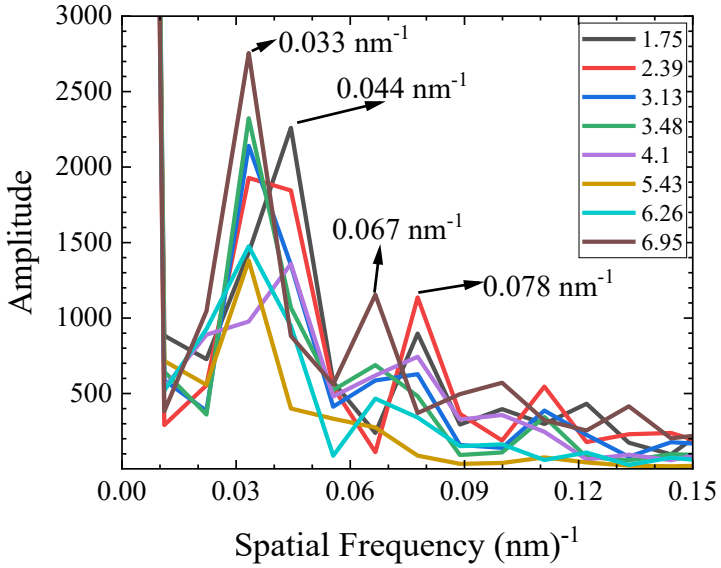

Figure 5-10: FFT of the transmission spectra of the GO/Algin-coated tapered FMZI.

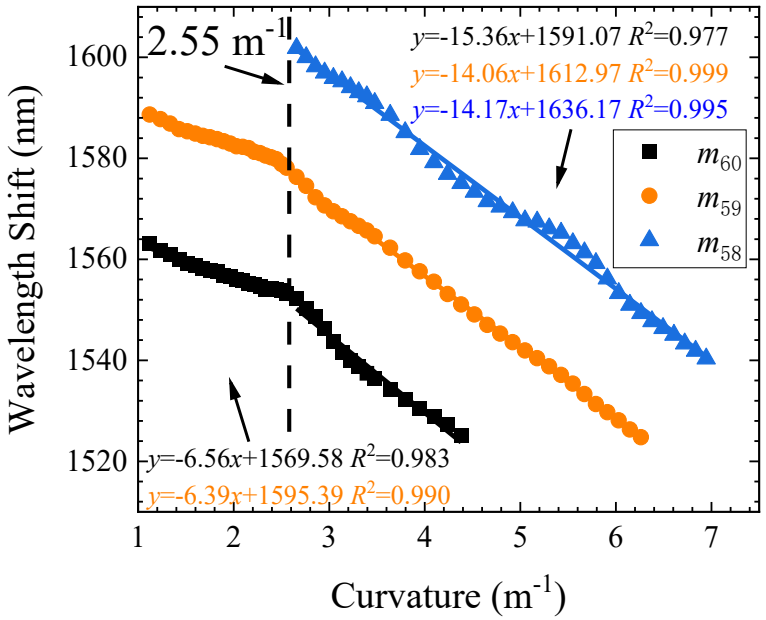

Figure 5-11: Dependence of dip shift of GO/Algin-coated FMZI on the increase of curvature and the results of linear fitting for dips m_{60}, m_{59}, and m_{58}.

Figure 5-11 shows how the dips m_{60}, m_{59}, and m_{58} shift with increasing curvature, revealing the relationship between curvature sensitivity and linear fitting. A turning point is

observed at a curvature of 2.55 m^{-1}, indicating a sensitivity division. When the curvature is below 2.55 m^{-1}, the curvature sensitivity is -6.56 nm/m^{-1} for m_{60}, with an R^2 value of 0.983. Similarly, for m_{59}, the sensitivity is -6.39 nm/m^{-1} with an R^2 value of 0.99. On the other hand, when the curvature exceeds 2.55 m^{-1}, the sensitivity values for the three dips are as follows: -15.36, -14.06, and -14.17 nm/m^{-1}, respectively. The R^2 value of determination are 0.977, 0.999, and 0.995.

5.5 Curvature Sensitivity of Graphene Oxide/Fullerene: Hydrogel Coated Fiber Mach-Zehnder Interferometer

Figure 5-12 presents the transmission spectra of GO/$C_{60}(OH)_n$: hydrogel-coated FMZI at various curvatures. With an increase in curvature, the dip shows a blue-shift, while its intensity undergoes periodic changes. Figures 5-12 (a) to (c) illustrate the transmission spectra of GO/$C_{60}(OH)_n$: hydrogels-coated FMZI in the measurements corresponding to the curvature in 1.33 to 2.55 m^{-1}, 2.66 to 4.24 m^{-1}, and 4.24 to 5.91 m^{-1}, respectively.

Figure 5-13 presents the FFT analysis of the GO/$C_{60}(OH)_n$: hydrogel-coated FMZI at different curvatures. For curvatures below 2.55 m^{-1}, a dominant peak is observed at a spatial frequency of 0.044 nm^{-1}. As the curvature ranges from 2.55 to 4.24 m^{-1}, the dominant peak shifts to 0.033 nm^{-1}, and a minor peak at 0.078 nm^{-1}. Above a curvature of 4.24 m^{-1}, the dominant peak remains at 0.033 nm^{-1}, while the amplitude of the minor peak decreases until it eventually disappears.

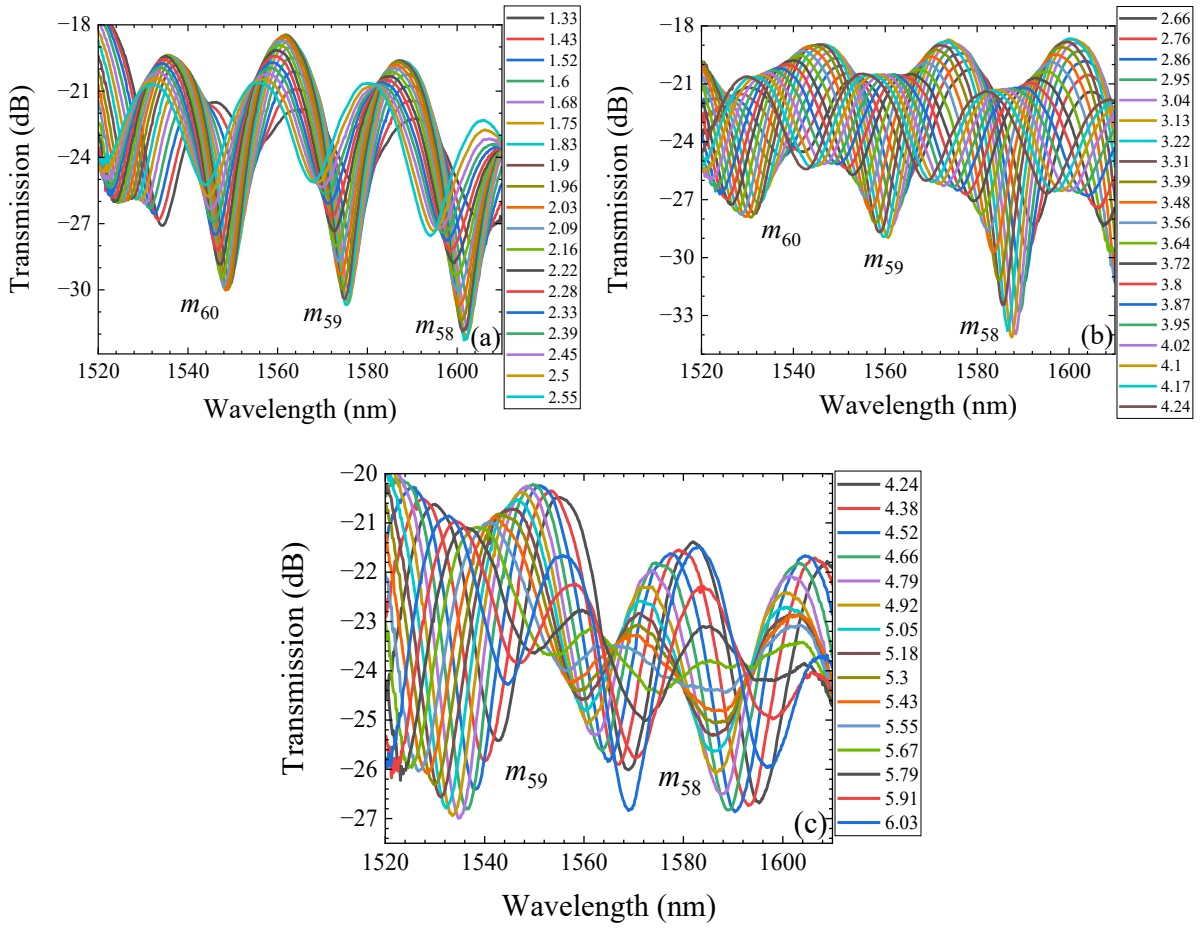

Figure 5-12: Transmission spectra of the GO/$C_{60}(OH)_n$: hydrogel-coated tapered FMZI, which are recorded at various curvatures ranging from (a) 1.33 to 2.55 m^{-1}, (b) 2.66 to 4.24 m^{-1}, and (c) 4.24 to 6.03 m^{-1}.

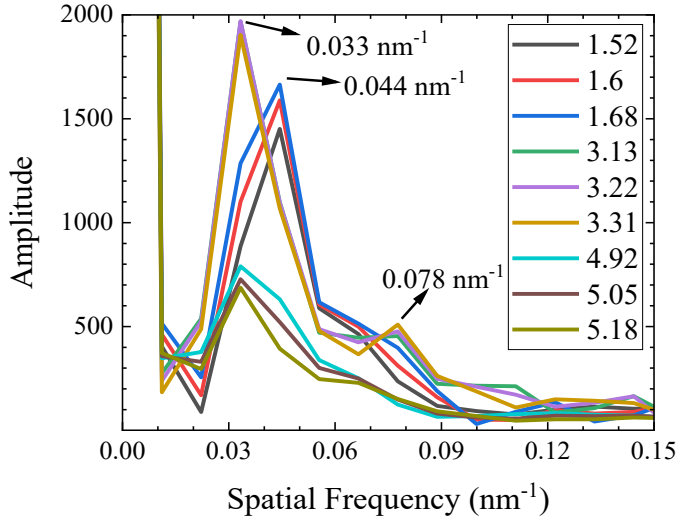

Figure 5-13: FFT of the transmission spectra of the GO/$C_{60}(OH)_n$: hydrogel-coated tapered FMZI.

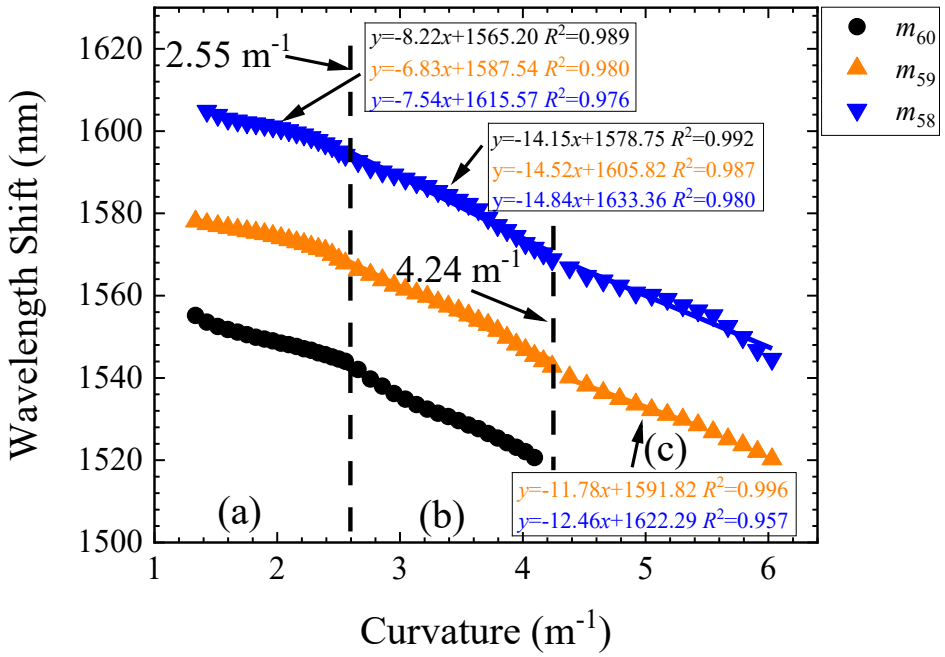

Figure 5-14: Dependence of wavelength shifts of GO/$C_{60}(OH)_n$: hydrogel-coated FMZI on the increase of curvature and the results of linear fitting for dips m_{60}, m_{59}, and m_{58}. (a) 1.33 to 2.55 m^{-1}, (b) 2.55 to 4.24 m^{-1}, and (c) 4.24 to 6.03 m^{-1}.

Figure 5-14 zone (a) shows the curvature sensitivity of m_{60} to be -8.22 nm/m^{-1} with an R^2 value of 0.989. Similarly, m_{59} exhibits a curvature sensitivity of -6.83 nm/m^{-1} with an R^2 value of 0.980, and m_{58} has a sensitivity of -7.54 nm/m^{-1} with an R^2 value of 0.976. In Figure 5-14 zone (b), the curvature sensitivities of the three dips are determined as -14.15, -14.52, and -14.84 nm/m^{-1}, with the R^2 are 0.992, 0.987, and 0.980, respectively. Figure 5-14 zone (c) shows that the dip m_{59} demonstrates a curvature sensitivity of -11.78 nm/m^{-1}, with an R^2 value of 0.996, and the curvature sensitivity of dip m_{58} is -12.46 nm/m^{-1}, with an R^2 value of 0.957.

Chapter 6 Conclusion

Optical fiber sensing technology has become one of the most important sensing technologies due to its unique advantages. Graphene, with its two-dimensional atomic structure, has unique mechanical, electronic, and optical properties. Graphene oxide (GO) is one of the derivatives of graphene. Graphene oxide-based materials enable a wide range of sensing applications owing to its interaction of oxygen-rich functional groups with external water molecules and various organic solvents. Two types of symmetrical fiber Mach-Zehnder interferometers (FMZIs) prepared by the arc discharge method are used to investigate the effect of the fiber microstructure on sensitivity and coating properties. In this study, two GO-based coating materials are proposed for the first time to study their sensing performance under various environmental conditions, including refractive index, temperature, humidity, and curvature and compare them with GO coatings. The two materials are graphene oxide-sodium alginate composites (GO/Algin) and graphene oxide-fullerenol nano-composite encapsulated by the hydrogel ($GO/C_{60}(OH)_n$: hydrogel).

The waist diameter of tapered fibers prepared by the arc discharge method is determined by the arc power and stretch length. COMSOL simulation on the tapered FMZIs demonstrates that reducing the cone diameter decreases transmission intensity and results in a blue-shift of the dip in the transmission spectrum. Multiple cladding modes are coupled in the second tapered segment due to the larger cladding diameter. The transmission spectrum can be analyzed using fast Fourier transform (FFT). The FFT of a tapered interferometer exhibits a major peak and

several minor peaks, indicating the effective coupling of higher-order cladding modes with the core mode. The COMSOL simulation on the bulge-fused FMZI shows that, as the diameter of the bulge-fused structure increases, the intensity of the interference dip wavelength increases and red-shifts. From the Fourier transform pattern, it can be observed that the transmission spectra of the bulge-fused interferometers have only one dominant spatial frequency, which indicates that it cannot couple the higher-order cladding mode back to the core mode, although that structure can couple the core mode to the cladding.

The results of refractive index (RI) measurement with tapered fibers coated with GO of different thicknesses show that the GO coating enhances the sensitivity of the refractive index measurement. The RI sensitivity of tapered FMZI increases from -10.23 to -32.37 nm/RIU after being coated with 6.85 μm of GO. However, if the coating thickness is too large, the inner layer of GO coating hardly changes because of the limited permeability of absorbing water molecules. By analyzing the phase shift of the two spatial frequency peaks through the Fourier transform of the transmission spectra, it can be found that the higher-order cladding mode is more sensitive when the external refractive index changes. The tapered FMZI coated with GO shows an apparent red-shift and good linearity in the temperature and humidity measurement, with sensitivities of 0.0356 nm/°C, and 0.0427 nm/RH%, respectively. It is also shown that the refractive index of graphene oxide decreases with increasing humidity. In humidity sensitivity measurement, both uncoated and GO-coated bulge-fused FMZIs exhibit insensitivity. However, in temperature and refractive index sensitivity measurement, the dip wavelength of the uncoated bulge-fused FMZI displays a nonlinear shift with changing temperature and refractive index. On the other hand, when coated with a GO layer, the dip wavelength shift of the bulge-fused FMZI

shows a linear relationship in both temperature and refractive index measurement, with sensitivities of 0.0573 nm/°C, and 30.44 nm/RIU, respectively.

At dip m_{61} the RI and temperature sensitivities of GO/Algin-coated tapered FMZI are -23.91 nm/RIU and 0.0492 nm/°C, respectively. The refractive index sensitivity of the GO/Algin-coated tapered FMZI exhibits a non-linear relationship in dip shift at m_{60}, which can be attributed to the non-uniform swelling of the coating in the KCl solution. Additionally, the GO/Algin-coated tapered FMZI shows a higher sensitivity during humidity measurement when the humidity level exceeds 50 RH%, which is 0.0215 nm/RH%. This sensitivity enhancement can be attributed to the water-retaining property of sodium alginate. At higher humidity levels, the entire coating becomes fully soaked with water molecules, resulting in increased sensitivity to variations in water molecule density in the surrounding environment. The insensitivity of $GO/C_{60}(OH)_n$: hydrogel-coated tapered FMZI during refractive index and humidity measurement indicate that, while the water-soluble $GO/C_{60}(OH)_n$ nanocomposite is avoided from being dissolved in water, the hydrogel coating also prevents the internal coating from reacting with the surrounding area. While the temperature sensitivity of the GO-coated tapered FMZI may be marginally lower compared to other coated and bulge-fused structure FMZIs, its strong linearity and heightened sensitivity in humidity measurements render it a preferred choice for practical applications.

Curvature sensitivity measurement is conducted by measuring the transmission spectra of uncoated tapered FMZI and tapered FMZIs coated with three different types of GO-based materials at varying curvatures. When a tapered fiber is bent, the modal field distribution will change, which results in the coupling of the core mode to the cladding modes. This coupling can occur either from the side of the fiber that is stretched or from the side that is compressed. As the

uncoated tapered FMZI bends, the waist of the tapered structure will bend first, so the angle of incidence of light will be affected by the bent fiber and the change of the tapered structure. The relationship between dip wavelength and curvature is non-linear because the intensity of the higher-order cladding modes gradually decreases as the curvature increases. After being coated with graphene oxide-based materials, the strength of the coating can reduce the effect of the changing structure in the tapered region to increase the measurement range of curvature sensitivity.

GO-coated optical fibers have found application in the detection of ethanol vapor concentration [112], ammonia gas concentration [113], refractive index sensing [114], and humidity sensing [115]. This versatility is attributed to the ample presence of functional groups on the GO-coated surface. Due to the electrostatic repulsion between GO layers, achieving a uniform GO coating with a specific thickness on optical fibers is challenging. This paper employs an improved i-LBL method to achieve high-quality GO coating on a designated area. GO/Algin composites were previously reported as desiccants [116], oil-water separation membranes [117], and in the detecting perfluorooctanoic acid in water [118], owing to their hygroscopic properties and ability to adsorb trace amounts of certain heavy metals. GO/$C_{60}(OH)_n$ nanocomposites were reported as electrode materials [119], and in applications, such as electronic humidity sensor [120], and solar cells [121]. Coating materials GO/Algin and GO/$C_{60}(OH)_n$ are proposed and demonstrated in this study to investigate their sensitivities of RI, temperature, humidity, and curvature. The sensitivity to refractive index, temperature, and humidity is enhanced by 216%, 40%, and 1192%, respectively, when the tapered FMZI is coated with GO, while for the GO/Algin coating, the enhanced percentages are 56%, 18%, and 760% (>50 RH%), respectively. The GO/$C_{60}(OH)_n$ coating shows enhanced percentages of 7% and 200%

(>50 RH%) for refractive index and humidity sensitivities, respectively, while the temperature sensitivity decreases by 12%. The measurement range of uncoated tapered FMZI in curvature measurement is 1.57 to 4.20 m^{-1} in the wavelength range 1520.00 to 1610.00 nm. After coated with GO, GO/Algin, and GO/$C_{60}(OH)_n$, the curvature measurement ranges extend from 1.01 to 6.89 m^{-1}, 1.12 to 6.95 m^{-1}, and 1.33 to 6.03 m^{-1}, respectively. The sensitivities of many previously reported fiber sensors were either restricted by the materials or complicated manufacturing processes, such as single hollow core Bragg fiber [122], or spearheaded with a lower sensitivities such as temperature sensitivity of 0.03839 nm/°C [123], and humidity sensitivity of 0.01 nm/RH% [124]. FMZIs developed in this study exhibit enhanced sensitivities. In addition, only single-mode fibers are adopted in the FMZIs in this study, and the in-situ self-assembly method greatly reduces the waste of material in the coating process. Overall, this study highlights the effectiveness and significant potential of GO-based nanomaterials in fiber optic sensing applications.

References

[1] Y. Liu, X. Song, B. Li, J. Dong, L. Huang, D. Yu, and D. Feng, “Simultaneous measurement of temperature and strain based on SCF-based MZI cascaded with FBG,” *Appl. Opt.*, **59**, 9476-9481 (2020).

[2] S. Zhang, X. Dong, T. Li, C. Chan, and P. Shum, “Simultaneous measurement of relative humidity and temperature with PCF-MZI cascaded by fiber Bragg grating,” *Opt. Commun.*, **303**, 42–45 (2013).

[3] Y. Wang, Y. Li, C. Liao, D. N. Wang, M. Yang and P. Lu, "High-temperature sensing using miniaturized fiber in-line Mach–Zehnder interferometer," *IEEE Photonics Technol. Lett.*, **22**, 39-41 (2010).

[4] Beaverton: Ringgold Inc., “Optical fiber sensors: Advanced techniques and applications,” *ProtoView*, **2**, 21 (2015).

[5] D. Wang, “Review of femtosecond laser fabricated optical fiber high temperature sensors,” *Chin. Opt. Lett.*, **19**, 091204 (2021).

[6] G. Woyessa, A. Theodosiou, C. Markos, K. Kalli, and O. Bang, “Single peak fiber Bragg grating sensors in tapered multimode polymer optical fibers,” *J. Lightwave Technol.*, **39**, 6934-6941 (2021).

[7] M. A. Kamizi, D. Lugarini, R. Fuser, L. H. Negri, J. L. Fabris, and M. Muller, “Multiplexing optical fiber macro-bend load sensors,” *J. Lightwave Technol.*, **37**, 4858-4863 (2019).

[8] H. Chen, B. Luo, D. Wu, X. Yang, S. Shi, X. Zou, Y. Li, S. Jiang, and M. Zhao, “Optical vernier sensor based on a cascaded tapered thin-core microfiber for highly sensitive refractive index sensing,” *Appl. Opt.*, **61**, 10727-10734 (2022).

[9] Y. Liang, L. Jin, L. Wang, X. Bai, L. Cheng, and B. Guan, “Fiber-laser-based ultrasound sensor for photoacoustic imaging,” *Sci. Rep.,* **7**, 40849 (2017).

[10] X. Yin, N. Wang, X. Yu, Y. Li, B. Zhang, and D. Li, “Theoretical analysis and optimization of extrinsic Fabry-Perot interferometer optical-fiber humidity-sensor structures,” *Curr. Opt. Photon*., **5**, 652-659 (2021).

[11] W. Sheng, H. Dang, and G. Peng, “Hysteresis and temperature drift compensation for FBG demodulation by utilizing adaptive weight least square support vector regression,” *Opt. Express*, **29**, 40547-40558 (2021).

[12] R. Wang, J. Zhao, Y. Sun, H. Yu, N. Zhou, H. Zhang, and D. Jia, “Wearable respiration monitoring using an in-line few-mode fiber Mach-Zehnder interferometric sensor,” *Biomed. Opt. Express*, **11**, 316-329 (2020).

[13] S. H. Lee, Y. Roh, S. Lee, Y. Ryu, B. Ju, and M. Seo, “Direct comparison with terahertz metamaterials and surface-enhanced Raman scattering in a molecular-specific sensing performance,” *Opt. Express*, **29**, 12-23 (2021).

[14] Y. Wei, C. Liu, C. Liu, C. Shi, R. Wang, X. Wang, Z. Ren, Z. Ran, Z. Liu, and Y. Zhang, “Multi-channel curvature sensor based on fiber bending loss wavelength and SPR,” *Opt. Lett.*, **47**, 6017-6020 (2022).

[15] Z. Liu, H. Tam, L. Htein, M. V. Tse, and C. Lu, "Microstructured optical fiber sensors," *J. Lightwave Technol.*, **35**, 3425-3439 (2017).

[16] G. Brambilla, “Optical fibre nanowires and microwires: a review,” *J. Opt.*, **12**, 043001 (2010).

[17] P. Niu, J. Zhao, C. Zhang, H. Bai, X. Sun, J. Bai, and L. Chen, “S fiber taper-based fiber loop ring-down refractometer,” *IEEE Sens. J.*, **19**, 970–975 (2019).

[18] J. Yoon, J. Lee, G. Kim, S. Ryu, and J. Park, “Deep neural network-based structural health monitoring technique for real-time crack detection and localization using strain gauge sensors,” *Sci. Rep.*, **12**, 20204 (2022).

[19] A. Leal-Junior, L. Avellar, A. Frizera, C. Marques, “Smart textiles for multimodal wearable sensing using highly stretchable multiplexed optical fiber system,” *Sci. Rep.*, **10**, 13867 (2020).

[20] M. Born, and E. Wolf, “Principles of Optics,” *Pergamon Press, Oxford* (1970).

[21] J. Ballato, T. Hawkins, P. Foy, B. Kokuoz, R. Stolen, C. McMillen, M. Daw, Z. Su, T. M. Tritt, M. Dubinskii, J. Zhang, T. Sanamyan, and M. J. Matthewson, “On the fabrication of all-glass optical fibers from crystals,” *J. Appl. Phys.*, **105**, 053110 (2009).

[22] P. H. Reddy, A. V. Kir'yanov, A. Dhar, S. Das, D. Dutta, M. Pal, Y. O. Barmenkov, J. A. Minguella-Gallardo, S. K. Bhadra, and M. C. Paul, "Fabrication of ultra-high numerical aperture GeO_2-doped fiber and its use for broadband supercontinuum generation," *Appl. Opt.*, **56**, 9315-9324 (2017).

[23] C. Hnatovsky, K. D. Silva, N. Abdukerim, R. B. Walker, H. Ding, and S. J. Mihailov, "Nanoscale morphology and thermal properties of low insertion loss fiber Bragg gratings produced using the phase mask technique and a single femtosecond laser pulse," *Opt. Express*, **30**, 47361-47374 (2022).

[24] A. W. Snyder and J. D. Love, "Optical waveguide theory," *Boston, MA: Springer US* (1984).

[25] Philip Russell, "Photonic crystal fibers," *Science*, **299**, 358-362 (2003).

[26] Y. Shi-Kay, and C. Asawa, "Fiber optical intensity sensors," *IEEE J. Sel. Areas Commun.*, **1**, 562–575 (1983).

[27] M. Arumugam, "Optical fiber communication - An overview," *Pramāṇa*, **57**, 849–869 (2001).

[28] J. Qian, and W. Huang, "Coupled-mode theory for LP modes," *J. Lightw. Technol.*, **4**, 619–625 (1986).

[29] C. Buckberry, "Optical fibre sensor technology," *Opt. Laser Technol.*, **28,** 9 (1996).

[30] B. H. Lee, Y. H. Kim, K. S. Park, J. B. Eom, M. J. Kim, B. S. Rho, and H, Y. Choi, "Interferometric fiber optic sensors," *Sensors*, **12**, 2467–2486 (2012).

[31] L. Zehnder, "Ein neuer Interferenzrefraktor," *Zeitschrift für Instrumentenkunde*, **11**, 275–285 (1891).

[32] K. P. Zetie, S. F. Adams, and R. M. Tocknell, "How does a Mach-Zehnder interferometer work?" *Phys. Edu.*, **35**, 46-48 (2000).

[33] M. Hou, J. Tian, Y. Jiang, and Y. Zuo, "Highly sensitive and stable fiber-laser pressure-sensing system based on an unequal-arm Mach-Zehnder cascaded with a Sagnac structure," *Opt. Express*, **29**, 43454 (2021).

[34] J. H. Lim, H. S. Jang, K. S. Lee, J. C. Kim, and B. H. Lee, "Mach-Zehnder interferometer formed in a photonic crystal fiber based on a pair of long-period fiber gratings," *Opt. Lett.*, **29**, 346–348 (2004).

[35] B. H. Lee, and U. C. Paek, "Multislit interpretation of cascaded fiber gratings," *J. Lightw. Techol.*, **20**, 1750–1761 (2002).

[36] H. Y. Choi, M. J. Kim, and B. H. Lee, "All-fiber Mach-Zehnder type interferometers formed in photonic crystal fiber," *Opt. Express*, **15**, 5711–5720 (2007).

[37] L. V. Nguyen, D. Hwang, S. Moon, D. S. Moon, and Y. Chung, "High temperature fiber sensor with high sensitivity based on core diameter mismatch," *Opt. Express*, **16**, 11369–11375 (2008).

[38] B. Gu, M. Yin, A. Zhang, J. Qian, and S. He, "Optical fiber relative humidity sensor based on FBG incorporated thin-core fiber modal interferometer," *Opt. Express*, **19**, 4140–4146 (2011).

[39] P. Lu, L. Men, K. Sooley, and Q. Chen, "Tapered fiber Mach-Zehnder interferometer for simultaneous measurement of refractive index and temperature," *Appl. Phys. Lett.*, **94**, 131110 (2009).

[40] L. Jiang, J. Yang, S. Wang, B. Li, and M. Wang, "Fiber Mach-Zehnder interferometer based on microcavities for high-temperature sensing with high sensitivity." *Opt. Lett.*, **36**, 3753–3755 (2011).

[41] S. Duan, W. Liu, C. Sun, H. Jiang, C. Yao, K. Zhang, X. Bai, W. Wang, C. Lu, T. Geng, F. Peng, and L. Yuan, "High sensitive directional twist sensor based on a Mach–Zehnder interferometer," *IEEE Photon. J.*, **10**, 1-7 (2018).

[42] D. Wu, T. Zhu, K. S. Chiang, and M. Deng, "All single-mode fiber Mach-Zehnder interferometer based on two peanut-shape structures," *J. Light. Technol.*, **30**, 805-810 (2012).

[43] X. Sun, H. Du, X. Dong, Y. Hu, and J. Duan, "Simultaneous curvature and temperature sensing based on a novel Mach-Zehnder interferometer," *Photonic Sens.*, **10**, 171–180 (2020).

[44] K. S. Novoselov, A. K. Geim, S. V. Morozov, D. Jiang, Y. Zhang, S. V. Dubonos, I. V. Grigorieva, and A. A. Firsov, "Electric field effect in atomically thin carbon films," *Science*, **306**, 666–669 (2004).

[45] D. Gadakh, P. Dashora, and G. Wadhankar, “A review paper on graphene coated fibres,” *Graphene*, **8**, 53–74 (2019).

[46] Y. Liu, R. Cheng, L. Liao, H. Zhou, J. Bai, G. Liu, L. Liu, Y. Huang, and X. Duan, “Plasmon resonance enhanced multicolour photodetection by graphene” *Nat. Commun.*, **2**, 579 (2011).

[47] X. Liang, N. Li, R. Zhang, P. Yin, C. Zhang, N. Yang, K. Liang, and B. Kong, “Carbon-based SERS biosensor: from substrate design to sensing and bioapplication,” *NPG Asia Mater.*, **13**, 8 (2021).

[48] T. Hang, J. Wu, S. Xiao, B. Li, H. Li, C. D. Yang, C. Yang, N. Hu, Y. Xu, Y. Zhang, and X. Xie, “Anti-biofouling NH_3 gas sensor based on reentrant thorny ZnO/graphene hybrid nanowalls,” *Microsyst. Nanoeng.*, **6**, 41 (2020).

[49] H. Yang, H. Hu, Y. Wang, and T. Yu, “Rapid and non-destructive identification of graphene oxide thickness using white light contrast spectroscopy,” *Carbon*, **52**, 528–534 (2013).

[50] Y. Wang, C. Shen, W. Lou, and F. Shentu, “Polarization-dependent humidity sensor based on an in-fiber Mach-Zehnder interferometer coated with graphene oxide,” *Sens. Actuators B Chem.*, **234**, 503–509 (2016).

[51] M. Tian, Y. Huang, C. Li, and M. Lv, “High-performance humidity sensor based on a micro-nano fiber Bragg grating coated with graphene oxide,” *Opt. Express*, **28**, 26395–26406 (2020).

[52] M. Divagar, A. Gowri, S. John, and V. V. R. Sai, “Graphene oxide coated U-bent plastic optical fiber based chemical sensor for organic solvents,” *Sens. Actuators B Chem.*, **262**, 1006 (2018).

[53] E. Owji, H. Mokhtari, F. Ostovari, B. Darazereshki, and N. Shakiba, “2D materials coated on etched optical fibers as humidity sensor,” *Sci. Rep.*, **11**, 1771 (2021).

[54] F. Song, F. Ke, H. Zhang, and H. Wang, “Preparation of graphene-coated conductive fibers by layer-by-layer assembly of negative and positive charged graphene Oxide,” *Mater. Today: Proc.*, **16**, 1542–1547 (2019).

[55] M. Fang, X. Xiong, Y. Hao, T. Zhang, H. Wang, H. Cheng, and Y. Zeng, “Preparation of highly conductive graphene-coated glass fibers by sol-gel and dip-coating method,” *J. Mater. Sci. Technol.*, **35**, 1989–1995 (2019).

[56] X. Fan, Q. Wang, M. Zhou, F. Liu, H. Shen, Z. Wei, F. Wang, C. Tan, and H. Meng, "Humidity sensor based on a graphene oxide-coated few-mode fiber Mach-Zehnder interferometer," *Opt. Express*, **28**, 24682–24692 (2020).

[57] M. Singh, S. K. Raghuwanshi and O. Prakash, "Ultra-sensitive fiber optic gas sensor using graphene oxide coated long period gratings," *IEEE Photonics Technol. Lett.*, **31**, 1473-1476 (2019).

[58] M. Tian, Y. Huang, C. Li, and M. Lv, "High-performance humidity sensor based on a micro-nano fiber Bragg grating coated with graphene oxide," *Opt. Express*, **28**, 26395–26406 (2020).

[59] Y. Zhao, A. Li, Q. Guo, X. Ming, Y. Zhu, X. Sun, P. Li, and Y. Yu, "Relative humidity sensor of S fiber taper based on graphene oxide film," *Opt. Commun.*, **450**, 147–154 (2019).

[60] S. T. Bashir, L. Yang, J. J. Liggat, and J. L. Thomason, "Kinetics of dissolution of glass fibre in hot alkaline solution," *J. Mater. Sci.*, **53**, 1710–1722 (2018).

[61] G. Box, D. Behnken, "Some new three level designs for the study of quantitative variables," *Technometrics*, **2**, 455–475 (1960).

[62] J. P. Maran, S. Manikandan, K. Thirugnanasambandham, C. V. Nivetha, and R. Dinesh, "Box–Behnken design based statistical modeling for ultrasound-assisted extraction of corn silk polysaccharide," *Carbohydr. Polym.*, **92**, 604 (2013).

[63] A. Gelman, "Analysis of variance: Why it is more important than ever," *The Annals of Statistics*, **33**, 1–31 (2005).

[64] M. Ahmad, and H. L. Larry, "Effect of taper geometries and launch angle on evanescent wave penetration depth in optical fibers," *Biosens. Bioelectron.*, **20**, 1312–1319 (2005).

[65] V. Dhavamani, S. Chakraborty, S. Ramya, & S. Nandi, "Design and simulation of waveguide Bragg grating based temperature sensor in COMSOL," *J. Phys. Conf. Ser.*, **2161**, 12047 (2022).

[66] W. T. Cochran, P. D. Welch, J. W. Cooley, D. L. Favin, H. D. Helms, R. A. Kaenel, W. W. Lang, G. C. Maling, Nelson, D. E., and Rader, C. M., "What is the fast Fourier transform?" *Proc. IEEE*, **55**, 1664-1674 (1967).

[67] M. Xiong, H. Gong, Z. Wang, C. Zhao, and X. Dong, "Optical modal interferometer fiber strain sensor based on waist-enlarge fusion splicing," *Optik*, **127**, 6862–6866 (2016).

[68] T. Jiao, H. Meng, S. Deng, S. Liu, X. Wang, Z. Wei, F. Wang, C. Tan, and X. Huang, "Simultaneous measurement of refractive index and temperature using a Mach-Zehnder interferometer with forward core-cladding-core recoupling," *Opt. Laser Technol.*, **111**, 612–615 (2019).

[69] Y. Wang, C. Shen, W. Lou, and F. Shentu, "Fiber optic humidity sensor based on the graphene oxide/PVA composite film," *Opt. Commun.*, **372**, 229–234 (2016).

[70] M. Ionita, M. A. Pandele, and H. Iovu, "Sodium alginate/graphene oxide composite films with enhanced thermal and mechanical properties," *Carbohydr. Polym.*, **94**, 339–344 (2013).

[71] K. Cao, Z. Jiang, J. Zhao, C. Zhao, C. Gao, F. Pan, B. Wang, X. Cao, and J. Yang, "Enhanced water permeation through sodium alginate membranes by incorporating graphene oxides," *J. Membr. Sci.*, **469**, 272–283 (2014).

[72] L. Binetti, A. Stankiewicz, and L. S. M. Alwis, "Graphene-oxide and hydrogel coated FBG-based pH sensor for biomedical applications," *Proceedings*, **2**, 789 (2018).

[73] C. Bian, J. Wang, X. Bai, M. Hu, and T. Gang, "Optical fiber based on humidity sensor with improved sensitivity for monitoring applications," *Opt. Laser Technol.*, **130**, 106342 (2020).

[74] X. Ding, X. Chen, X. Zhao, and N. Li, "A QCM humidity sensor based on fullerene/graphene oxide nanocomposites with high quality factor," *Sens. Actuators B Chem.*, **266**, 534–542 (2018).

[75] D. Martens, and P. Bienstman, "Study on the limit of detection in MZI-based biosensor systems," *Sci. Rep.*, **9**, 5767–5767 (2019).

[76] D. Kohler, G. Schindler, L. Hahn, J. Milvich, A. Hofmann, K. Länge, W. Freude, and C. Koos, "Biophotonic sensors with integrated Si_3N_4-organic hybrid (SiNOH) lasers for point-of-care diagnostics," *Light Sci. Appl*, **10**, 64–64 (2021).

[77] X. Sun, X. Dong, Y. Hu, H. Li, D. Chu, J. Zhou, C. Wang, and J. Duan, "A robust high refractive index sensitivity fiber Mach-Zehnder interferometer fabricated by femtosecond laser machining and chemical etching," *Sens. Actuator A Phys.*, **230**, 111–116 (2015).

[78] J. Wo, G. Wang, Y. Cui, Q. Sun, R. Liang, P. P. Shum, and D. Liu, “Refractive index sensor using microfiber-based Mach-Zehnder interferometer,” *Opt. Lett.*, **37**, 67–69 (2012).

[79] F. Yu, P. Xue, X. Zhao, and J. Zheng, “Investigation of an in-line fiber Mach–Zehnder interferometer based on peanut-shape structure for refractive index sensing,” *Opt. Commun.*, **435**, 173–177 (2019).

[80] Y. Zhao, F. Xia, and J. Li, “Sensitivity-enhanced photonic crystal fiber refractive index sensor with two waist-broadened tapers,” *J. Light. Technol.*, **34**, 1373–1379 (2016).

[81] Ojha, N. N. Subhashree, and N. Kumar. “Refractive index sensitivity enhancement of SF-MZI through metal film deposition,” *Opt. Fiber Technol.*, **7**, 103032 (2022).

[82] A. K. Yetisen, H. Butt, L. R. Volpatti, I. Pavlichenko, M. Humar, S. J. J. Kwok, H. Koo, K. S. Kim, I. Naydenova, A. Khademhosseini, S. K. Hahn, and S. H. Yun, “Photonic hydrogel sensors,” *Biotechnol. adv.*, **34**, 250–271 (2016).

[83] C. Bian, J. Wang, X. Bai, M. Hu, and T. Gang, “Optical fiber based on humidity sensor with improved sensitivity for monitoring applications,” *Opt. Laser Technol.*, **130**, 106342 (2020).

[84] W. Talataisong, R. Ismaeel, and G. Brambilla, “A review of microfiber-based temperature sensors,” *Sensors*, **18**, 461 (2018).

[85] E. Owji, H. Mokhtari, F. Ostovari, B. Darazereshki, and N. Shakiba, “2D materials coated on etched optical fibers as humidity sensor,” *Sci. Rep.*, **11**, 1771 (2021).

[86] A. M. Shrivastav, D. S. Gunawardena, Z. Liu, and H. Y. Tam, “Microstructured optical fiber based Fabry–Pérot interferometer as a humidity sensor utilizing chitosan polymeric matrix for breath monitoring,” *Sci. Rep.*, **10**, 6002 (2020).

[87] B. Zuo, X. Liang, X. Zhang and T. Yin, "Detection of refractive index with a temperature-compensated MZI-based optical sensor using few-mode fiber," *IEEE Access.*, **9**, 158651 (2021).

[88] J. Zhang, Z. Tong, W. Zhang, Y. Zhao, and Y. Liu, “Research on NCF-PCF-NCF structure interference characteristic for temperature and relative humidity measurement,” *IEEE Photon. J.*, **13**, 1–5 (2021).

[89] J. Li, Z. Tong, L. Jing, W. Zhang, J. Qin, and J. Liu, “Fiber temperature and humidity sensor based on photonic crystal fiber coated with graphene oxide,” *Opt. Commun.*, **467**, 125707 (2020).

[90] C. Bian, J. Wang, X. Bai, M. Hu, and T. Gang, "Optical fiber based on humidity sensor with improved sensitivity for monitoring applications," *Opt. Laser Technol.*, **130**, 106342 (2020).

[91] A. K. Geim, and K. S. Novoselov, "The rise of graphene," *Nat. Mater.*, **6**, 183–191 (2007).

[92] J. Fu, Y. Xu, M. Xu, L. G. Abbas, and A. Zhou, "Highly sensitive humidity sensor based on tapered dual side-hole fiber," *Optik*, **261**, 169183 (2022).

[93] W. Qi, and L. Yu, "Review of optical fiber bending/curvature sensor," *Meas.: J. Int. Meas. Confed.*, **130**, 161–176 (2018).

[94] J. N. Fields, and J. H. Cole, "Fiber microbend acoustic sensor," *Appl. Opt.*, **19**, 3265–3267 (1980).

[95] F. Zhao, J. Wang, Y. Xiao, K. Zhang, R. Chen, and S. Liu, "Curvature monitoring of power grid wires based on anti-resonant reflecting guidance in hollow core fibers." *Optik*, **213**, 164785 (2020).

[96] Y. Ma, M. Zhao, C. Su, J. Sun, X. Li, Z. Yu, L. Zhang, and T. Geng, "Vector curvature sensor based on asymmetrically polished long-period fiber grating," *Meas.: J. Int. Meas. Confed.*, **194**, 110997 (2022).

[97] Y. Zhao, M. Chen, F. Xia, and R. Lv, "Small in-fiber Fabry-Perot low-frequency acoustic pressure sensor with PDMS diaphragm embedded in hollow-core fiber," *Sens. Actuator A Phys.*, **270**, 162–169 (2018).

[98] D. Barrera, J. Madrigal, and S. Sales, "Long period gratings in multicore optical fibers for directional curvature sensor implementation," *J. Light. Technol.*, **36**, 1063–1068 (2018).

[99] B. Sun, Y. Huang, S. Liu, C. Wang, J. He, C. Liao, G. Yin, J. Zhao, Y. Liu, J. Tang, J. Zhou, and Y. Wang, "Asymmetrical in-fiber Mach-Zehnder interferometer for curvature measurement," *Opt. Express*, **23**, 14596–14602 (2015).

[100] J. Villatoro, J. V. Newkirk, E. Antonio-Lopez, J. Zubia, A. Schülzgen, and R. Amezcua-Correa, "Ultrasensitive vector bending sensor based on multicore optical fiber," *Opt. Lett.*, **41**, 832–835 (2016).

[101] J. Kong, A. Zhou, C. Cheng, J. Yang, and L. Yuan, "Two-axis bending sensor based on cascaded eccentric core fiber Bragg gratings," *IEEE Photonics Technol. Lett.*, **28**, 1237–1240 (2016).

[102] X. Zhu, S. Li, D. Sun, W. Liu, J. Cao, G. Zhang, Z. Han, L. Zou, C. Wang, and Y. Shi, "High sensitivity temperature and curvature sensor based on Mach-Zehnder interferometer with tapered two peanut-shaped structures," *IEEE Sens. J.*, **22**, 4135–4143 (2022).

[103] L. G. Martinez-Ramirez, E. C. S. Alvarado, E. Gallegos-Arellano, A. Fernandez-Jaramillo, J. M. Estudillo-Ayala, D. Jauregui-Vazquez, Rojas-Laguna, R., and Sierra-Hernandez, J. M., "Select-cutoff Mach-Zehnder interferometer based on waist-enlarged technique and its multi-wavelength fiber laser application," *Infrared Phys. Technol.*, **128**, 104508 (2023).

[104] L. Niu, C. Zhao, H. Gong, Y. Li, and S. Jin, "Curvature sensor based on two cascading abrupt-tapers modal interferometer in single mode fiber," *Opt. Commun.*, **333**, 11–15 (2014).

[105] X. Sun, H. Du, X. Dong, Y. Hu, and J. Duan, "Simultaneous curvature and temperature sensing based on a novel Mach-Zehnder interferometer," *Photonic Sens.*, **10**, 171–180 (2020).

[106] R. T. Schermer and J. H. Cole, "Improved bend loss formula verified for optical fiber by simulation and experiment," in *IEEE J. Quantum Electron.*, **43**, 899-909 (2007)

[107] R. Ulrich, S. C. Rashleigh, and W. Eickhoff, "Bending-induced birefringence in single-mode fibers," *Opt. Lett.*, **5**, 273–275 (1980).

[108] Y. Liu, J. A. R. Williams, and I. Bennion, "Optical bend sensor based on measurement of resonance mode splitting of long-period fiber grating," *IEEE Photonics Technol. Lett.*, **12**, 531–533 (2000).

[109] Y. Gui, Q. Shu, P. Lu, J. Peng, J. Zhang, and D. Liu, "Optical fiber sensor for curvature and temperature measurement based on anti-resonant effect cascaded with multimode interference," *Sensors*, **22**, 8457 (2022).

[110] M. Shao, J. Liang, H. Gao, C. Wang, and Y. Liu, "Seven-core fiber based in-fiber Mach–Zehnder interferometer for temperature-immune curvature sensing," *Opt. Commun.*, **528**, 128989 (2023).

[111] Y. Zhang, L. Zhou, D. Qiao, M. Liu, H. Yang, C. Meng, T. Miao, J. Xue, and Y. Yao, "Progress on optical fiber biochemical sensors based on graphene," *Micromachines*, **13**, 348 (2022).

[112] J. Zhang, H. Fu, J. Ding, M. Zhang, and Y. Zhu, "Graphene-oxide-coated interferometric optical microfiber ethanol vapor sensor," *Appl. Opt.*, **56**, 8828-8831 (2017).

[113] S. H. Girei, M. M. Alkhabet, Y. M. Kamil, H. N. Lim, M. A. Mahdi, and H. M. Yaacob, "Wavelength dependent graphene oxide-based optical microfiber sensor for ammonia gas," *Sensors*, **21**, 1–11 (2021).

[114] K. P. W. Dissanayake, W. Wu, H. Nguyen, T. Sun and K. T. V. Grattan, "Graphene-oxide-coated long-period grating-based fiber optic sensor for relative humidity and external refractive index," *J. Light. Technol.*, **36**, 4, 1145-1151 (2018).

[115] W. H. Lim, Y. K. Yap, W. Y. Chong, and H. Ahmad, "All-optical graphene oxide humidity sensors," *Sensors*, **14**, 24329–24337 (2014).

[116] N. Minh Dat, L. Minh Huong, N. T. Dat, D. B. Thinh, D. N. Trinh, N. T. H. Giang, M. T. Phong, and N. H. Hieu, "Synthesis of hygroscopic sodium alginate-modified graphene oxide: Kinetic, isotherm, and thermodynamic study," *European Polymer Journal*, **174**, 111333 (2022).

[117] M. Ehsan, H. Razzaq, S. Razzaque, M. Kanwal, and I. Hussain, "Engineering nanocomposite membranes of sodium alginate-graphene oxide for efficient separation of oil-water and antifouling performance," *J. Environ. Chem. Eng.*, **11**, 109185 (2023).

[118] F. Faiz, M. J. Cran, J. Zhang, S. Muthukumaran, and F. Sidiroglou, "[," IEEE *J. Sens.*, **23**, 12861-12867 (2023).

[119] R. Jaiswal, U. Saha, T. H. Goswami, A. Srivastava, and N. E. Prasad, ""Pillar effect" of chemically bonded fullerene in enhancing supercapacitance performances of partially reduced fullerenol graphene oxide hybrid electrode material," *Electrochimica Acta*, **283**, 269–290 (2018).

[120] K. Tang, X. Chen, X. Ding, X. Yu, and X. Yu, "MoS_2/Graphene oxide/C_{60}-OH nanostructures deposited on a quartz crystal microbalance transducer for humidity sensing," *ACS Appl. Nano. Mater.*, **4**, 10810–10818 (2021).

[121] S. Lee, J. S. Yeo, J. M. Yun, and D.Y. Kim, "Water dispersion of reduced graphene oxide stabilized via fullerenol semiconductor for organic solar cells," *Opt. Mater. Express*, **7**, 2487-2495 (2017).

[122] B. Huang, X. Sheng, J. Cao, and S. Lou, "A compact sensor integrated in a single hollow core Bragg fiber for simultaneous measurement of temperature and strain," *IEEE J. Sens.*, **23**, 10478 (2023).

[123] Q. Wang, X. Chen, X. Zhou, W. Liu, D. Song, X. Yan, X. Zhang, F. Wang, T. Suzuki, Y. Ohishi, and T. Cheng, “An antiinterference temperature sensor based on Mach-Zehnder interferometer using kagome hollow-core photonic crystal fiber,” *IEEE J. Sens.*, **23**, 8426–8434 (2023).

[124] S.R. Azzuhri, I.S. Amiri, A.S. Zulkhairi, M.A.M. Salim, M.Z.A. Razak, M.F. Khyasudeen, H. Ahmad, R. Zakaria, and P. Yupapin, “Application of graphene oxide based Microfiber-Knot resonator for relative humidity sensing,” *Results Phys.*, **9**, 1572-1577 (2018).